

Dissertation

Submitted to the
Combined Faculty of Natural Sciences and
Mathematics
of the Ruperto-Carola-University of Heidelberg,
Germany
for the degree of
Doctor of Natural Sciences
(Dr. rer. nat.)

Put forward by
M.Sc. Arnulf Stein
Born in Westerstede

Oral Examination: 25.10.2019

Electronic Structure, Band Formation and Singlet Fission Dynamics at Metal/Organic Interfaces

Referees: Prof. Dr. Petra Tegeder
apl. Prof. Dr. Hans-Robert Volpp

Electronic Structure, Band Formation and Singlet Fission Dynamics at Metal/Organic Interfaces

Charge carrier injection at the metal/organic interface is crucial for the performance of organic semiconductor based (opto)electronic devices. To achieve an efficient charge carrier injection a detailed knowledge of the electronic properties at the metal/organic interface is needed. In this thesis ultraviolet photoemission spectroscopy and (time-resolved, angle-resolved) two-photon photoemission spectroscopy were utilized to reveal occupied as well as unoccupied electronic states including excitonic states and transport levels. On the one hand the electronic structure and excited state dynamics of a pentacene derivative, in particular regarding the singlet fission dynamics with respect to the film thickness on an Au(111) surface, were examined. On the other hand the electronic structure at the interface between several promising N-heteropolycyclic semiconductors, including a porphyrin, a N-heteroacene and different N-heteroperopyrenes, and Au(111) was revealed. The investigations of the N-heteroperopyrenes stand out as the observation of band formation *via* hybridization between delocalized metal bands and localized molecular orbitals at the metal/organic interface should foster efficient charge injection.

Elektronische Struktur, Bandausbildung und Singlet Fission Dynamik an Metall/Organik Grenzflächen

Die Leistungsfähigkeit von auf organischen Halbleitern basierenden (opto)elektronischen Bauelementen ist stark abhängig von der Ladungsträgerinjektion an der Grenzfläche zwischen dem Metall und der Organik. Um eine effiziente Ladungsträgerinjektion zu erreichen ist ein detailliertes Wissen über die elektronischen Eigenschaften der Metall/Organik Grenzfläche notwendig. Im Rahmen dieser Arbeit wurden besetzte und unbesetzte elektronische Zustände, einschließlich exzitonischer Zustände und Transportlevel, mithilfe von Ultraviolett-Photoelektronenspektroskopie und (winkel- und zeitaufgelöster) Zwei-Photonen Photoemissions-Spektroskopie untersucht. Zum einen wurden die elektronische Struktur sowie die Dynamik angeregter Zustände eines Pentalen Derivates aufgeklärt. Im Fokus stand hierbei der „singlet fission“ Zerfall und sein Verhalten in Abhängigkeit von der Schichtdicke der Moleküle auf einer Au(111) Oberfläche. Zum anderen wurde die elektronische Struktur an der Grenzfläche zwischen zahlreichen vielversprechenden N-Heteropolyzyklus Halbleitern, wie einem Porphyrine, einem N-Heteroacene und verschiedenen N-Heteroperopyrenen, und Au(111) ermittelt. Die Untersuchungen an den N-Heteroperopyrenen stechen heraus, da bei ihnen eine Bandausbildung zwischen delokalisierten Metallbändern und lokalisierten Molekülorbitalen beobachtet wurde, welche eine effiziente Ladungsträgerinjektion zwischen den Materialien begünstigen sollte.

Contents

Abstract	3
Kurzzusammenfassung in deutscher Sprache	5
1. Introduction	9
2. Theory and Basics	13
2.1. Metal/Organic Interfaces	13
2.1.1. Au - Surface Structure and Electronic Bands	13
2.1.2. Organic Semiconductors - Electronic Structure	20
2.1.3. The Electronic Structure at Metal/Organic Interfaces . .	23
2.2. Singlet Fission	26
3. Experimental Methods and Setup	29
3.1. Temperature Programmed Desorption	29
3.2. Photoemission Spectroscopy	31
3.3. Experimental Setup and Sample Preparation	35
3.3.1. UHV Chamber	36
3.3.2. Laser Setup	37
4. Characterization of the bare Au(111) Surface	41
5. Singlet Fission at the TIPS-Pentacene/Au(111) Interface	45
5.1. TIPS-Pentacene: A Soluble Pentacene Derivative	45
5.2. Sample Preparation and Coverage Estimation of TIPS-Pentacene on Au(111)	46
5.3. Electronic Structure and Excited State Dynamics	49
6. Electronic Structure of N-Heteropolycyclic Molecules at the Metal-Organic Interface	57
6.1. Porphyrins: Matured Molecules for Future Applications	58
6.2. Sample Preparation and Coverage Estimation of Fe-tetra- pyridil-porphyrin on Au(111)	61

Contents

6.3. Electronic Structure at the Fe-tetra-pyridil-porphyrin/Au(111) Interface	63
6.4. Arrow-shaped N-Heteroacenes: Potential n-type Organic Semiconductors	70
6.5. Sample Preparation of the arrow-shaped N-Heteroacene on Au(111)	71
6.6. Electronic Structure of the arrow-shaped N-Heteroacene/Au(111) Interface	73
7. Band Formation at the Metal/Organic Interface	79
7.1. Tetraazaperopyrene: A promising n-type Organic Semiconductor	80
7.2. Sample Preparation and Coverage Estimation of Tetraazaperopyrene on Au(111)	83
7.3. Electronic Structure of the Tetraazaperopyren/Au(111) Interface	86
7.4. Dispersions in Molecule-Induced States	90
8. Conlusion and Outlook	95
List of Figures	101
List of Acronyms	103
Appendix	107
A. Additional TIPS-Pn Measurements	107
B. Additional FeTPyP Measurements	111
C. Additional TIPS-BAP Measurements	115
D. Additional TAPP Measurements	118
Bibliography	127
List of Publications, Conference Contributions and Supervised Theses	155

1. Introduction

Semiconductor-based devices are omnipresent in our everyday electronic equipment. Up to today, silicon is the most common semiconductor used, e.g. in microelectronics or conventional solar cells, but during the last decade organic semiconductors gained more and more of importance [1–4], in particular due to their potential applications in (opto)electronic devices such as organic light emitting diodes (OLEDs) [5–13], organic field effect transistors (OFETs) [8, 10, 14–20] and organic solar cells (OSCs) [21–27]. Several advantageous of organic semiconductors such as low weight, low costs, transparency, flexibility, and easy processing by solution-based printing or evaporation led to the usage in various fields, e.g. displays, sensors and data storages [9, 11, 13, 15, 16, 28–37]. Easy to perform modifications of the organic semiconductors additionally open the possibility to tune the materials for individual needs [38–40]. To do so purposeful, a fundamental comprehension of the underlying photophysics and chemistry is crucial which led to major research efforts in both academic research institutions and industry [39].

Organic films only show a low density of thermally excited charge carriers, since organic semiconductors generally have a wide band gap in comparison to inorganic semiconductors [41, p. 3]. Therefore, efficient charge injection from metal electrodes into the organic semiconductors and *vice versa* is needed to achieve high currents. It follows that the performance of devices is strongly influenced by the charge carrier injection at the interfaces between electrode and organic semiconductor, but still much work is required to fully understand the underlying mechanisms [42–48]. However, it is obvious that this charge carrier injection depends on the electronic properties of the organic/metal interface [49–54]. Hybridization of molecular orbitals can lead to band formation as it has been found in some molecular crystals [55–58]. The same is valid for the hybridization between delocalized substrate metal bands and localized molecular orbitals of attached molecules, but so far only for strongly interacting adsorbate-substrate systems this kind of band formation was predicted [59–62]. This band formation at the interface is expected to foster efficient charge transfer between the electrode and the organic semiconductor.

1. Introduction

The purpose of this thesis is to investigate fundamental aspects of the metal/organic interface and in thin adsorbate layers, specially regarding the electronic properties, such as the electronic structure, excited state dynamics, hybridization and band formation. A valuable tool to do so is the two-photon photoemission spectroscopy (2PPE) which is a surface sensitive technique enabling the investigation of occupied and unoccupied electronic states, including excitonic states and transport levels [63–68]. Additionally, it gives access to excited state dynamics *via* femtosecond (fs) time-resolved 2PPE (TR-2PPE) and is able to observe dispersions (degree of electron localization/delocalization) *via* angle-resolved 2PPE (AR-2PPE). Conventional ultraviolet photoelectron spectroscopy (UPS) can additionally help to complement the picture of the occupied electronic states at interfaces, while temperature-programmed desorption (TPD) can give further information about adsorbates coverages and enables reproducible and well-defined sample preparations [64, 65, 69].

One of the most common organic semiconductors is pentacene showing high-charge carrier mobilities and a band gap within the visible region [53, 70–72]. Unfortunately, pentacene is very sensitive to oxidations and shows a low solubility, making a solution based processing difficult [73]. Anthony *et al.* [74] could overcome these drawbacks by introducing (triisopropylsilyl)ethynyl (TIPS)-groups into the central position of the pentacene backbone. The resulting 10,17-bis((triisopropylsilyl)ethynyl)-pentacene (TIPS-Pn) shows an increased solubility, stability, and a favorable self-assembly. The higher members of the acene family are known to undergo a singlet fission process, where one photon creates two charge carriers *via* the formation of two triplets on two adjacent molecules from one excited singlet state [75–77, 77–85]. This makes TIPS-Pn a promising candidate for applications in organic semiconductor based photovoltaics. The influence of the metal electrode on the singlet fission process was so far unknown and therefore, a detailed investigation of the excited state dynamics at the TIPS-Pn/Au(111) interface was carried out in the framework of this thesis, revealing a strong coverage dependent quenching effect regarding the singlet fission dynamics.

Acenes with more than five linearly fused rings have also shown to be promising organic semiconductors, but the lack of stability and solubility is even bigger [86–89]. They can be stabilized by keeping the recipe for success and by attaching TIPS-groups. Further stabilization can be achieved by attaching two further benzene rings forming an arrow-shaped molecule [87]. However, during the last years a vast pool of organic semiconductor building blocks has been developed, but the majority of these are, like the acenes, p-type

semiconductors. An approach to synthesize potential n-type semiconductors is the incorporation of nitrogen atoms into the acene backbone, lowering the energy of the frontier orbitals and additionally stabilizing the molecules [90–95]. The combination of both approaches leads to a new promising molecule, the 10,17-bis((triisopropylsilyl)ethynyl)dibenzo[a,c]naphtho[2,3-i]phenazine (TIPS-BAP). This kind of frontier orbital stabilization, of course, is not only valid for the acenes, and therefore, also further N-heteropolycycles are promising n-type semiconductors. The 1,3,8,10-tetraazaperopyrenes (TAPPs), a relative new class of N-heteropolycycles, have already shown promising results in various applications, and their material properties could be tuned widely [38, 96–106]. Long before human kind another diverse group of N-heteropolycycles has been developed by nature. Porphyrins, consisting of four pyrrole rings, cyclic connected via methine groups, and various substituents, form a class of flexible and tunable N-doped macrocycles and are widespread as key-units in biological processes. This natural class of molecules was expanded by synthetic affords, and due to their easily tunable electronic properties, they are suitable to complement the pool of organic semiconductor building blocks [107–115]. One promising candidate from this class, with possible application in molecular switches, electronics and spintronics, is the Fe-5,10,15,20-tetra-pyridil-porphyrin (FeTPyP) [65, 116].

Since knowledge about the electronic properties of the metal/organic interface is fundamentally important for the purposeful development of efficient organic molecule based devices, this work studied thin layers of several promising N-heteropolycycles adsorbed on the Au(111) surface *via* 2PPE, UPS, and TPD. The energy levels of several molecular states of TIPS-BAP, FeTPyP, TAPP, 2,9-bis(trifluoromethyl)-1,3,8,10-tetraazaperopyrene (TAPP-(CF₃)₂), and 2,9-bis(perfluoropropyl)-1,3,8,10-tetraazaperopyrene (TAPP-(C₃F₇)₂) have been determined with respect to the Fermi level of the gold surface. This includes transport levels and excitonic states, and thus transport gaps, optical gaps and exciton binding energies could be concluded. Additionally, work function shifts were observed during adsorption.

For the TAPP derivatives adsorbed on the gold substrate, it should be highlighted that dispersing interface related bands have been revealed. They are proposed to origin from a hybridization of delocalized metal bands and localized molecular orbitals. This kind of band formation at the interface, so far, was only obtained for a small number of metal/organic interface systems [59–62]. Namely these were F₄TCNQ and TTF on Au(111) and PTCDA and NTCDA on Ag(110). For all of these systems, an initial charge transfer between the metal and the organic takes place, resulting in charged ions at the

1. Introduction

metal/organic interface, and therefore, a further charge injection at the interfaces might be hindered. An interface with more weakly interactions between the molecules and the metal, also showing band formation, therefore would be advantageous for device applications. That is exactly the case for the TAPP-derivatives adsorbed on Au(111), as hints for rather weak interactions between the molecules and the metal are obtained, and a charge transfer could be largely excluded.

The research addressed in the framework of this thesis is located in between the scientific effort to synthesize new organic materials for future applications and the development of high efficient devices. The presented results therefore can give feedback to improve and control the synthetic aims and deliver basic information helping to fabricate new and better organic semiconductor based devices.

Besides the introduction and the conclusion, the present thesis contains six main chapters. Chapter 2 starts with a basic introduction into the theoretical background which is important for the understanding of the interpretations and conclusions made. A brief description of electronic bands, their formation and the dispersions of electrons is given, besides a short introduction into the electronic structure of the gold substrate. Further, basic ideas regarding the electronic structure at organic semiconductor/metal interfaces are presented and finally, the so called singlet fission process is explained. The experimental methods and setup are described in Chapter 3 followed by a characterization of the bare Au(111) surface in Chapter 4. Chapter 5 then focuses on the investigation of the TIPS-Pn/Au(111) interface and the obtained singlet fission dynamics. The electronic structure of two N-heteropolycycles, the FeTPyP and the TIPS-BAP at the Au(111) interface is presented in Chapter 6, followed by the investigations of the interface between different TAPP derivatives and Au(111), revealing band formation in Chapter 7.

2. Theory and Basics

In this chapter fundamental theoretical topics are discussed to give a proper basis for the results and interpretations presented in this thesis. The surface geometry and the electronic structure of metal surfaces is treated with a main focus on the gold band structure and the Au(111) metal surface. Gold is one of the most noble metals accompanied by low reactivity due to its filled d-shell. This makes it to an ideal substrate for the investigations of metal/organic interfaces. Besides the description of the bare metal a brief introduction into the electronic structure of organic semiconductors is given, and the basic nomenclature of orbitals and electronic states will be reviewed. This is followed by a short view on metal/organic interfaces and effects influencing the electronic structure of the involved compounds. Finally, the so-called singlet fission process is explained.

2.1. Metal/Organic Interfaces

2.1.1. Au - Surface Structure and Electronic Bands

Electronic Bands and Dispersions

Metals are distinguished by their typical chemical bond where, in a simplified approach, their valence electrons can move freely within the lattice of the metal ions. The *Sommerfeld-Theory* or *free electron model* assumes that these electrons behave like an electron or Fermi gas in a constant potential. Following from this approach we can describe an electron by the *particle in a box model* with a steady state Schrödinger equation, where only the kinetic energy is taken into account.

$$-\frac{\hbar^2}{2m_e}\Delta\Psi(\mathbf{r}) = E\Delta\Psi(\mathbf{r}) \quad (2.1.1)$$

Here \hbar is the reduced *Planck constant*, m_e the electron mass, Δ the *Laplace Operator*, $\Psi(r)$ the electronic wave function and E the energy eigenvalue. Solving

2. Theory and Basics

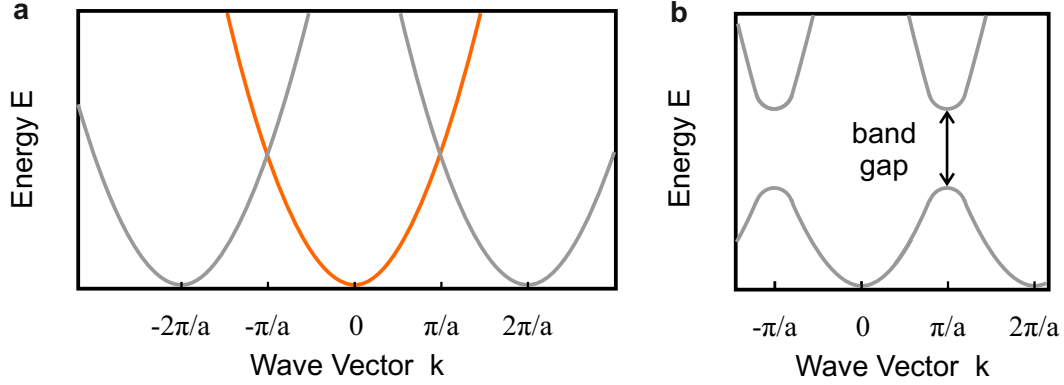


Figure 2.1.: (a) Periodically obtained parabolic dispersion of an electron in a nearly-zero periodic potential. The parabolic dispersion of a free electron is highlighted in orange. (b) Dispersion curves for electrons in a periodically non-zero potential. At the edges of the Brillouin zone energy gaps occur, leading to electronic bands and band gaps. \mathbf{a} denotes the lattice vector. Figure adapted from Ref. [117, p. 303, 309].

this equation for Ψ being a plane wave

$$\Psi(\mathbf{r}) = \frac{1}{\sqrt{V}} e^{i\mathbf{k}\mathbf{r}}, \quad (2.1.2)$$

with V being a normalization factor, leads to the wave vector \mathbf{k} dependent energy eigenvalues

$$E(k) = \frac{\hbar^2 k^2}{2m_e} \quad (2.1.3)$$

which gives us the parabolic dispersion relation for free electrons as displayed in figure 2.1 (a) (orange curve). However, the potential in a metal is not constant, as assumed above. In fact the lattice of the metal ions build up a periodic potential, with $\tilde{V}(\mathbf{r}) = \tilde{V}(\mathbf{r} + \mathbf{R})$, where \mathbf{R} is a random lattice vector. For $\tilde{V}(\mathbf{r})$ being nearly zero, the energy eigenvalues of the Schrödinger equation

$$\left[-\frac{\hbar^2}{2m_e} \Delta + \tilde{V}(\mathbf{r}) \right] \Psi(\mathbf{r}) = E \Delta \Psi(\mathbf{r}), \quad (2.1.4)$$

are given by

$$E_{\mathbf{k}} = E_{\mathbf{k}+\mathbf{G}} = \frac{\hbar^2}{2m_e} |\mathbf{k} + \mathbf{G}|^2, \quad (2.1.5)$$

with \mathbf{G} being the reciprocal lattice vector. With the smallest reciprocal lattice vector $\mathbf{g} = 2\pi/\mathbf{a}$ the parabolic dispersion obtained for free electrons repeats periodically as shown in figure 2.1 (a). Increasing the potential $\tilde{V}(\mathbf{r})$ to a finite strength leads to energy gaps at the edges of the Brillouin zone as displayed in figure 2.1 (b). As a consequence there are energetic regions with and without electrons. The former are called electronic bands and the latter are called band gaps. Summarized we can conclude that dispersions of electrons within a Brillouin zone are the direct consequence of nearly free moving electrons in a periodic lattice potential, as it is e.g. the case within a metallic band. The preceding description of electronic bands and dispersions can be found in various solid state physics books [117–120] and is treated there in more detail.

Metal Surface States

Moving from a bulk material to its surface profound changes of the electronic structure can occur. At the surface of a solid the periodicity and symmetry are interrupted and chemical bonds are unsaturated. This leads to surface specific electronic states, e.g. *surface states* and *image potential states*, which shall be shortly introduced at this point. First theoretical descriptions of surface states were made by Tamm [121] and Shockley [122]. The Shockley surface state (SS) is based on the nearly free electron approximation, sufficiently describing the phenomena at metal surfaces [123, p. 266]. At the metal surface the lattice potential of the bulk is abruptly increased due to the transition to the vacuum energy. Simplified this transition can be regarded as a step like potential, where two different localized solutions can be found for the real part of the Schrödinger equation (see figure 2.2). On the one hand the bulk type solution, a standing Bloch wave, is matched to an exponential decay propagating into the vacuum. On the other hand a surface type solution localized within a couple of Ångström at the surface, with an exponentially damped vibration propagating into the bulk and an exponential decay propagating into the vacuum [123, p. 266]. The energy eigenvalues of the SS are located within the bulk band gaps and their lowest energy can be found around the Γ point, as they show a dispersion depending on k_{\parallel} , while due to their localization at the surface there is no dependence on k_{\perp} [124, p. 403]. The localization of the wave function partly outside the surface leads to a sensibility of the SS with respect to defects like steps, islands, adatoms, and adsorbates. This kind of defects can lead to a shift in energetic position, broadening, intensity reduction or complete quenching [125–133].

2. Theory and Basics

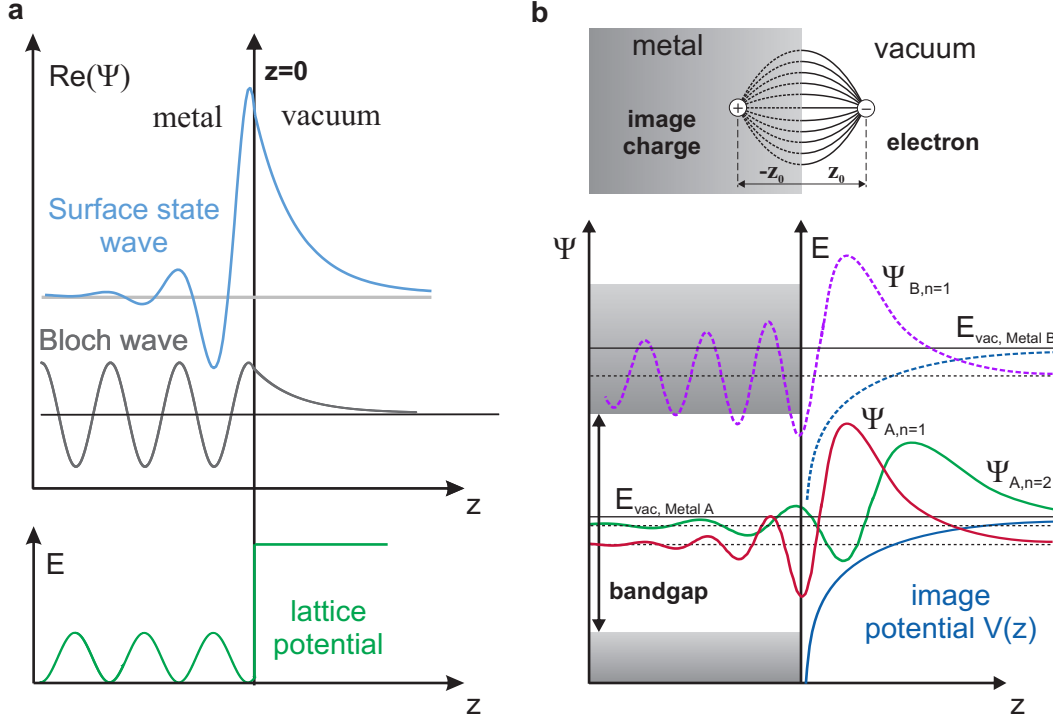


Figure 2.2.: (a) Illustration of a simplified one-dimensional lattice potential at a metal surface. At the edge of the solid crystal the potential increases immediately to the vacuum energy. The real parts $Re(\Psi)$ of the two possible interface solutions of the Schrödinger equation are presented above. On the one hand a standing Bloch wave, matched to an exponentially decaying tail in the vacuum and on the other hand a surface state wave function decaying exponentially into the vacuum as well as the bulk. Figure adapted from Ref. [123, p. 267]. (b) Sketch of the interactions between an electron in front of a metal and its image charge. The image potentials $V(z)$ and the wave functions $\Psi_{n=1}$ for two different metals are shown. For the first metal the energy eigenvalue is located in the band gap, while for the second metal it is located in the bulk band region above the gap. Figure adapted from Ref. [134].

Besides the SS, a further kind of surface related states occur at metal surfaces, which are the image potential states (IPs). As illustrated in figure 2.2 (b) they can be described by an electron in front of the metal surface bound by its positive image charge inside the metal [135, p. 285], [124, p. 401], [134]. The interaction between the electron and its image charge leads to an attractive

image force

$$F(z) = -\frac{e^2}{4\pi\epsilon_0} \frac{1}{(2z)^2}, \quad (2.1.6)$$

and therefore an electron in front of the surface with an energy below the vacuum energy (E_{vac}) can be bound by an attractive Rydberg like potential

$$V(z) = -\frac{1}{4} \frac{e^2}{4\pi\epsilon_0} \frac{1}{z}, \quad (2.1.7)$$

where e is the elementary charge, ϵ_0 is the vacuum permittivity, and z is the distance to the surface [134]. The factor $\frac{1}{4}$ directly results from distance $2z$ between the electron and the image charge. As in the case of an electron in an atom, the electron localized in the IPS can take specific energy eigenvalues in respect to E_{vac} .

$$E_n = E_{vac} - \frac{0.85}{(n+a)^2} \quad (2.1.8)$$

Here n is the IPS quantum number and a is the so called quantum defect. The latter corrects the energy eigenvalues of the IPS, as a consequence of phase matching between the Coulomb wave function and the Bloch wave function of the bulk at real surfaces, where the IPS wave function penetrates into the bulk region as an evanescent wave [136, 137]. To enable efficient trapping of electrons in the IPS, energy eigenvalues within the band gap of the bulk material are needed, but IPS have also been observed for metals with their vacuum energy, and accordingly IPS energy eigenvalues, within a bulk band region [134, 138, 139]. These special cases are called *resonance image potential states*. The IPSs degenerate with bulk states in the form of weak hybrid states. The intensities of these IPSs are much weaker compared to their band gap counterparts and the electrons can relax easily into the bulk, resulting in ultrashort lifetimes [138, 139]. Electrons bound in the IPS can move freely in front of the surface and therefore they show a dispersion parallel to the surface (\vec{k}_{\parallel}) with an effective mass of $m^* \approx 1.0 - 1.7 m_e$ [138, 140].

$$E_n = -\frac{0.85}{(n+a)^2} + \frac{\hbar^2 k_{\parallel}^2}{2m^*} \quad (2.1.9)$$

Au(111)

Gold is a very noble metal and due to its filled d-orbitals it shows comparable low reactivities. This makes it an ideal substrate for the investigation of adsorbate covered surfaces. The gold crystal is based on a face-centered cubic (fcc)

2. Theory and Basics

packing of the atoms. The Au(111) plane, however is not thermodynamically stable in its original bulk form, when located at the surface. In this case it undergoes a reconstruction forming a *herringbone* $-(22 \times \sqrt{3})$ surface structure, where the gold atoms are compressed, placing 23 atoms onto 22 grid places. The herringbone structure is characterized by a changing pattern of a hexagonal closed packed (hcp) and fcc packed lattice [141, 142]. A calculated band structure of the Au(111) surface is presented in figure 2.3 [143]. The sp-band and the Shockley surface state show a dispersion parallel to the surface around the Γ -point of the first Brillouin zone. The calculations agree with UPS data by Kevan and Gaylord [144]. For Au(111) the effective masses are known to be $m^* \approx -0.4 m_e$ for the sp-band, and $m^* \approx -0.3 m_e$ for the SS. In respect to E_{Fermi} the sp-band is located at $E(sp) \approx -0.9 eV$ while the SS is to be found at $E(SS) \approx -0.45 eV$ [126, 130, 144–146]. The d-band dispersion parallel to the surface is negligible [143] but they show dispersion perpendicular (k_{\perp}) to the surface [147]. The band gap at the Γ -point around Fermi is reported to be located approximately from $-1.0 eV$ to $3 eV$ with respect to the Fermi level [148]. With a high quality Au(111) surface work function of $5.5 eV$ is obtained. The IPSs are thus located above the band gap, and therefore are resonance IPS, which own a quantum defect of approximately zero [134].

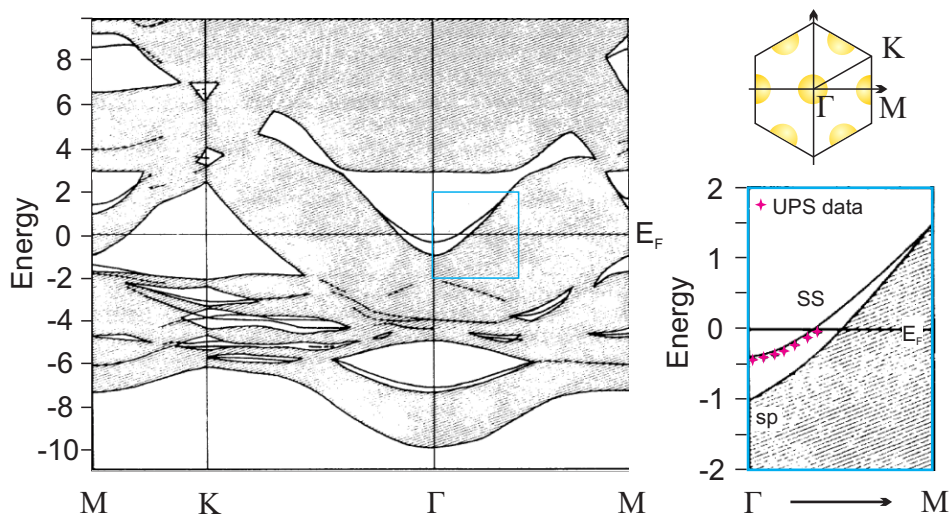


Figure 2.3.: Electronic structure of an Au(111) surface calculated with the top layer in a fcc stacking sequence site. Solid and dashed lines display surface states and resonances in the surface band structure. In the gray areas bulk states can exist. The blue marked area is shown enlarged in the lower right. For verification of the calculations UPS data from Kevan and Gaylord [144] have been added. The upper right shows the first 2D Brillouin zone of the Au(111) surface. Figure adapted from Ref. [143].

2.1.2. Organic Semiconductors - Electronic Structure

Band Formation in Organic Molecules

The linear combination of two atomic orbitals leads to a new set of two molecular orbitals. From this simplified view, the metallic band formation can be explained easily, as being a linear combination of n atomic orbitals forming a density of states (DOS) out of n molecular orbitals. A metal thus can be viewed as a molecule of n atoms and for $n \rightarrow \infty$ a quasi continuously band results. A metal, only consisting of one sort of atoms in a close distance and a well-ordered structure, easily meets the requirements of the linear combination of atomic orbitals (LCAO)-approximation [149, p. 685]. This idea can be transferred to large molecules also forming a quasi continuously DOS, and thus an energy band. This kind of intramolecular band formation is known for a variety of molecules [150–156], while an intermolecular band formation often does not meet the requirements of the LCAO-approximation. Especially the necessary orbital overlap for orbitals with the same symmetry is often not given with adjacent molecules. Nevertheless, there are several examples for especially π -conjugated molecular crystals showing a band formation as can be proven by delocalized electrons [55–58]. The idea of intermolecular band formation is illustrated by figure 2.4 for ethylene.

Organic Semiconductors

The model of energy bands resulting from the LCAO-approximation of countless atoms or molecules is a valid basis to understand the differences of between metals, semiconductors, and insulators. The linear combination of several occupied orbitals lead to an occupied band, while unoccupied orbitals form an unoccupied band. The lowest unoccupied band is commonly referred to as the conduction band, while the highest occupied band is called the valence band. For metals valence- and conduction band overlap, leading to free electron movement, and thus to their typical properties as metallic color, and high electrical and thermal conductivity. For the case of non overlapping valence- and conduction bands two different cases are distinguished on the basis of the gap size. For high energy gaps no conduction can be observed and so these materials are insulators. For lower gap sizes, where free charge carriers can be obtained *via* excitation or by doping, the materials are assigned to be semiconductors.

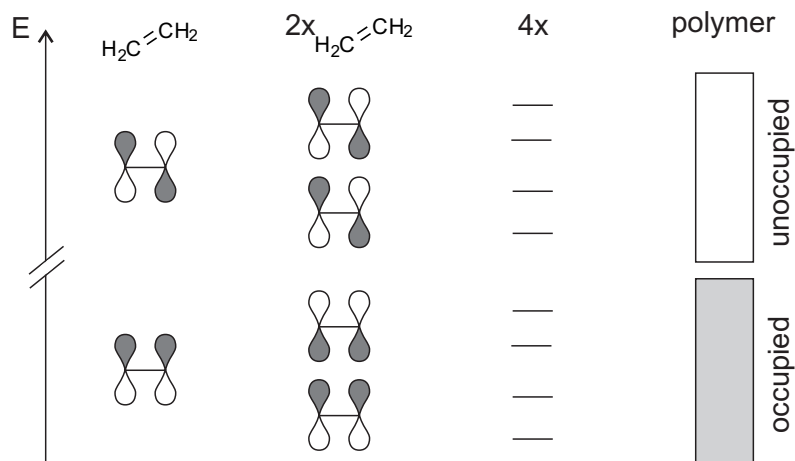


Figure 2.4.: Illustration of the linear combination of the molecular orbitals of ethylene forming a new set of bonding and antibonding orbitals. With increasing number of molecules involved the density of states is increasing till valence and conduction bands are formed. Figure adapted from [58].

Organic semiconductors are molecule based materials with an *optical gap*, as “the lowest electronic transition accessible via absorption of a single photon” [157], located between 1.5 to 3 eV [39]. This optical transition (e.g. $S_0 \xrightarrow{h\nu} S_1$), creating an exciton, thus is accessible by visible light (700 – 400 nm) [158]. Saturated organic molecules do not meet this requirement, but in contrast larger π -conjugated organic molecules and polymers have an optical gap in the required energy range [39, 158]. Organic semiconductors have, depending on the point of view, big advantages. Their energy gap can be easily tuned by changing the size of the molecules, by adding electron donating or withdrawing substituents, or inserting heteroatoms. Further their packing or crystal structure can be modified and metals can be intercalated or coordinated. With this a great variety of materials can be created and adapted to the respective use. Further thin, flexible and lightweight layers can be achieved making organic semiconductors a powerful complement to the classical inorganic semiconductors.

Energy Gaps and Excitons

The energy gap between the highest occupied molecular orbital (HOMO) and the lowest unoccupied molecular orbital (LUMO) is an important parameter

2. Theory and Basics

for organic semiconductors. However, different terms as fundamental gap, optical gap, HOMO-LUMO gap, transport gap, and band gap, are often not used precisely in literature. A good overview provide the remarks of Bredas [157], which are briefly summarized here. From a theoretical point of view the molecular orbitals (MOs) are stationary one-electron wave functions, while measurements access ionization potentials (UPS, 2PPE, x-ray photoelectron spectroscopy (XPS)), electron affinities (scanning tunneling spectroscopy (STS), 2PPE, inverse photoemission spectroscopy (IPS)) and optical transitions (ultraviolet-visible spectroscopy (UV/Vis), 2PPE, high resolution electron energy loss spectroscopy (HREELS)). Regarding a single molecule, the *fundamental gap*, is defined as the difference between ionization potential (IP) and electron affinity (EA), while the optical gap equals the energy needed for the lowest excitation of a molecule induced by the absorption of a single photon (e.g. $S_0 \xrightarrow{h\nu} S_1$). According to Bredas [157] the *HOMO-LUMO gap* is the energetic difference between the calculated frontier MOs, and therefore is an approximation of the fundamental gap. Moving from a single molecule to organic molecular materials, electronic bands can be formed as described above. In this case the energetic difference between the IP and the EA is referred to as the *band gap* or *transport gap*. However, the optical excitation of an organic material in general leads to the formation of a bound electron-hole pair, called an exciton. For the description of excitons usually two different models are considered. On the one hand the so-called *Mott-Wannier excitons* describing electron-hole pairs with large distances between electron and hole, which is the typical case in inorganic semiconductors. Due to screening effects by the material they show low binding energies (≤ 0.1 eV) [118, p. 390]. On the other hand, in organic molecules, rare gases and ionic crystals, much stronger and more localized electron-hole pairs are observed. These so-called *Frenkel excitons* show binding energies up to 1.0 eV and are located directly at one atom or within one molecule [118, p. 390][157]. The binding energy (E_B) of an exciton is defined as the energy difference between the transport gap and the excitons excitation energy (e.g. the optical gap of the organic molecular material). For an illustration refer to figure 2.5.

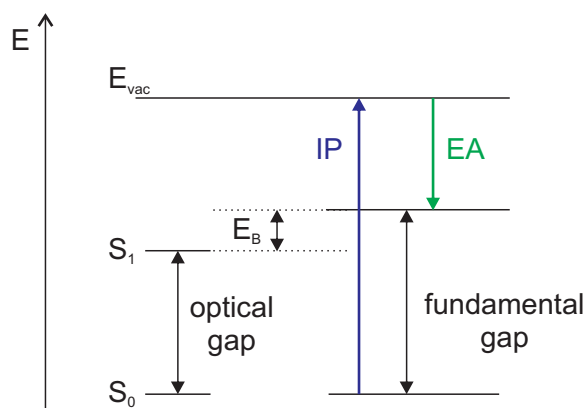


Figure 2.5.: Illustration of the gap energies and the exciton binding energy (E_B) for an organic molecule. The optical gap is the energy difference between the ground state (S_0) and the lowest excited singlet state (S_1), while the fundamental gap is the difference between the IP and the EA. Figure adapted from Ref. [157]

2.1.3. The Electronic Structure at Metal/Organic Interfaces

For electronic devices the interfaces between semiconductors and metals play a crucial role. Metal-semiconductor junctions are commonly used as ohmic or schottky contacts and their interface behavior can be described by well-established models [118, 135, 159].

However, for organic semiconductor/metal interfaces the picture needs to be refined. Here two models will be presented, which, depending on the point of view, can describe the interplay between organic molecules and the metal surface. On the one hand the *induced density of interfacial states* (IDIS) model, and on the other hand the *hybrid charge transfer* model. While the first is more inspired by the band related interface picture of inorganic semiconductors, the second is more focused on an orbital based view, as it is the common picture for molecules. The first model was developed by H.Vázquez and coworkers [160–162] focusing on the interactions of Au with different organic semiconductors, as Au being a metal with weak interactions to adsorbates. In this model the charge neutrality level (CNL), as being an “effective” Fermi level for molecules, is introduced (see figure 2.6). The CNL level can be understood as a kind of electronegativity marker of the adsorbed molecule [41, p. 28]. Calculating the CNL, from IP and EA it is expected to be found at the midgap between HOMO and LUMO of the molecule. However, it is necessary to take all energy levels

2. Theory and Basics

and the interaction with the surface into account while calculating the CNL. The position of the CNL is obtained by integrating the molecular density of states $\rho_S(E)$ up to charge neutrality conditions.

$$\int_{-\infty}^{CNL} \rho_S(E) dE = N, \quad (2.1.10)$$

N here denotes the number of electrons in the neutral molecule. The CNL is therefore often found to be closer to the LUMO, than to the HOMO due to the higher density of states around the latter [41, p. 29,30].

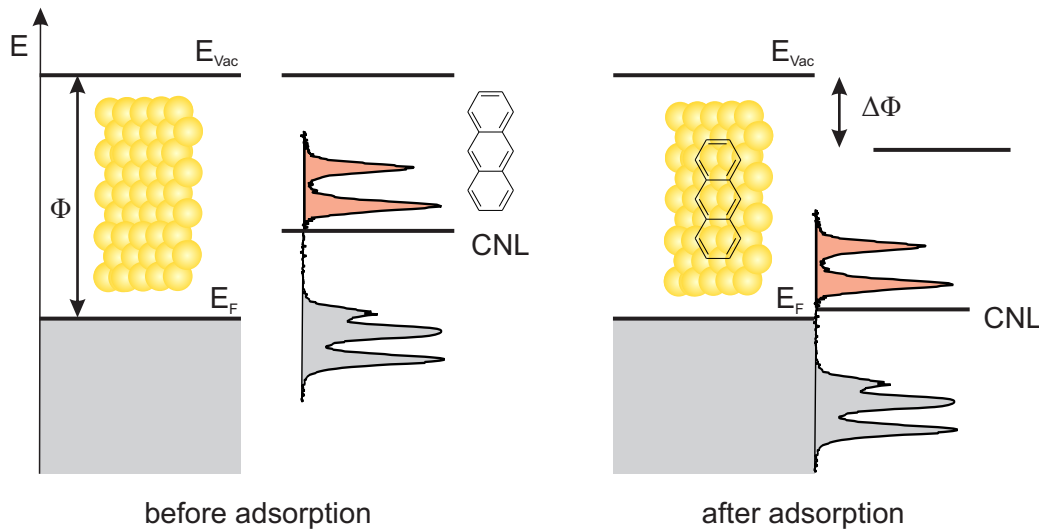


Figure 2.6.: Illustration of the induced density of interfacial states model. During adsorption the charge neutrality level (CNL) and the Fermi level align leading to a shift of the work function (Φ). CNL is not necessarily located at the mid-gap as the higher density of states around the HOMO pushes it upwards towards the LUMO [160].

When molecule and metal get in touch, electron charge flows between the compounds in a way, that the initial misalignment between Fermi energy (E_F) and CNL gets screened, leading to a shift of the work function at the interface in comparison to the work function of the isolated metal (see also below) [41].

The second model relies on the molecular orbital theory and is actually not only valid for metal/organic interfaces, but also for organic/organic or organic/inorganic interfaces. This model does not describe work function changes

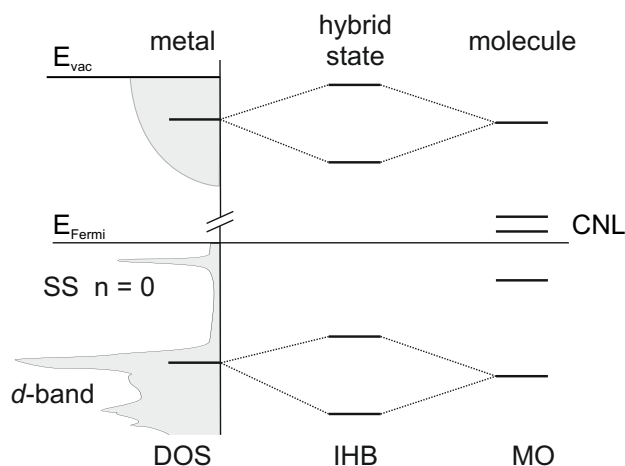


Figure 2.7.: Mixing of metal substrate bands with molecular orbitals due to adsorption on the basis of the LCAO theory. DOS: density of states; IHB: interface hybrid band; MO: molecular orbitals, CNL: charge neutrality level; SS: Shockley surface state.

during adsorption, but can be useful to explain new arising hybrid orbitals or bands at the interface. Here metal bands, as being an infinite number of linear combined atomic orbitals (AOs), form so called hybrid orbitals (often referred to as interface states) via linear combination with a molecular orbital. Depending on the strength of the interactions between the metal and the molecules, these hybrid orbitals can show weakly or strongly altered properties, compared to the single component orbitals or bands. For example with this picture an interface band formation under participation of a molecular orbital and a metal band can be explained [61].

Work Function of Metal/Organic Interfaces

The work function is the minimum energy which is needed to remove an electron from the bulk into the vacuum $\Phi = W - E_F$. For metal surfaces it is mainly determined by the bulk chemical potential and the surface dipole, which in turn results from electrons spilling out of the surface into the vacuum [51, 163]. Work function changes at metal interfaces during the adsorption of molecules are an often observed phenomena [61, 67, 68, 128, 164, 165]. These changes are a result of multiple effects. As explained above the Fermi and CNL level alignment leads to a shift of the work function. The strength of the Fermi level shift, and thus the work function change, is determined by the difference between Fermi and CNL level, but also the generation of an

2. Theory and Basics

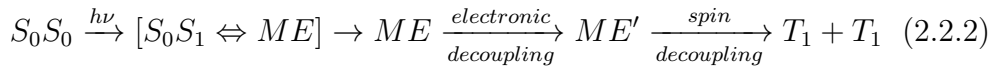
interface dipole during alignment can influence the shift [162]. Besides the interface dipole, molecular dipole moments perpendicular to the surface also contribute to the shift as well as the so called push-back effect (also known as “cushion effect” or Pauli repulsion) [51, 165–168]. The adsorption of organic molecules “pushes” electrons back into the surface, reducing the upper mentioned original surface dipole. Summarized it can be said, that the work function is combination of the bulk potential and an overall dipole moment influenced by molecular dipoles, the intrinsic surface dipole, the push-back effect, and interfacial dipoles.

2.2. Singlet Fission

The efficiency of single junction photovoltaic solar cells is theoretically limited by 32 %. This prediction was formulated by Shockley and Queisser in 1961 and results from incomplete absorption, radiative recombination, and, as the main part, waste heat as a consequence of the difference between photon energies and band gap [169]. A possibility to overcome the theoretical limit is a multiple exciton generation, as it is the case for the so called *singlet fission (SF) process*. The SF process already was the object of several studies, but still some points are not fully understood by now [170–172]. In an simplified view of the SF process an optically excited molecule (S_1) interacts with an adjacent ground state molecule forming a so called multiexciton (ME) state, which then decays into two separated triplets in an overall spin allowed process [80, 170–172]. In contrast to the orders of magnitude slower intersystem crossing, the spin angular momentum is conserved in SF.



Recent theoretical [81, 173, 174] investigations and experimental results [80, 82, 175–177] led to a deeper understanding of this process.



For [$E(S_1) \approx 2 * E(T_1)$] the excitation of the Frenkel exciton forms a coherent superposition of the S_1 and the ME state, which decays, in the case of exoenergetic SF on an ultrafast timescale below 300 fs, into the ME state. The ME is a correlated triplet pair $^1(\text{TT})$ with an overall singlet character, but time resolved spin resonance spectroscopy revealed the additional formation of triplet pair states of quintet character $^5(\text{TT})$ [175, 178]. However, the ME formation

can take place via a coherent or incoherent pathway and the influence of charge transfer (CT) states on the ME state is a discussed topic [78, 80, 173, 174]. Further there are observations of strong vibronic and vibrational couplings mediating the ultrafast ME formation [75, 179]. Figure 2.8 illustrates the frontier orbitals of a capable molecule during the process simplified. At this point it also should be mentioned, that the SF involves more than just two adjacent molecules, as the singlet state needs to be delocalized for an efficient process [172, 180]. In general, it is necessary that the involved molecules show a defined order and packing accompanied by suitable orbital overlap to achieve efficient SF rates and ultrafast dynamics [170, 171].

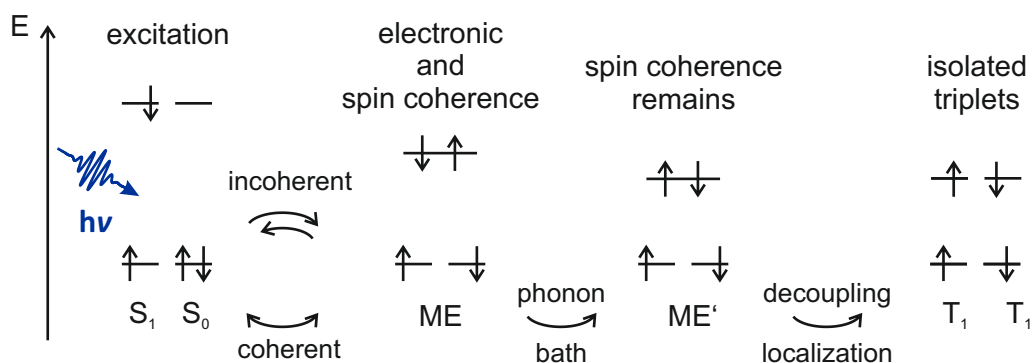


Figure 2.8.: Simplified illustration of the frontier orbitals during the singlet fission process. S_n : singlet state, ME: multiexciton state, T_n : triplet state.

The ME' state is formed by the loss of electronic coupling and coherence within a picosecond timescale [90, 172, 181, 182], while the spin coherence remains. Finally, the spin decouples and the ME' state localizes into separated triplet states ($T_1 + T_1$). SF was so far mainly observed in π -conjugated systems, as acenes are the most prominent candidates. Here Tetracene [75–77] is an example for endoenergetic SF ($E(S_1) \leq 2 * E(T_1)$), while Pentacene ($E(S_1) \geq 2 * E(T_1)$) [77–84] and Hexacene ($E(S_1) > 2 * E(T_1)$) [85] undergo exoenergetic SF. Endoenergetic SF competes with delayed fluorescence due to the reverse process of triplet-triplet annihilation or triplet fusion [183–186], while SF is dominant for exoenergetic systems.

3. Experimental Methods and Setup

In the following chapter the experimental techniques applied in the context of this thesis will be presented. Namely, temperature-programmed desorption (TPD), ultraviolet photoelectron spectroscopy (UPS) and two-photon photoemission spectroscopy (2PPE) were used to investigate multiple metal-organic interfaces. Subsequently, the experimental setup will be introduced.

3.1. Temperature Programmed Desorption

A suitable and well-established technique to investigate coverages and binding energies of adsorbed molecules on surfaces is the temperature-programmed desorption (TPD) [124, p. 685], [159, p. 429], [187]. While increasing the sample temperature with a constant heating rate in an ultra high vacuum (UHV) chamber, a quadrupole mass spectrometer (QMS) is used to detect desorbing molecules. Desorption is taking place for the molecules obtaining a thermal energy sufficient to overcome the binding energy (E_B) at the surface. A first approach to use TPD as a quantitative method to obtain these binding energies, was made by Redhead in 1962 [188]. By heating the sample with a constant heating rate ($\beta = dT/dt$), i.e. in a “programmed” way, the desorption rate (r_{des}) is

$$r_{des} = \frac{d\Theta_{ad}}{dt} = \Theta_{ad}^n \nu_0 e^{\frac{E_B}{k_B T}}, \quad (3.1.1)$$

with Θ the fractional coverage, n the reaction order, and ν_0 the rate constant. This directly leads to the *Polanyi-Wigner* equation, which gives a relationship between the desorption as a function of temperature and the binding energy.

$$\frac{d\Theta_{ad}}{dT} = \Theta_{ad}^n \frac{1}{\beta} \nu_0 e^{\frac{E_B}{k_B T}} \quad (3.1.2)$$

3. Experimental Methods and Setup

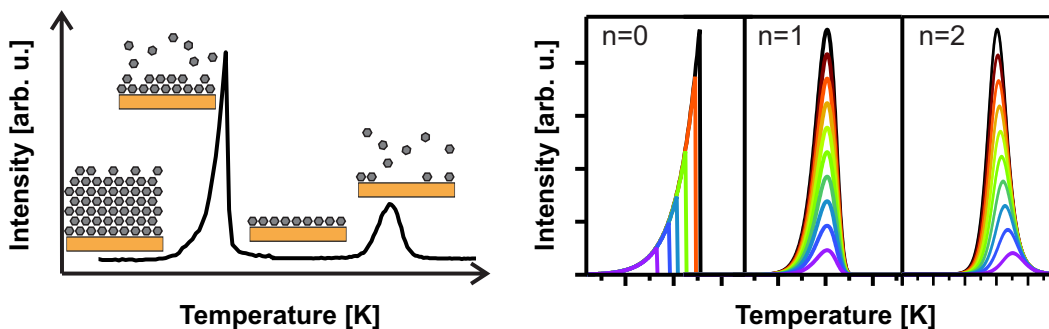


Figure 3.1.: Schematic illustration of temperature programmed desorption measurements. *Left*: A typical TPD spectrum of a molecule covered metal surface. The insets show models of the surface coverage at different temperatures during desorption. *Right*: On the basis of the *Polanyi-Wigner* equation calculated desorption spectra with a desorption order of $n = 0$ and $n = 1$ for coverages increasing from the purple to the black curve (adapted from [193]).

The reaction order is determined by the desorption mechanism and strongly influences the shape of the obtained TPD spectra as shown in figure 3.1. *Zero-order* desorptions, where the desorption rate is independent of the coverage, are usually obtained for multilayer coverages. The adsorption rate increases with increasing temperature until all adsorbates are completely desorbed and the rate abruptly falls to zero. The high temperature cut off depends on the initial coverage, as more molecules need more time to desorb from the surface. For monolayers, where a defined number of molecules are located at their adsorption sites *first-order* desorptions are obtained as long as adsorbate/adsorbate and adsorbate/substrate interactions are negligible. In this case the peak maximum is independent of the initial coverage. *Second-order* desorptions are the case for a recombinative desorption mechanism, where two adsorbates need to meet before they can get detached from the surface. For this reason the peak maximum shifts to lower temperatures for increasing coverages [124, p. 282]. TPD spectra can differ from this ideal behavior, as for lateral interactions between adsorbed molecules, ν_0 and E_B can become coverage dependent, resulting in peak shifts for varying coverages [189–192]. A so called pseudo-zero-order desorption is typical for attractive interactions, and a pseudo-second-order desorption is often obtained for repulsive interactions. On the right side of figure 3.1 a typical TPD spectrum obtained for molecules adsorbed on metal surfaces is shown. For a surface covered with multiple layers of molecules, a zero order desorption is observed at temperatures comparable to the sublimation temperature. The first layer in direct contact to the metal

surface in general is more strongly bound, thus desorbing at higher temperatures. This allows access to well-defined monolayer coverages by heating a multilayer covered surface to a temperature in between the multi- and monolayer desorption temperatures, as will be used frequently in the framework of this thesis. By comparing the integrals of the monolayer and the multilayer desorption peaks information about coverage can additionally be gained, as long as the molecules desorb intact. Further, detecting different molecular fragments can give insight into possible on surface reactions and desorption processes [194]. Overall, TPD is a basic tool in surface science allowing access to a wide range of information and can so serve as a suitable tool to investigate metal/organic interfaces.

3.2. Photoemission Spectroscopy

A valuable tool to investigate electronic structures at surfaces is the photoemission spectroscopy (PES). PES reaches back to first experimental observations of the photoelectric effect by Heinrich Hertz and Wilhelm Hallwachs in 1887 and the theoretical interpretations of Einstein in 1905. The interaction of photons of sufficient high energy with matter leads to the emission of electrons. These electrons have a specific kinetic energy (E_{kin}) depending on the materials work function (Φ), the incident photon energy ($E_{Ph} = h\nu$)¹, and the initial binding energy (E_B) of the electron with respect to E_F .

$$E_{kin} = E_{Ph} - \Phi + E_B \quad (3.2.1)$$

Based on this effect several experimental methods have been developed, from which ultraviolet photoelectron spectroscopy (UPS) and two-photon photoemission spectroscopy (2PPE) were conducted in the framework of this thesis, both being surface sensitive techniques and thus suitable for investigating the metal/organic interface. The surface sensitivity is a result of the small electron inelastic mean free path in solids described by the so called *universal curve*. Within PES it is common to term energetic levels, where the detected electrons originate from, as initial, intermediate, and final electronic states. Initial states are energetic levels below E_F , and therefore occupied, while intermediate and final states are located above E_F and E_{vac} , respectively, and therefore are unoccupied in the ground state.² UPS, using ultraviolet light sources for

¹ $h = \text{Planck's constant}$, $\nu = \text{frequency of the light}$

²The term “electronic state”, as it is used in PES should not be confused with the term “electronic state” as it is commonly used in chemistry, when describing the overall wave

3. *Experimental Methods and Setup*

the ionization, focuses on the investigation of occupied initial states as valence bands and OMOs, but is not able to access unoccupied intermediate states. The use of inverse photoelectron spectroscopy can overcome this lack, but it is restricted in terms of its energy resolution. A very powerful and complementary tool, is the 2PPE, which gives access to both, initial and intermediate states [63–68]. 2PPE is a second order non-linear optical process where two photons interact with a substrate to emit one electron. A typical 2PPE spectrum is sketched in figure 3.2. One photon excites an electron from below E_F into a real or virtual excited state and the second photon then pushes the electron above the vacuum level, where it can be detached and measured by e.g. a time of flight spectrometer. The obtained spectra can be regarded as a combination of an exponential secondary electron background [195] and overlaying peaks, which result from increased cross sections as the consequence of a high density of initial, intermediate or final states at a specific energy. Although the kinetic energy of the electrons is measured, the obtained spectra commonly are shown with respect to the final state energy $E_{Final} - E_F$. This plotting has the advantage that both, intermediate, and initial states can intuitively be calculated from the plotted energy axis, by subtracting the photon energy once for intermediate states and twice for initial states. A further advantage is, that the work function can be read directly from the position of the low energy cutoff of the spectrum, denoted as the secondary edge (SE). Here the emitted electrons have barely enough energy to overcome the work function, and so their residual kinetic energy is nearly zero. The high energy cutoff of the spectrum is assigned to the Fermi edge (FE) showing the electrons initially located at E_F and so having the maximum kinetic energy after emission. To run the second order non-linear process efficiently, high photon densities are needed, which can be obtained by ultrashort laser pulses, resulting in one of the major drawbacks of this method, as high photon densities and resulting emission processes can result in photodegradation of organic molecules [196–200]. While measuring 2PPE it is favorable to not observe direct photoemission simultaneously, due to the much higher efficiency, and so it is purposeful if the energy of one photon is not high enough to exceed the work function. The 2PPE process can be triggered by two photons of the same energy as well as by two photons of different energies. The first case is referred to as monochromatic 2PPE (or 1C-2PPE), while the latter is referred to as dichromatic 2PPE (or 2C-2PPE).

function for **all** electrons in a specific molecule. E.g. for a molecule being in the “electronic ground state” an emission can occur from an electron initially located in the HOMO or a lower lying occupied molecular orbital (OMO), and therefore from different “initial electronic states”.

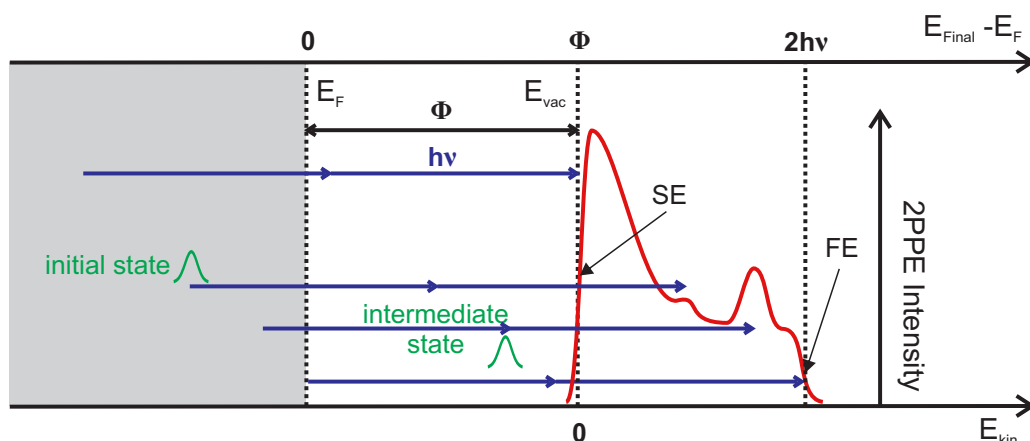


Figure 3.2.: Sketch of a typical 2PPE spectrum. Two photons ($E = h\nu$) interact with an electron located below E_{Fermi} pushing it above the vacuum energy, where its kinetic energy can be detected. It is common sense to reference the spectrum to the final state energy ($E_{Final} - E_F$) (see text). SE denotes the secondary edge and FE the Fermi edge.

However, as 2PPE spectra contain contributions from occupied as well as unoccupied states a proper assignment is necessary. Figure 3.3 shows how the kinetic energy of an electron, and thus the peak position in the 2PPE spectrum, changes for a variation of the incident photon energy. Slope evaluations of the observed peak positions for photon energy dependent measurements can so clarify whether a peak results from an initial, intermediate or final state. For monochromatic measurements a slope of zero indicates a final, a slope of one an intermediate, and a slope of two an initial state. For dichromatic measurements ($h\nu_1 = \frac{1}{2}h\nu_2$) slopes of zero for final states, of one and two for intermediate states, and three for initial states are obtained. For the intermediate states the slope depends on whether $h\nu_1$ or $h\nu_2$ serves as the pump or probe, respectively. It is important to note that these slope evaluations are only valid as long as the involved electronic states do not show a dispersion along the normal component of the wave vector (k_\perp), and therefore perpendicular to the surface [201, 202].

Giving the two photons a temporal offset time-resolved 2PPE (TR-2PPE) measurements can be carried out giving excess to excited state dynamics on the timescale of the femtosecond laser pulses. The probe pulse ionizing the intermediate state arrives the sample delayed, by increasing the length of its beam path, and, as the resulting 2PPE intensity is directly linked to the tran-

3. Experimental Methods and Setup

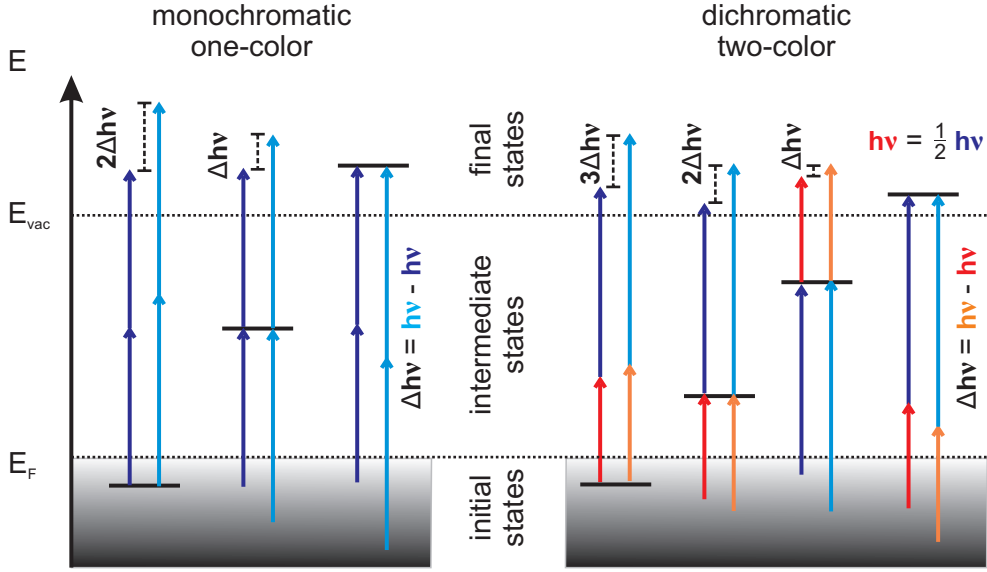


Figure 3.3.: Sketch of the 2PPE peak assignment. The kinetic energy of emitted electrons change differently for varying photon energies, depending on whether the observed peaks result from initial, intermediate, or final states.

sient population of this state, lifetimes can be measured. Mathematically this delay dependent intensity, also referred to the *cross-correlation* $XC(t)$, can be described by a convolution of the *auto-correlation* function $AC(t)$ and the transient population $N(t)$. The auto-correlation itself is a convolution of the two laser pulses ($I_1(t)$, $I_2(t)$), which can be satisfyingly described by a sech^2 function [203]. A detailed mathematical derivation can be found in [204]

$$\begin{aligned}
 XC(t) &= (AC * N)(t) = (I_1 * I_2 * N)(t) \\
 &= \int_{-\infty}^{\infty} \int_{-\infty}^{\infty} I_1(x) * N(y - x) * I_2(t - y) dx dy \quad (3.2.2)
 \end{aligned}$$

To obtain additional information about the dispersions of the investigated states, and thus the degree of electron delocalization, angle resolved UPS as well as AR-2PPE can be performed by changing the emission angle of the sample in front of the analyzer. For periodic surfaces the wave function inside and outside of the surface have to phase-match, and therefore the parallel component of the k -vector is conserved [124, p. 387]. In dependence of the angle Θ between surface normal and detector axis, electrons with a different parallel

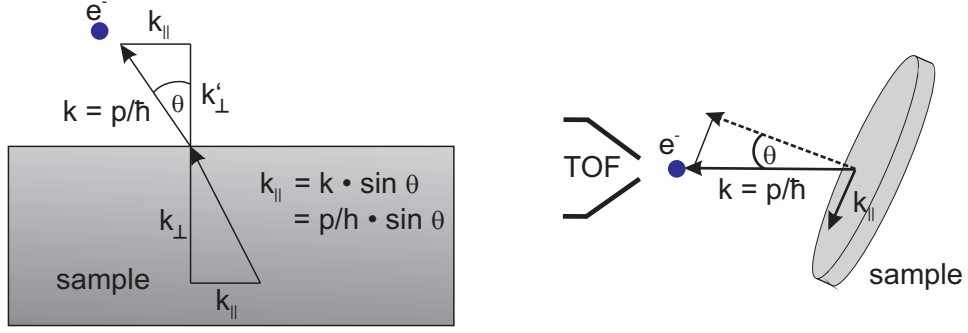


Figure 3.4.: AR-PES conditions. $k_{||}$ is conserved, while k_{\perp} changes due to the samples work function. Electrons with a different parallel momentum are detected by rotating the sample in front of the TOF. Figure adopted from [205].

momentum are detected (see figure 3.4). This initial parallel momentum can be calculated as a function of Θ and the kinetic energy of the electrons E_{kin} .

$$k_{||} = \frac{p}{\hbar} \sin\Theta = \frac{\sqrt{2m_e E_{kin}}}{\hbar} \sin\Theta \quad (3.2.3)$$

As discussed in section 2.1.1 nearly free electrons can be described by a parabolic like dispersion with an effective mass m^* . Under this assumption the energy of an electron in a specific state can be written as

$$E_{Bind} = E_{(k_{||}=0)} + \frac{\hbar^2 k_{||}^2}{2m^*}. \quad (3.2.4)$$

By plotting the electron's energy against $k_{||}$, its effective mass, as a parameter for its ability to move parallel to the surface, thus can be calculated from the parabolic curvature. For a more detailed insight into PES and 2PPE see Refs. [134, 202, 206, 207], [124, p. 386].

3.3. Experimental Setup and Sample Preparation

To apply UPS, 2PPE and TPD an advanced experimental setup is needed, which can be divided into two main parts. On the one hand a laser setup

3. Experimental Methods and Setup

delivering ultrashort monochromatic light pulses to efficiently trigger the 2PPE process and on the other hand a UHV chamber, where TPD measurements and sample preparations can be carried out, as well as the photoemitted electrons can be detected. Since no fundamental changes were made to the setup during the last years, only a short introduction is given here. A more fundamental description can be found in Refs. [204, 208, 209]

3.3.1. UHV Chamber

A sketch of the UHV chamber is shown in Figure 3.5. The ultra-high vacuum is created by a series of turbomolecular pumps providing a base pressure of $1 \cdot 10^{-10}$ mbar. A manipulator allows a 3-dimensional movement of the sample and a rotation around its own axis. The temperature of the sample can be controlled over a range of 80 K to 900 K by cooling with liquid nitrogen and heating via tantalum wires, which additionally serve to connect the sample to the manipulator. In the lower part of the chamber a cylindrical μ -metal shield is installed to ensure appropriate detection of photoemitted electrons with a time-of-flight spectrometer (TOF) (210 mm drift tube, 6° acceptance angle). Moving the sample in 2-dimensions in front of the TOF allows the investigation of different spots of the sample, while a rotation around its axis gives access to AR-2PPE measurements. The laser beams enter the chamber through a MgF₂ window, hitting the sample in 45° to the TOF axis in normal emission mode. For further surface analysis a low energy electron diffraction (LEED) (*Fision instruments rear view LEED - RVL 900*) is additionally installed inside the μ -metal shielding. The upper level of the chamber includes an in-situ screw driver, a sputter gun (*Specs IQE 11-A*), a quadrupole mass spectrometer (QMS, *Balzers QMG 112A*), a Knudsen cell evaporation unit (*Kentax TCE-BSC*), and a sample storage. This setup allows an in-situ preparation of well-defined surfaces. The Au(111) crystal used as the substrate in the framework of this thesis is prepared by a three step cleaning cycle. First the sample gets cleaned by heating to 800K and subsequent sputtering for 5 min with an argon background pressure of $2\text{-}3 \cdot 10^{-6}$ mbar and an ion acceleration voltage of 1.5 kV. The crystal is oriented in a 45° angle to the argon beam during this procedure. The resulting rough surface then is thermally annealed for 30 min at 800 K. This allows the clean gold surface to realign into the reconstructed well-defined Au(111) herringbone reconstructed surface. In the following different organic molecules, can be evaporated onto the sample to obtain the desired interfaces. Coverages were controlled by varying Knudsen cell temperatures and dosing times. A successful preparation is controlled via TPD (see above), using the QMS to detect molecular fragments. A detection of fragments is necessary

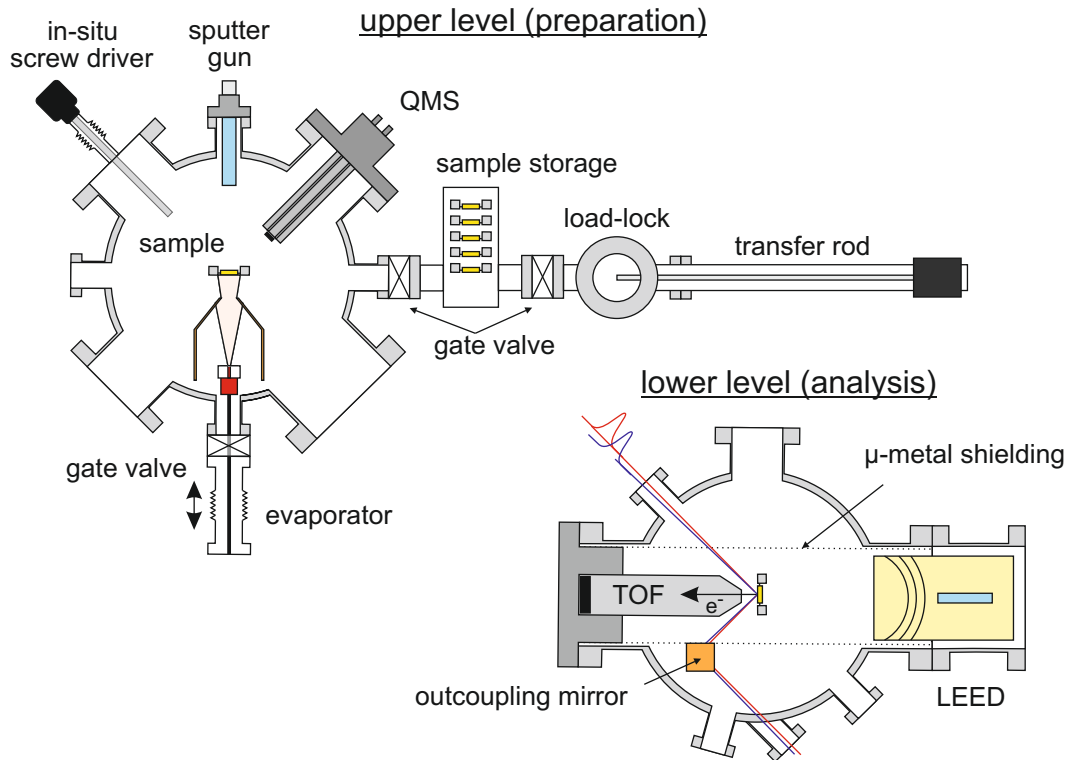


Figure 3.5.: Sketch of the UHV chamber used in the framework of this thesis. Sample preparations and TPD measurements are conducted in the upper level, while PES measurements are carried out at the lower level of the chamber. Figure reproduced from Ref. [208].

for two reasons. On the one hand, the used *Balzers QMG 112A* QMS is restricted to a mass-charge ratio between $m/z = 2 - 200$. On the other hand the detection of different mass fragments gains information about possible on surface reactions and incomplete desorptions.

3.3.2. Laser Setup

To obtain the needed ultrashort monochromatic light pulses a complex laser setup is used as sketched in figure 3.6. A commercial solid state neodymium-doped yttrium orthovanadate (Nd:YVO₄) laser (532 nm, frequency doubled, *Verdi V18 - Coherent*), is used to pump a Ti:Sapphire oscillator (*Mira 900B*) and a regenerative amplifier (*RegA 9050 - Coherent*). In the Ti:Sapphire oscillator ultrashort light pulses with a wavelength of $\lambda = 800$ nm, and a repetition

temporal overlap of the two beams on the sample has to be ensured. For the latter, so called *delay stages*, varying the length of the beam path, are introduced into the VIS- and the 3.1 eV-beam. This additionally allows to measure TR-2PPE.

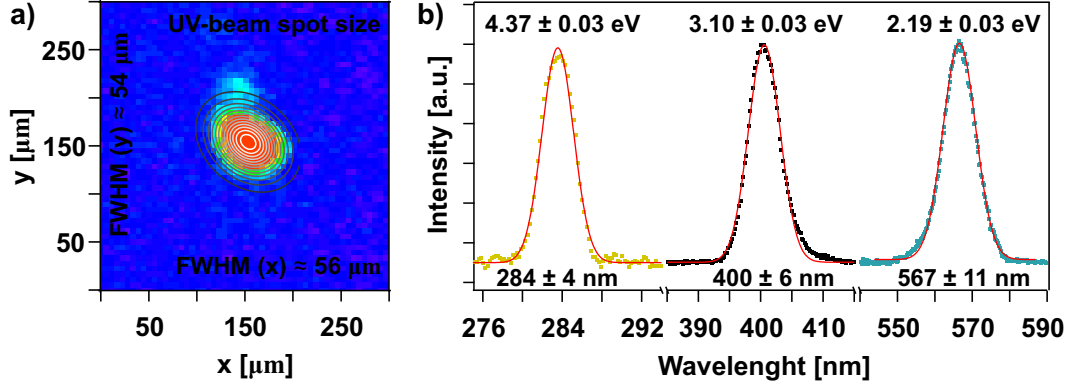


Figure 3.7.: Illustration of the beam characteristics. (a) Spatial distribution of the UV-beam taken with a CCD-Camera (*Astro CCD Camera - Sony ICX098BL Chip*). The data is fitted with a 2D Gaussian-shaped peak. (b) Exemplary spectra of the UV-, VIS-, and 3.1 eV-beam. The spectral resolution is obtained from the FWHM of the Gaussian-shaped peaks.

As a consequence of the setup dichromatic measurements with the UV-beam and the VIS-beam are always restricted to $h\nu_1 = \frac{1}{2}h\nu_2$. The light pulses finally interacting with the sample have a power of 0.5 – 2 mW for the UV-beam and 4 – 7 mW for the VIS-beam and the 3.1 eV-beam) adjusted in dependence of the individual cross section of the investigated samples and possible photodestruction for too high intensities. The beam diameter is about 55 μm (2D-gaussian fit) resulting in a spot sizes of approximately 2400 μm² (see figure 3.7 (a)). Exemplary spectra of the different beams are given in figure 3.7 (b) showing the spectral resolution of 0.03 – 0.04 eV as the FWHM of the fitted Gaussian-shaped peaks. The final time resolution of the setup is determined by the auto-correlation (AC) of the two pulses on the sample ranging from 75 to 100 fs, depending on the daily alignment of the setup. The AC directly on the sample can be obtained by measuring the cross-correlation (XC) (see equation 3.2.2) for non-resonant excited initial states as in these cases the intermediate virtual states have a vanishing transient population. As described above the XC of non-virtual intermediate states can be described as a convolution of the AC and the transient population $N(t)$ of these states. This then enables the setup to determine excited state dynamics down to

3. *Experimental Methods and Setup*

approximately 50 *fs*.

4. Characterization of the bare Au(111) Surface

In the framework of this thesis the metal substrate of choice for the investigation of the metal/organic interface was the Au(111) surface, showing low reactivities and high stability. A theoretical description of the electronic structure of the gold bulk and at the Au(111) surface was carried out in section 2.1.1. In this chapter the focus is on the experimental description of the gold sample used in our setup to rule out misassignment and misinterpretation of the experimental results obtained for the investigated interfaces.

Figure 4.1 shows 2PPE, UPS and LEED measurements on the well-prepared bare Au(111) crystal surface, cleaned by the procedure described in section 3.3.1. Monochromatic 2PPE measurements for several photon energies show a strong and narrow feature shifting with a slope of two in respect to the used photon energy as it is expected for an initial state. Resulting in a binding energy of $0.45 \pm 0.04 eV$ below E_F , this feature can be clearly assigned to the sp-derived SS as it is observed on high-quality Au(111) crystal surfaces. For high photon energies an additionally weaker feature is observed for lower energies. This feature is arising from the sp-band and as the sp-band shows a dispersion perpendicular to the surface no slope evaluation can be carried out as can be seen from the photon energy dependent peak positions shown in figure 4.1 (c). The same is valid for the d-band and its several features obtained in the low energy regions of the spectra. The work function, directly obtained from the secondary edge of the spectra, is $5.47 \pm 0.05 eV$ being a further clear hind for a well-defined and clean Au(111) surface. Unfortunately the IPSs at the clean Au(111) sample cannot be seen in the presented data, because of the high work function of the gold. If the work function gets reduced by adsorbing molecules they shift downwards in energy and so can be obtained additional in our spectra. For the dichromatic measurements also features assignable to the SS and the sp-band are observed and the SS state shows the expected photon energy dependent shift with a slope of three in respect to the photon energy of the VIS-beam. As the work function of the used gold surface is rather high only initial states located near to the Fermi edge can be observed

4. Characterization of the bare Au(111) Surface

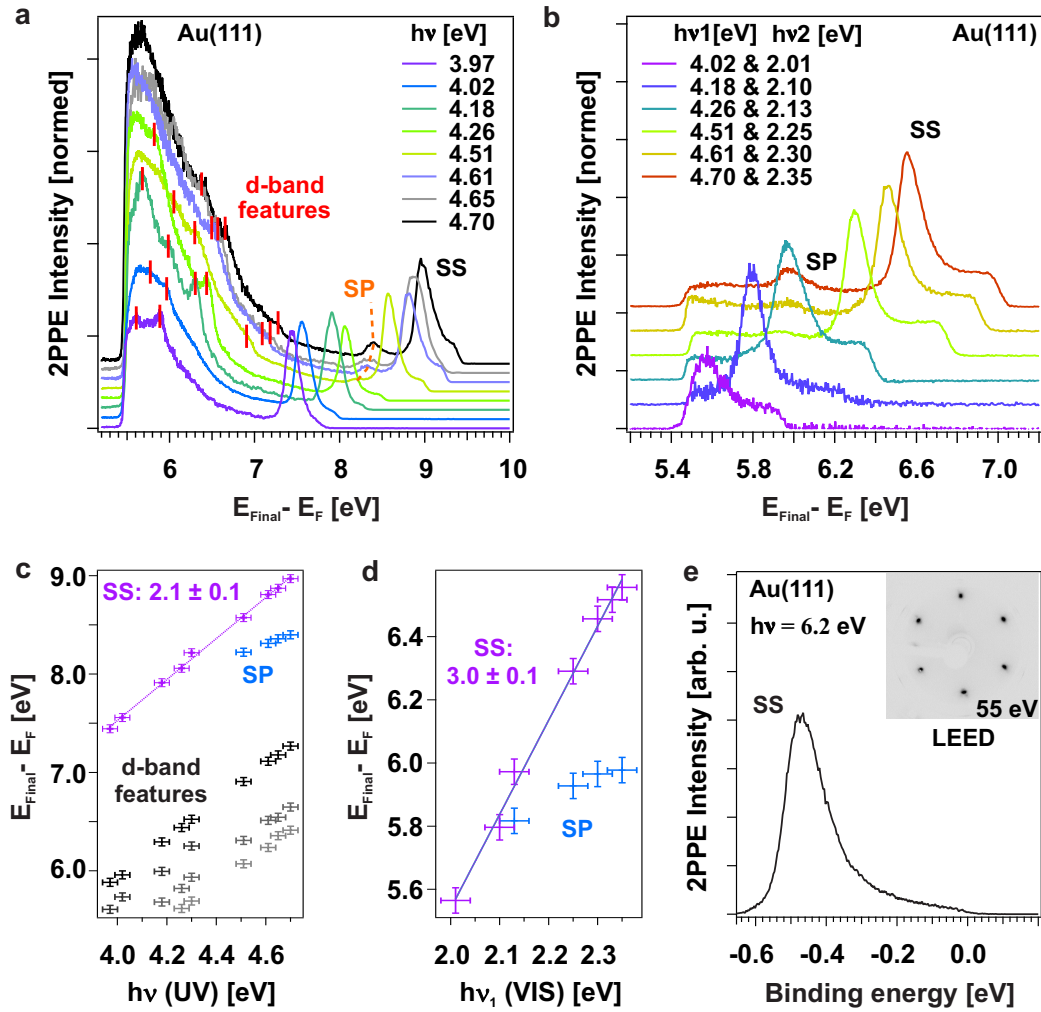


Figure 4.1.: PES on the bare gold surface. (a) monochromatic and (b) dichromatic 2PPE spectra. In both cases the Shockley surface state (SS) and a sp-band feature are visible. Additionally, several d-band features are observed in (a). (c) and (d) show the photon energy dependent peak positions. A slope evaluation was only carried out for the SS, as the sp- and the d-bands show a dispersion perpendicular to the surface. (e) UPS spectrum taken with $h\nu = 6.2$ eV is mainly dominated by the SS. As an inset in the upper right a LEED pattern of the surface is given, with an inverted color scale.

by UPS measurements with a photon energy of $h\nu = 6.2$ eV. The obtained spectrum shown in figure 4.1 (e), thus is dominated by only one peak, which again is assigned to the SS. The LEED pattern shown in the inset was taken

with a primary electron energy of 55 eV and shows the typical pattern of the reconstructed Au(111) surface [210], once more underpinning the presence of a well aligned and contamination-free crystal surface. To confirm the assignment of the SS and the sp-band features in the spectra shown in figure 4.1 TR-2PPE measurements were carried out along the ΓM -line of the first Brillouin zone, as both should show a significant dispersion parallel to the surface. The results are shown in figure 4.2.

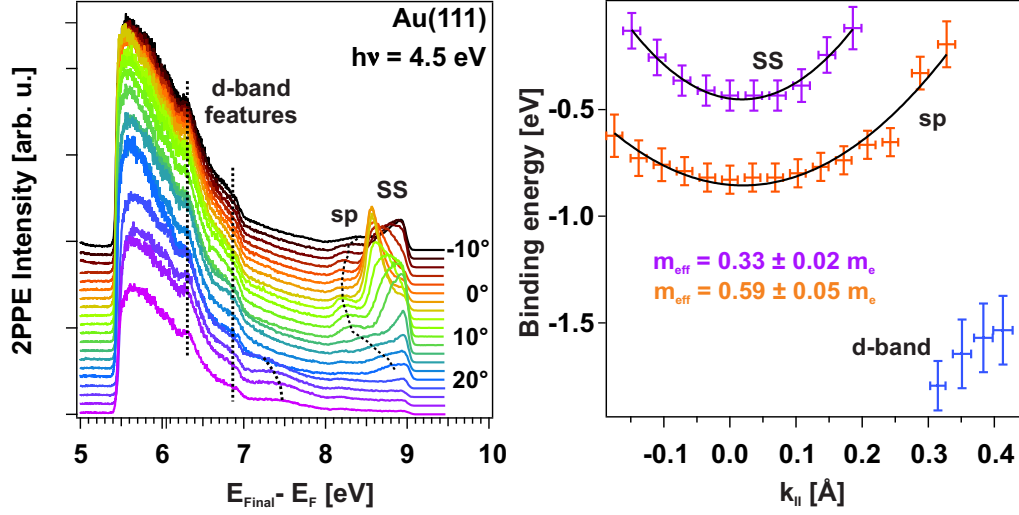


Figure 4.2.: AR-2PPE on the bare gold surface. Left: Spectra obtained for different angles of the sample in front of the TOF. A clear dispersion of the sp-band and the SS are observed. Further an electron like dispersion of a d-band feature is observed for angles above 20°. Right: The binding energy of the three dispersing features is given in respect to k_{\parallel} . For the sp-band and the SS the effective mass (m_{eff}) is calculated from the curvature of the peak position.

Turning the sample in front of the analyzer leads to an angle dependent peak shift for the peaks assigned to the SS and sp-band, respectively, as can be seen on the left. The peak position in respect to the wave vector parallel to the surface (k_{\parallel}) is plotted on the right and based on equation 3.2.4 the effective mass of the electrons located in these states can be calculated resulting in an effective mass of $0.33 \pm 0.02 m_e$ for the SS and $0.59 \pm 0.05 m_e$ for the sp-band. For high angles it can be seen, that a further peak appears in the region of the d-band features which, thus is assigned to a d-band feature showing an electron like dispersion. In foresight to the discussion of band formation at the interface carried out in chapter 7, it should be highlighted here, that non of the in normal emission observed d-band features shows any kind of dispersion

4. *Characterization of the bare Au(111) Surface*

parallel to the surface.

5. Singlet Fission at the TIPS-Pentacene/Au(111) Interface

In 1961 it was predicted by Shockley and Queisser [169] that the efficiency of a single junction solar cell is theoretically limited to 32 %. This limit is mainly determined by waste heat, as the surplus photon energy of a photon exceeding the absorber band gap is lost. Singlet fission (see section 2.2) is a promising process to overcome this so called Shockley-Queisser limit by creating two charge carriers by the absorption of one photon [170, 171]. The most prominent candidates to undergo this process are the acenes and within these, pentacene stands out showing the most efficient singlet fission on ultra-short lifetimes [77–84]. In the following chapter a good soluble pentacene derivative, the 10,17-bis((triisopropylsilyl)ethynyl)-pentacene (TIPS-Pn), was investigated and the singlet fission process within this compound at the metal interface is considered closer. Partial results of this chapter have already been published in Ref. [64].

5.1. TIPS-Pentacene: A Soluble Pentacene Derivative

Pentacene is a well-known organic semiconductor having a large conjugated π -system and an optical band gap of 1.83 eV absorbing within the visible region, which has already shown its high potential for device applications [70–72]. The lowest singlet exciton (S_1) transition energy lies slightly above two times the triplet energy (T_1) of 0.86 eV [82]. Since ($E(S_1) \geq 2 \cdot E(T_1)$) is necessary for efficient and fast singlet fission, pentacene seems to be an ideal candidate. Nevertheless, pentacene has some drawbacks, as it is very sensitive to oxidation and shows a low solubility [73]. To overcome these drawbacks, Anthony et al. [74] synthesized a functionalized pentacene derivative, the TIPS-Pn as

5. Singlet Fission at the TIPS-Pentacene/Au(111) Interface

it is shown in figure 5.1 . By adding TIPS-groups in the central position of the pentacene backbone, a strongly increased solubility and stability is obtained, simplifying purification and solution-based processing. An additional side effect is a favorable self-assembly into a π -stacked array increasing overlap of the pentacene rings with adjacent molecules and a reducing interplanar spacing of the aromatic rings [74]. TIPS-Pn was the object of numerous studies during the last years, because of its promising properties for organic electronic devices [64, 74, 90, 177, 179, 181, 211–221]. It has shown to undergo SF in solution and thin films on ultrashort timescales, as it is the case for its unsubstituted derivative [64, 90, 177, 181, 213–215]. As singlet fission dynamics of TIPS-Pn, so far, were mainly investigated in solution or in spin coated films, a focus on evaporated samples, as being the topic of this work, gives access to thin films down to the monolayer regime. This reveals information about the influence of the underlying surface as a model system for (metal) electrodes. The adsorption geometry influences the electronic structure of the adsorbate-substrate system and is thus also of great interest. For example, Mannsfeld et al. [212] showed via grazing incidence X-ray diffraction (GIXD) experiments that for “non-interacting” surfaces (e.g. SiO₂) the molecular plane of TIPS-Pn is oriented nearly perpendicular to the surface with the TIPS-groups pointing towards the surface. This allows the molecules to grow in a molecular packing that is nearly identically to that in the bulk crystal. In opposite, at Au(111) surfaces a more or less planar (tiling angle $\leq 30^\circ$) geometry is observed by HREELS [64] and near edge X-ray absorption fine structure (NEXAFS) [219] measurements.

5.2. Sample Preparation and Coverage Estimation of TIPS-Pentacene on Au(111)

The Au(111) surface was prepared by the standard cleaning cycles, as described in section 3.3.1. Subsequently, TIPS-Pn was evaporated onto the surface by heating the effusion cell to 470 K for a certain time depending on which coverage was planned to be investigated. The sample was held at 200 K during the evaporation process to ensure sufficient sticking of the molecules. Figure 5.1 shows EI-MS Spectra of TIPS-Pn, as bought and after heating in the effusion cell.¹ As the Spectra are identical it can be concluded, that no decomposition

¹ EI-MS measurements were carried out by the Mass Spectrometry Facility of the Institut of Organic Chemistry of the University of Heidelberg under the lead of Juergen Gross

5.2. Sample Preparation of TIPS-Pentacene

took place during the evaporation process. The inset shows the area measurable by the QMS attached to the UHV chamber enlarged with intense masses labeled. An assignment of these fragments is given in the lower part of the graph. The high intense fragments $m/z = 43, 59, 73, 87, 115$ result from the TIPS side groups, while the group of $m/z = 190-200$ can be assigned to fragments of the pentacene backbone.

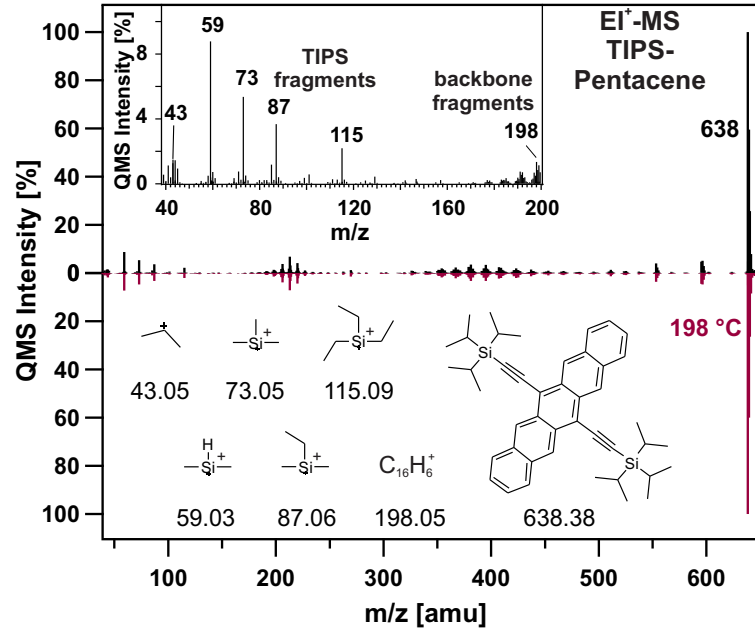


Figure 5.1.: EI-MS spectrum of TIPS-Pn, as bought (upper part) and after heating inside the doser (lower part). The part of the spectrum observable by the QMS attached to the UHV chamber is shown enlarged in the inset. Important fragments are labeled.

To determine the coverage of TIPS-Pn adsorbed on the Au(111) surface TPD measurements were carried out. Figure 5.2 shows spectra recorded for $m/z = 59$ for different coverages between 1-12 monolayers (MLs). A high-temperature peak, labeled as α_3 , is located around 570 K, showing the shape of a typical first-order desorption as it is the common case for molecules adsorbed in a monolayer with little lateral interactions as it is expected for TIPS-Pn, due to its bulky side chains. For lower desorption temperatures an additional peak with two maxima, α_1 and α_2 , is observed for higher coverages. Showing a typical zero-order desorption shape they are assigned to the multilayer and second layer desorption, respectively. This kind of double peak feature can occur, when the second layer is still bound slightly stronger to the surface than molecules in even higher layers, due to interactions with the substrate.

5. Singlet Fission at the TIPS-Pentacene/Au(111) Interface

The initial coverage was determined by the peak integral ratios of the combined multilayer peak and the monolayer peak. TPD spectra of different mass charge ratios $m/z = 59, 73, 198$ for a coverage of 12 ML are shown in the inset in figure 5.2. The shape of all three, including side chain ($m/z = 59, 73$) and backbone ($m/z = 198$) fragments, are the same for the multilayer desorption, thus an intact multilayer desorption can be assumed. This enables the preparation of well-defined monolayers by evaporating a multilayer coverage to the surface and subsequently heating to around 440 K. The intact multilayer desorption further tells us, that an intact evaporation and adsorption onto the surface was achieved in the first place. The monolayer desorption peak is only present for the TIPS-side chain while the backbone signal increases undefined over a large temperature scale. This is clear hind for a molecule decomposition of the adsorbed molecules during heating above 550 K and thus no intact desorption of the monolayer takes place, which is in good agreement with temperature-dependent XPS measurements carried out by Gnoli *et al.* [219].

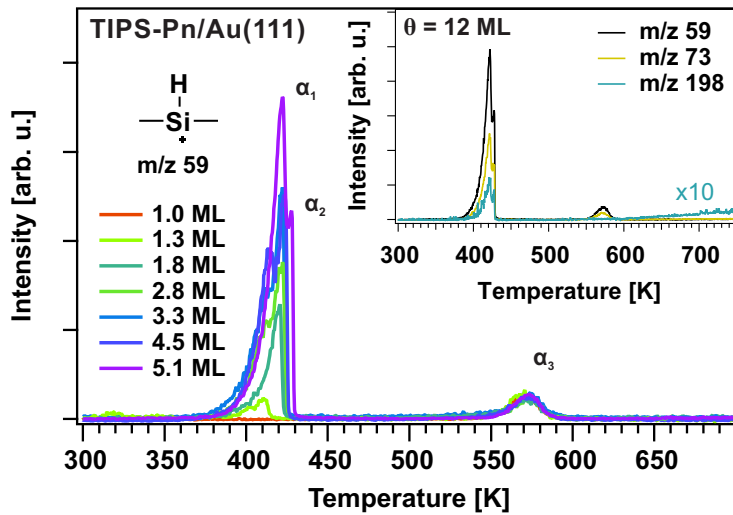


Figure 5.2.: TPD measurements (ionic fragment $m/z = 59$) of TIPS-Pn adsorbed on Au(111) for different initial coverages recorded with a heating rate of 1 K/s. α_3 denotes the monolayer desorption peak while α_1 and α_2 denote the multilayer and second layer desorption peak, respectively. The inset shows equivalent measurements for a 12 ML coverage for different mass charge ratios.

5.3. Electronic Structure and Excited State Dynamics

To reveal the electronic structure of the interface UPS and 2PPE were carried out and the results will be discussed in the following. Figure 5.3 shows a selection of monochromatic (a) and dichromatic (b) 2PPE spectra taken with different photon energies and for varying coverages. A full series of photon energy and coverage dependent measurements can be found in the appendix (figure A.1 and A.2). For the monochromatic spectra the low energy region is dominated by the background and the d-band features (shown gray underlaid). Within the 1 ML spectra in total five additional peaks are observed in the high energy regions. An assignment can be carried out by the photon energy dependent shift of the peak positions as shown in figure 5.3 (c).² The evaluation gives four intermediate states and one initial states with their energies being $E_{HOMO} = -0.9 \pm 0.1$ eV, $E_{UMO_2} = 2.42 \pm 0.04$ eV, $E_{UMO_3} = 3.65 \pm 0.06$ eV, $E_{IPS_{n=1}} = 3.98 \pm 0.04$ eV, and $E_{IPS_{n=2}} = 4.42 \pm 0.08$ eV in respect to E_{Fermi} . The observed initial state was assigned to the HOMO as being the energetically highest molecule induced state observed. This assignment is underpinned by UPS measurements shown in appendix A.1 (d) and coverage dependent 2PPE measurements in appendix A.2 where the occurrence and increase of the HOMO attributed peak with increasing coverage can be clearly seen. The energetically lowest intermediate state (UMO_2) is only observed for low photon energies as it gets overwhelmed by d-band features for higher photon energies. The assignment of UMO_2 and UMO_3 to molecular orbitals is valid as there are no intermediate states of the bare Au(111) surface expected in this energetic region. In the opposite the two highest intermediate states can only be observed for high photon energy measurements, as a single photon needs to have sufficient energy to populate these states. Calculating their energetic position in respect to E_{vac} gives $E_{IPS_{n=1,vac}} = -0.67 \pm 0.04$ eV, and $E_{IPS_{n=2,vac}} = -0.23 \pm 0.08$ eV, which suggests that these are the first and second IPS with a quantum defect of approximately $a = 0-0.1$ calculated *via* equation 2.1.8. This suggestion is approved by AR-2PPE measurements as displayed in appendix A.3 showing a dispersion of these states. The observed effective masses are $m_{eff}(IPS_{n=1}) = 1.17 \pm 0.29$ m_e and $m_{eff}(IPS_{n=2}) = 1.3 \pm 0.35$ m_e . The obtained energetic positions and dispersions of the IPSs are in good agreement with various adsorbate covered Au(111) surfaces [66, 222–224].

With increasing coverage the HOMO dominates the high energy region of

²For details regarding the slope evaluation refer to section 3.2

5. Singlet Fission at the TIPS-Pentacene/Au(111) Interface

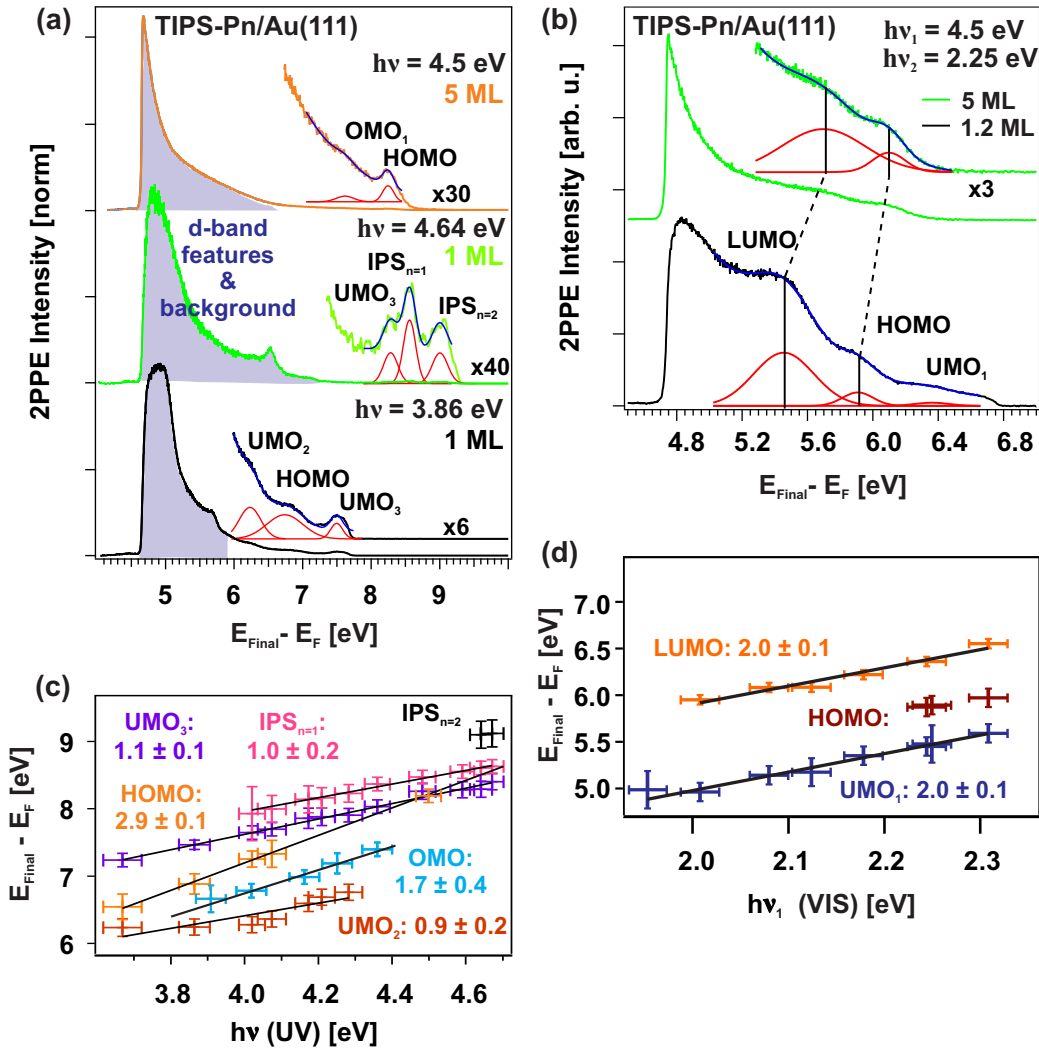


Figure 5.3.: (a) Monochromatic and (b) dichromatic 2PPE spectra of TIPS-Pn adsorbed on Au(111) recorded with different photon energies and coverages. 2PPE intensity is given as a function of the final state energy. The spectra were fitted by an exponential background and Gaussian-shaped peaks. Peaks resulting from (the highest) occupied molecular orbitals ((H)OMO), (the lowest) unoccupied molecular orbitals ((L)UMO), and image potential states (IPS) are observed. (c) and (d) show the corresponding photon energy dependent peak positions to assign peaks observed in the 2PPE spectrum. Figure adapted from [64].

5.3. Electronic Structure and Excited State Dynamics

the spectrum and a further initial state is observed, which is assigned to a lower lying OMO with $E_{OMO_1} = -1.24 \pm 0.15 \text{ eV}$. The dichromatic spectra taken at a coverage of 1.2 ML show three peaks, and the slope evaluation reveals two intermediate states besides the HOMO, which was already identified by UPS and monochromatic 2PPE. Calculating the energetic values, gives $E_{UMO_1} = 1.9 \pm 0.07 \text{ eV}$ and $E_{LUMO} = 0.9 \pm 0.04 \text{ eV}$, in respect to E_F and thus these peaks are assigned to the LUMO and a higher lying unoccupied molecular orbital (UMO). By increasing the coverage the spectra get dominated by the peaks assigned to the HOMO and the LUMO. The increase of the LUMO's peak intensity with increasing coverage is a clear sign that we observed the optical LUMO (S_1). Besides the increasing intensity also a shift in the energetic position of the peaks is observed with increasing coverage (also refer to appendix A.2). For a coverage up to 12 ML the LUMO shows an upwards shift of 250 meV, while the HOMO shows an upwards shift of 180 meV, leading to $E_{HOMO,12 \text{ ML}} = -0.72 \pm 0.1 \text{ eV}$ and $E_{LUMO,12 \text{ ML}} = 1.15 \pm 0.1 \text{ eV}$. The upwards shift of the LUMO is caused by a reduction of the electronic coupling between the surface and the adsorbing molecules [67, 68]. For the HOMO, this reduction should lead to an increase of binding energy and thus to a downwards shift. However, the opposite behavior may occur, due to intermolecular interactions. Besides the peaks assigned to electronic states at the interface, a work function shift of about 800 meV and a shift of the SS of about 130 meV (UPS measurements, appendix A.1) can be found for the adsorbate covered surface. This adsorbate-induced decrease of the work function attributed to the push-back effect (see section 2.1.3). The shift of the surface state is a well-known phenomena on adsorbate covered noble metal surfaces, as it has been reported for noble gases [126, 132, 133], or molecular layers [128–131] and is caused by either interfacial charge transfer processes or modifications of the surface work function [225].

The overall electronic structure of the TIPS-Pn/Au(111) interface is given in figure 5.4. In total three occupied and six unoccupied states are observed. Besides the interface related SS and IPSs, the HOMO, the optical LUMO and further higher and lower lying MOs of TIPS-Pn at the interface are assigned. $E_{HOMO} = -0.9 \text{ eV}$ can be approved by literature [211, 216]. With the additional information about the LUMO located at $E_{LUMO} = 0.9 \text{ eV}$, the optical gap is 1.80 eV for the monolayer and as the energetic positions of HOMO and LUMO shift with increasing coverage, the gap rises to 1.87 eV. This is in good agreement with electronic HREELS measurements of the investigated interface, where the optical gap was determined to be 1.9 eV [64]. This again underpinned the conclusion, that the observed LUMO is an intramolecular optically excited S_1 state.

5. Singlet Fission at the TIPS-Pentacene/Au(111) Interface

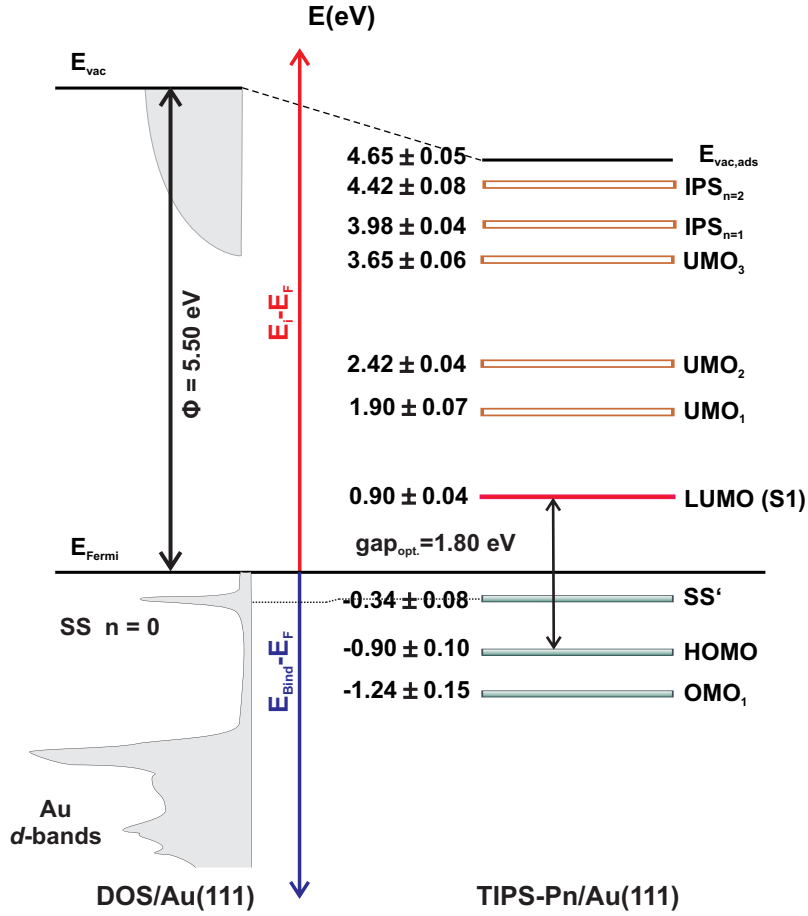


Figure 5.4.: Energy level diagram of one monolayer TIPS-Pn adsorbed on Au(111). On the left the density of states (DOS) of the bare gold surface is shown. Unoccupied electronic states are shown in red, while occupied electronic states are shown in blue. The molecule-induced surface state and work function shifts are highlighted by dashed lines. The energetic positions are given with respect to the Au(111) Fermi level (E_F).

To gain additional information about the excited state dynamics at the TIPS-Pn/Au(111) interface and possible singlet fission, TR-2PPE has been carried out. Figure 5.5 (a) shows an exemplary false color plot of a sample with a coverage of 5 ML of TIPS-Pn on the gold surface, taken with photon energies of $h\nu_1 = 2.25 \text{ eV}$ and $h\nu_2 = 4.5 \text{ eV}$, where $h\nu_1$ serves as the pump and $h\nu_2$ serves as the probe pulse for positive time delays. In the false color plot representation of the data, the normalized dichromatic 2PPE signal is

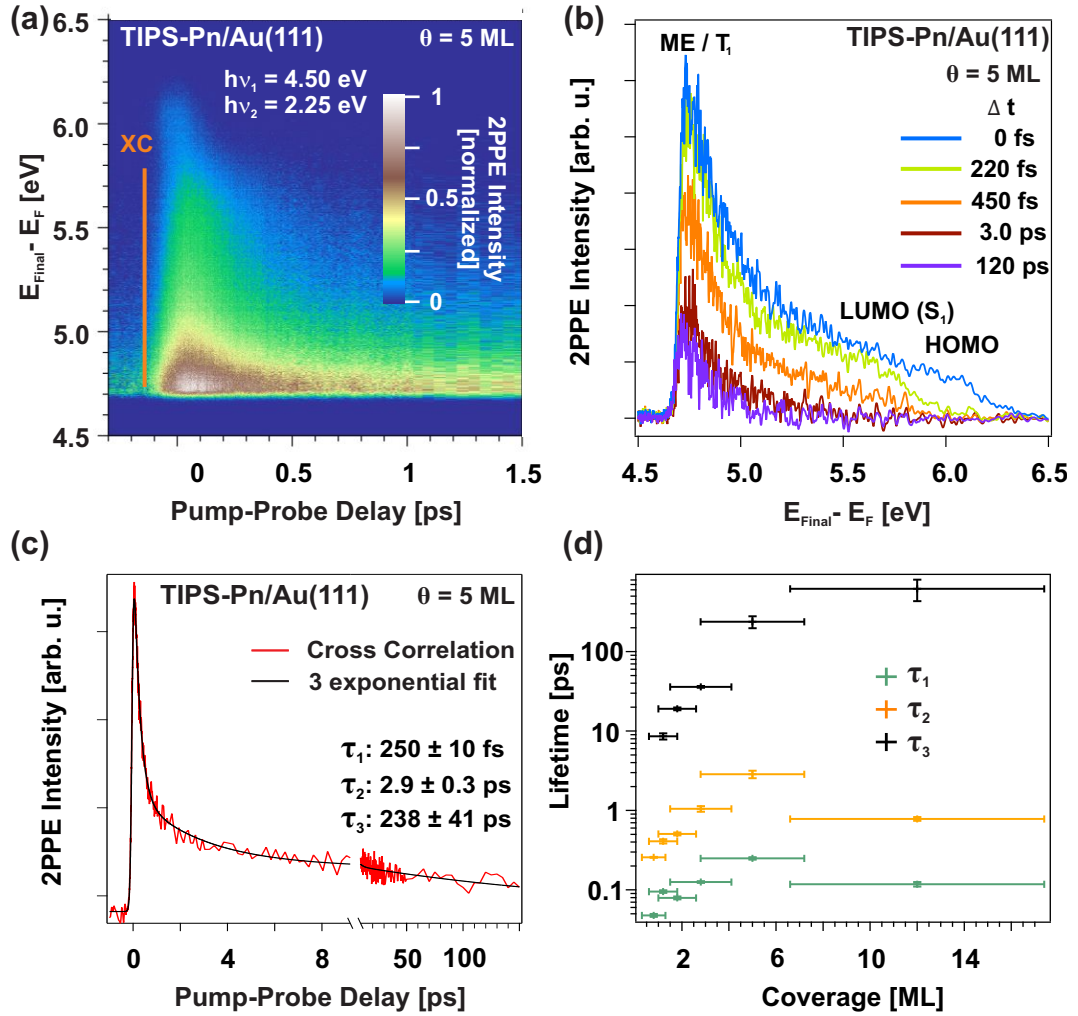


Figure 5.5.: (a) False color plot of the 2PPE intensity as a function of final state energy and pump-probe delay for a coverage of 5 *ML* TIPS-Pn adsorbed on Au(111). (b) 2PPE spectra at different pump-probe delay times. (c) XC curve obtained for the energy range displayed in (a). Three lifetimes result from a triple exponential decay convoluted with a *sech*² function. (d) Lifetimes, as determined in (c), as a function of TIPS-Pn layer thickness on the Au(111) surface. Figure adopted from [64].

given by a false color scale in respect to the final state energy and the pump-probe delay. From this representation it can be seen, that the intensity of the dichromatic 2PPE spectrum is not vanished for a temporal offset, but evolves differently depending on the final state energy of the measured elec-

5. Singlet Fission at the TIPS-Pentacene/Au(111) Interface

trons. A short living contribution can be seen in the high energy region of the spectrum, while the low energy part directly at the secondary edge shows a long living contribution. A more detailed insight can be gained by taking a look at specific spectra for selected time delays, as displayed in figure 5.5 (b). These spectra can be obtained by taking slides at specific time delays of the representation in (a). For $t = 0$, where pump and probe pulse overlap in time a 2PPE spectrum comparable to those in figure 5.3 is observed. Contributions of the HOMO, the optical LUMO (S_1) and a further contribution directly at the secondary edge can be seen. This assignment becomes more comprehensible, by considering the spectra with increased time delays. For a temporal offset of 220 fs the contribution from the HOMO at around 6.1 eV , being an initial state, is gone, as electrons from this state need both photons contemporaneous to be ionized via a virtual state. The LUMO (S_1) state, located around 5.6 eV in the spectrum, possesses a lifetime and thus electrons from this excited state can be ionized by a delayed photon from the probe pulse. The same is valid for the long-lasting contribution in the spectrum directly at the secondary edge of the spectrum. The S_1 state and a component at the secondary edge, decay within in the first picoseconds. The spectrum, however does not vanish completely at the secondary edge, but instead remains long lasting as can be seen by comparing the nearly identical spectra at 3 ps and 120 ps . Taking the cross-correlation (XC), as the integrated intensity of a selected part of the spectrum in respect to the pump-probe time delay, allows to determine the decay constants and thus the lifetimes of the decaying contributions. The selected part of the spectrum to create the XC is shown in figure 5.5 (a) and the resulting XC is given in (c). The curve can be fitted by a triple exponential decay, describing the transient population of the involved intermediate states, convoluted with a $sech^2$ function, representing the AC of the two laser pulses. For a TIPS-Pn coverage of 5 ML, lifetimes of $\tau_1 = 250 \pm 10 fs$, $\tau_2 = 2.9 \pm 0.3 ps$, and $\tau_3 = 240 \pm 40 ps$ are obtained. Figure 5.5 (d) shows the influence of the gold substrate on the excited state dynamics, by plotting the observed lifetimes against the coverage of TIPS-Pn on the gold substrate. All three lifetimes increase with increasing coverage. τ_1 increases slightly from $50 \pm 10 fs$ to $160 \pm 60 fs$ (average value 3-12 ML), while the effect is much stronger for τ_2 and τ_3 increasing from $0.26 \pm 0.04 ps$ to $1.6 \pm 0.9 ps$ (average value 3-12 ML) and $8.6 \pm 0.8 ps$ to $620 \pm 190 ps$. This coverage dependency is a result of two relaxation channels [55-57,67]. On the one hand the intrinsic channel in the bulk material and on the other hand a distance dependent external channel enabling a relaxation of the excited states into the gold.

Knowing that TIPS-Pn undergoes singlet fission allows an appropriate assign-

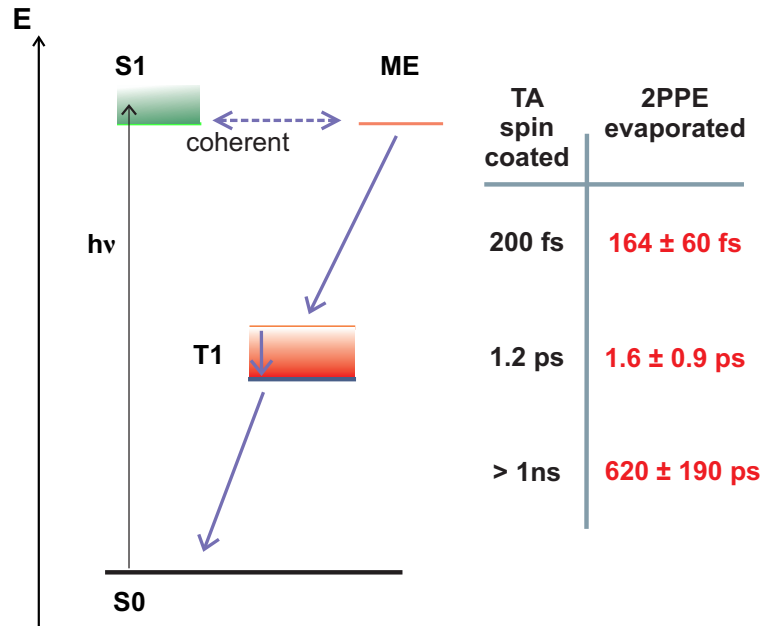


Figure 5.6.: Summarized model for the excited state dynamics of TIPS-Pn adsorbed on Au(111) obtained via 2PPE measurements. For comparison TA data from spin coated films is added [90]. Figure adopted from Ref. [64].

ment of the decay times [64, 90, 177, 181, 213–215]. A coherent excitation of the S_1 state and the ME state have been reported in recent studies [21–25], and thus the contribution at the secondary edge being excited and decaying contemporaneous with the S_1 state with a lifetime of 160 ± 60 fs can be assigned to the ME. This is underpinned by the energetic position, as this contribution is located approximately 0.95 eV below $E(S_1)$. At first glance this might seem confusing, as $E(ME) \approx E(S_1)$, but if a ME state gets ionized by the probing pulse, a T_1 state and an ionized molecule remain, in contrary to an ionization of a S_1 state, where an ionized and a ground state molecule remain. This leads to a difference of the kinetic energy of the photoemitted electron of approximately $E(T_1)$ [82], which also explains, why the electrons emitted from the ME state have the same energy as those from the T_1 state, and thus the peak assigned to the T_1 state is located at the same energy in the 2PPE spectrum. In agreement with TA measurements [90] the second lifetime of 1.9 ± 0.9 ps is expected to describe the energetic stabilization of the triplet followed by its decay of 620 ± 190 ps. The concluded results are displayed in figure 5.6. The result of TA measurements on spin coated films are added for the purpose of comparison [90]. These values equal the data obtained via 2PPE nicely. Even

5. Singlet Fission at the TIPS-Pentacene/Au(111) Interface

shorter lifetimes of 80 – 100 fs for singlet fission in spin coated TIPS-Pn films, where observed by Musser et al. [179] and Bakulin et al. [177], while Wu et al. [226] observed lifetimes of 360 fs and 73 ps for TIPS-Pn films evaporated onto a quartz substrates. The slight variations can be attributed to differences in sample preparation and a thus changed TIPS-Pn film morphology. In the case of Wu et al. additionally the reduced experimental time window might have influenced the obtained results.

Summarizing the present chapter, it was shown, that TIPS-Pn can be evaporated intact onto an Au(111) surface and well-defined monolayers can be prepared via heating the sample after multilayer deposition. Contrary to the multilayer, the monolayer does not desorb intact as the molecules show fragmentation around 570 K on the gold surface. A coverage estimation could be carried out via TPD measurements and the electronic structure at the interface was investigated via 2PPE and UPS, revealing several interface and molecule induced states, including the shifted SS' , two IPSs, the HOMO, the optical LUMO (S_1) and further higher and lower lying MOs. The optical gap was determined to be 1.87 eV . Beyond, the singlet fission dynamics within the evaporated TIPS-Pn films could be obtained via TR-2PPE. A coherent excitation of the ME state and the S_1 , followed by a contemporaneous decay on a 160 ± 60 fs timescale, was concluded. The resulting triplet stabilizes with a lifetime of 1.6 ± 0.9 ps and decays within 620 ± 190 ps . Furthermore, it was shown, that these lifetimes are coverage dependent for thin layers and decrease strongly with decreasing layer thickness.

6. Electronic Structure of N-Heteropolycyclic Molecules at the Metal-Organic Interface

In this chapter the investigations of Fe-5,10,15,20-tetra-pyridil-porphyrin (FeTPyP) and 10,17-Bis((triisopropylsilyl)ethynyl)dibenzo[a,c]-naphtho[2,3-i]phenazinen (TIPS-BAP, TIPS-diBenzodiAzaPentacene) adsorbed on Au(111) are presented. The investigation of a further N-Heteropolycycle, the 1,3,8,10-tetraazaperopyrene (TAPP) is presented in the following chapter 7. A multi-experimental approach, including scanning tunneling microscopy (STM), STS, 2PPE, UPS, electron ionization mass spectroscopy (EI-MS), and TPD measurements, was used to elucidate the electronic and adsorption structure at the FeTPyP/Au(111) and the TIPS-BAP/Au(111) interface.¹ First a short overview over porphyrins and their role in chemical and biological processes will be given, followed by first investigations of FeTPyP on Au(111) via STM and STS (section 6.1). Section 6.2 will then describe the sample preparation of the FeTPyP covered Au(111) substrate. The elucidation of the electronic structure at the interface will then be given in section 6.3. Some results of this sections (6.1 - 6.3) have been published in Ref. [65]. The second part of this chapter deals with the recently by Hoff *et al.* [94] synthesized N-Heteropolycycle TIPS-BAP including the state of research (section 6.4), sample preparation (section 6.5) and the description of its electronic structure (section 6.6).

¹STS and STM measurements were carried out by Daniela Rolf in the group of Katharina J. Franke at the Freie Universität Berlin. EI-MS measurements were carried out by the Mass Spectrometry Facility of the Institut of Organic Chemistry of the University of Heidelberg under the lead of Juergen Gross.

6.1. Porphyrins: Matured Molecules for Future Applications

Nature developed an important class of aromatic N-doped macrocycles, the porphyrins. These macrocycles consist of four pyrrole rings connected via methine groups forming porphine as the parent chemical compound of the porphyrins. This porphine can be substituted in several fashions giving nature a construction kit for various components for elementary chemical and biological processes. Porphyrins are stable molecules with a center surrounded by four nitrogen atoms, and so they are ideal tetradentate chelating agents. Their diversity, stability, and flexibility explains their importance in several biological processes e.g. as a compound of hemoglobin, cytochrome c, catalase, chlorophyll, and many more. Their function reaches from catalysts, over molecule transporters to energy transducers. In biological systems Fe, Co, or Mg center ions dominate, while human made porphyrins nowadays can incorporate nearly every metal from the periodic table. This variety makes porphyrins to an interesting part of research for more than one century by now [227]. Due to their easily tunable electronic properties, on the one hand by influencing or changing the chelated metal center and on the other hand by substituting the macrocycles, they are being examined for their suitability in organic electronics. These potential electronic devices often involve surface and interface related aspects and so a deeper understanding of the electronic properties of porphyrins at interfaces is crucial. Several studies regarding porphyrins at interfaces have been carried out providing a broad insight into this topic [107–115]. The high flexibility of the porphyrins allows external forces to influence their structure strongly, leading to intramolecular distortions and so surface dependent molecular geometries, as can be investigated well by STM studies [107, 109, 110, 112]. However, the interfacial electronic structure strongly depends on the adsorption geometry, which makes it necessary to gain information with additional methods. By now already a number of investigations clarify the electronic structure of porphyrins at surfaces by the use of UPS and IPS [228–235]. These publications focus on different combinations of porphyrins and metal surfaces including (*meso*-tetraphenyl-porphyrin (2H-TPP)) on Ag, Cu, Al, Mg and Au [229, 236], Zn(II)-5-(3,5-dicarboxyphenyl)-10,15,20-triphenylporphyrin dye (ZnTPP) on ZnO, TiO₂, Fe, Mg, Al, Cu, and Au [228, 231–234, 236, 237], tetra(4-aminophenyl)porphyrin (TAPPor) on Au(111) [235], zinc phthalocyanine and octaethyl-porphyrin (OEP) on Cu and Zn [230], and H₂-5,10,15,20-tetra(4-pyridyl)porphyrin (H₂TPyP) on Mg, Al, Cu, and Au [236]. However, these studies are restricted to IPS, having a limited energetic resolution and only access to electron affinity levels (negative ion resonances), and thus the

combination from UPS and IPS cannot give any information about exciton binding energies. In contrast, 2PPE has proven to be a powerful tool to elucidate the electronic structure at interfaces, unveiling occupied as well as unoccupied states, and in particular is able to observe the transport as well as the optical gaps [67, 68]. Fe-5,10,15,20-tetra-pyridil-porphyrin (FeTPyP) (see figure 6.1 (a)) is a further promising candidate for molecular switches, electronics and spintronics. The porphine core incorporates a Fe(III) ion with a Cl⁻ ligand serving as a counterion. Additionally, four pyridil substituents are connected in *meso* position.

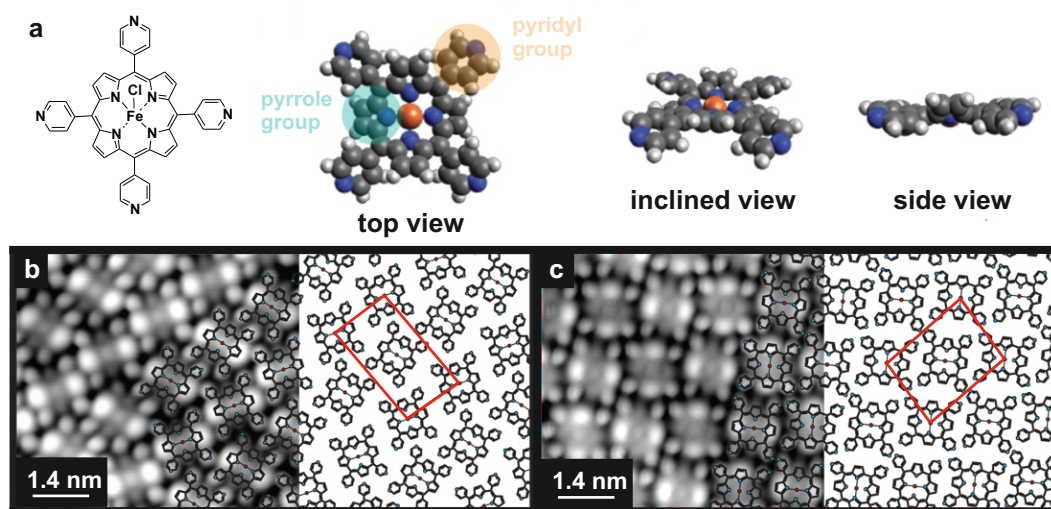


Figure 6.1.: (a) The Fe-5,10,15,20-tetra-pyridil-porphyrin (FeTPyP) molecule as a valence bond scheme and a structure model from different views, showing the out-of-plane saddle-shape deformation of the pyrrole groups. (b) & (c) Two different arrangements of FeTPyP molecules, either consisting of alternating rows of parallel molecules (b) or showing a staggered arrangement of FeTPyP with an alternating pattern of the molecules (c). The red box shows the rhombic unit cell of 1.4 nm x 2.7 nm, containing two molecules (b). The unit cell of 2.0 nm x 2.2 nm in (c) also contains two molecules. Because of the saddle-shape deformation of the molecules, two pyrrole groups of the molecules in both structures appear higher in the STM topography than the other two. Figure adapted from Ref. [116].

6. Electronic Structure of *N*-Heteropolycycles

K. J. Franke and coworkers [65, 116] carried out STM and STS measurements on FeTPyP. They could identify two different self-assembled adsorption geometries on an Au(111) surface displayed in Figure 6.1 (b) & (c). On the one hand there are molecules who assemble in alternating rows (b), and on the other hand there are molecules in a staggered arrangement (c). The well-ordered molecules form islands extending over tens of nanometers. In both arrangements the molecules can be found in a saddle-shaped configuration, where the inner macrocycle is distorted and one pair of pyrrole rings bends up while the other one bends down leading to different signals strengths in the STM topography. After deposition, the Cl^- seems to be removed from the center. This separation is accompanied by a reduction of the Fe(III) to Fe(II) and can be underpinned by measurements of inelastic spin excitations [65, 116, 238]. From STS experiments, dI/dV curves in the center of the molecule have been

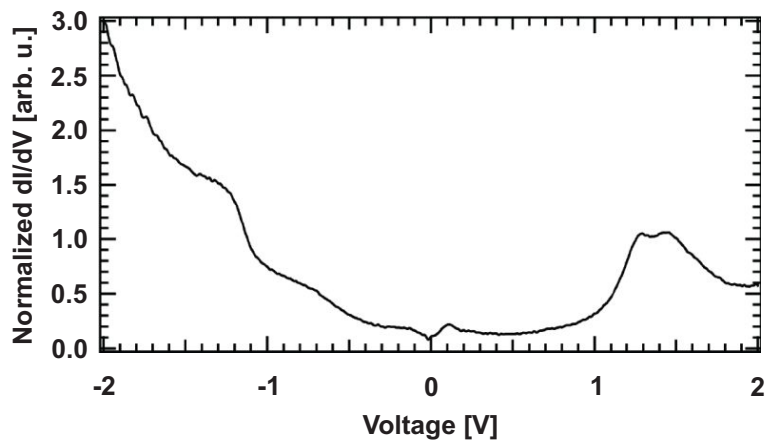


Figure 6.2.: dI/dV spectrum recorded in the center of an FeTPyP molecule on Au(111). Resonances at a positive bias voltage result from unoccupied molecular orbitals, while resonances with a negative bias voltage result from occupied molecular orbitals. Figure adopted from Ref. [65].

obtained as shown in Figure 6.2. At positive bias voltages there is a double-peak structure observed with maxima at 1.3 V and 1.45 V which have been assigned to the LUMO and the LUMO+1. Looking at negative bias voltages two resonances between -0.6 V and -1.3 V resulting from occupied orbitals can be seen. However, the resonances are rather broad, as STS shows a reduced resolution for occupied states, due to an increased tunneling barrier coupled to the negative bias voltages.

6.2. Sample Preparation and Coverage

Estimation of Fe-tetra-pyridil-porphyrin on Au(111)

In order to prepare the samples, the gold surface was cleaned as described in section 3.3.1. In the following the FeTPyP-Cl molecules were evaporated onto the surface by heating the effusion cell to 680 K while the surface was held at 300 K. During evaporation the Cl ligand was cleaved as shown by STM images and measurements of inelastic spin excitations [65, 116, 238]. In figure 6.3 an EI-MS Spectrum of FeTPyP-Cl is shown. As can be seen the most prominent signals within the range of the used QMS are related to a mass charge ratio of $m/z = 44$, 80 and 128. The fragments can be assigned to different isomers of the composition $C_2H_6N^+$, pyridinium, and $FeN_4CH_4^+$. However, to determine

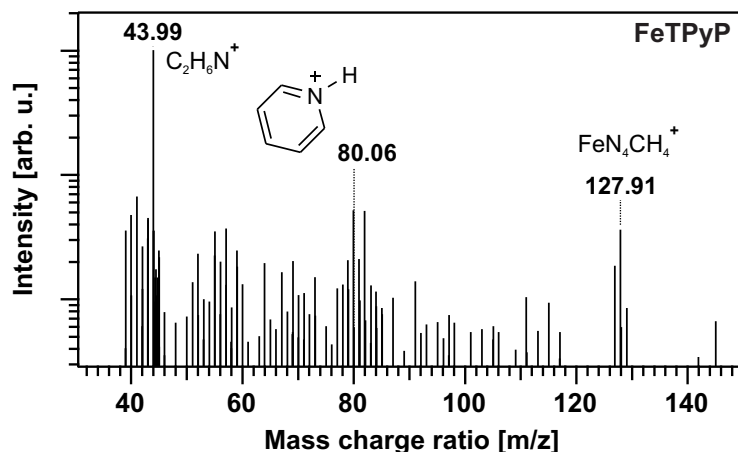


Figure 6.3.: EI-MS spectrum of FeTPyP with important fragments labeled. Intensity is given on a logarithmic scale.

the FeTPyP coverage on the gold surface, TPD measurements were carried out following the mass charge ratios of $m/z = 80$ and 128 during heating the sample to 750 K with a heating rate $\beta = 1 \text{ K/s}$. Figure 6.4 shows two different TPD measurements for different dosing times. For short dosing times there is no signal received, while for dosing times above 12 minutes and at a pressure of approximately $5 \cdot 10^{-9} \text{ mbar}$ (labeled as $\theta > 1 \text{ ML}$) a signal arises for both mass to charge ratios at a temperature around 580 K. The signals have a zero order shape and can so be attributed to a multilayer desorption. This leads to the assumption that there is no signal detectable for submonolayer coverages, probably due to strong interactions of the molecules with the metal

6. Electronic Structure of *N*-Heteropolycycles

surface, which prevents an intact desorption of the molecule from the surface. Exceeding the monolayer coverage molecules can be desorbed leading to the observed signals during the TPD measurements. So, unfortunately, the TPD measurements can not be used directly to determine the coverage, but we can estimate the dosing time to receive a coverage of one monolayer. Assuming a constant evaporation flux, we so can conclude to the coverage dosed during a specific time. The absence of a signal with $m/z = 35$ substantiates the cleavage of the Cl^- during evaporation and shows that the cleaved ion does not seem to adsorb separated on the surface.

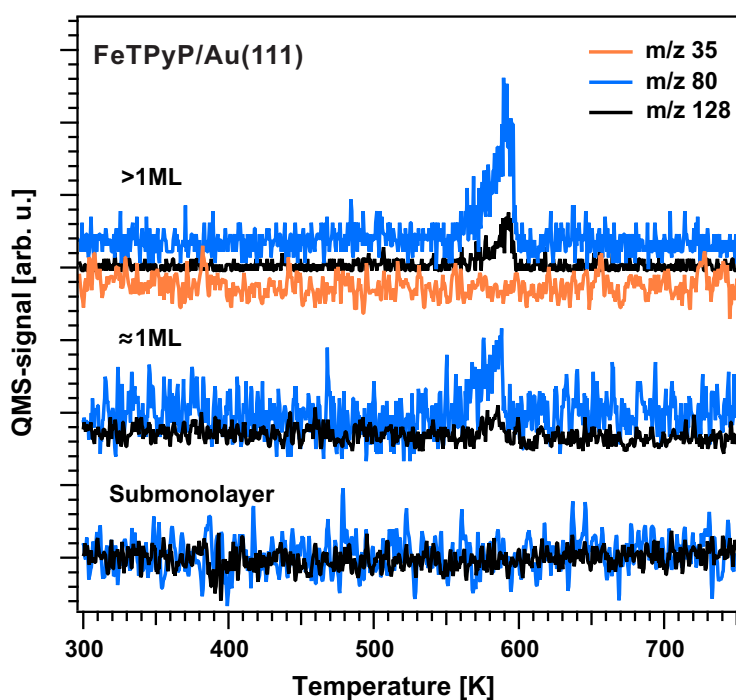


Figure 6.4.: TPD measurement of FeTPyP adsorbed on Au(111) for three different dosing times resulting in different coverages (Θ). For each Θ mass charge ratios of $m/z = 80$ and $m/z = 128$ have been recorded. For the highest Θ a mass charge ratio of $m/z = 35$ is additionally shown to exclude Cl^- adsorption. For clearance the spectra are shown with individual offsets. The lower spectra correspond to a submonolayer coverage, while the upper spectra correspond to a coverage around and slightly above one monolayer (ML). The multilayer data was recorded by Friedrich Maass, AK Teger, Universität Heidelberg.

6.3. Electronic Structure at the Fe-tetra-pyridil-porphyrin/Au(111) Interface

In the following we will discuss the results of UPS and 2PPE measurements of FeTPyP adsorbed on the Au(111) surface, resulting in a fundamental insight into the electronic structure at the metal/organic interface. In overall eleven electronic states, including four unoccupied molecular orbitals, the first IPS ($n=1$), one excitonic state, the Shockley surface state (SS) and four further occupied molecular orbitals are revealed. Figure 6.5 shows UPS spectra for several different coverages of FeTPyP, starting from the bare Au(111) surface and increasing up to one monolayer, taken with a photon energy of $h\nu = 6.2$ eV. The spectrum of the bare Au(111) surface is mainly dominated by the SS located at -0.48 ± 0.05 eV with respect to E_F as already mentioned in section 4. By adsorbing molecules the SS loses intensity, while an about 0.28 eV energetically upwards shifted SS' appears for low coverages of FeTPyP. By increasing the coverage of FeTPyP further the primarily shifted SS gets quenched again and starting from a coverage of approximately 0.4 monolayers, molecule-induced peaks are observed, which can be assigned to photoemission from the HOMO and three lower lying OMOs. For clearance the data are fitted by an exponential background and Gaussian-shaped peaks. In detail the observed peaks are located at -0.91 ± 0.08 , -1.12 ± 0.08 , -1.33 ± 0.08 , and -1.49 ± 0.08 eV. These values are in rough agreement with the data obtained by STS measurements [65], but as discussed before STS shows a reduced resolution and only broad peaks were obtained. The values obtained by UPS and 2PPE, further are ensemble-methods, while STS is measured locally in the center of a single molecule. The shift of the surface state is a well-known phenomena on covered noble metal surfaces, as it has been reported for various adsorbates like noble gases [126, 132, 133], or molecular layers [128–131]. It is caused by either interfacial charge transfer processes or modifications of the surface work function [225]. A strong adsorbate-induced decrease of the work function from 5.5 eV to 4.5 eV is observed, for a coverage up to 1 ML. As described in section 2.1.3 the work function shift can be regarded as interplay of the push-back effect, molecular dipole moments, and CNL level alignment (refer to section 2.1.3). In overall a rather strong interaction between metal surface and molecule is concluded, which would also agree with the missing monolayer desorption in the TPD measurements.

To determine the energetic position of unoccupied states, 2PPE measurements have been carried out. Figure 6.6 (a) shows monochromatic ($h\nu_1 = h\nu_2$) 2PPE

6. Electronic Structure of N-Heteropolycycles

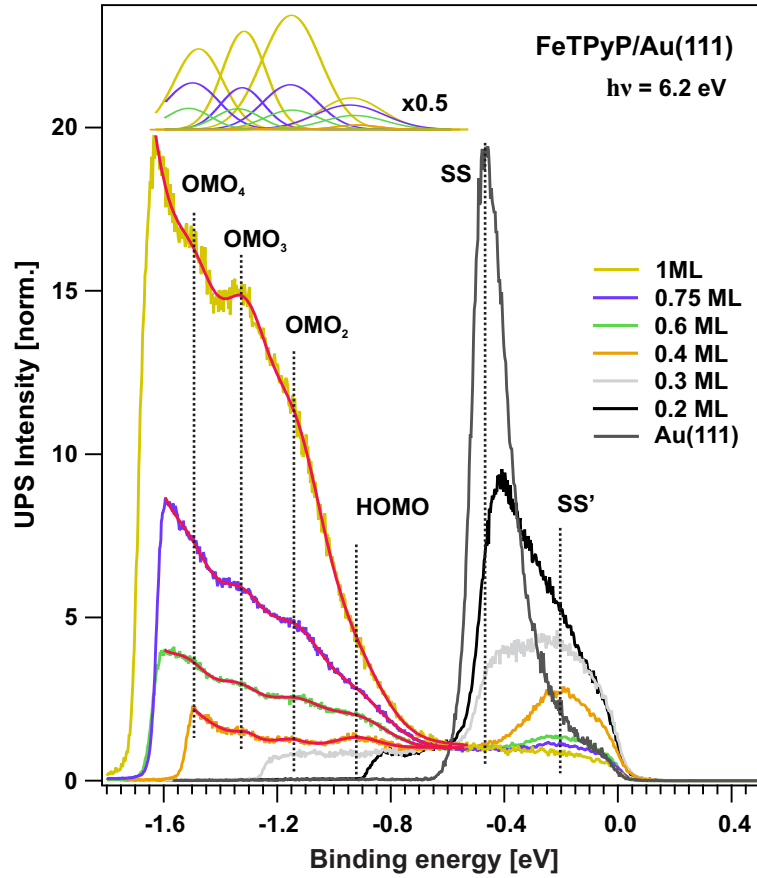


Figure 6.5.: UPS spectra ($h\nu = 6.2\text{eV}$) of various submonolayer coverages of FeTPyP on Au(111). Data are fitted by an exponential background combined with Gaussian-shaped peaks. Dotted lines highlight peaks resulting from occupied molecular orbitals (OMO), the Shockley surface state (SS), and the shifted surface state (SS'), and for clearance the fitted peaks are shown as an inlay. Figure adapted from Ref. [65].

spectra of 1 ML FeTPyP adsorbed on Au(111) for different photon energies. Contributions of several electronic states are observed. To assign these contributions properly their energetic position with respect to the used photon energy is shown in figure 6.6 (c).² Besides the well-known d-band features, in the low energy region of the spectra ($E_{Final} - E_F = 4.5\text{eV} - 7.0 \text{ eV}$), contributions of a final state ($E_{Final} - E_F = 5.18 \pm 0.08 \text{ eV}$) are observed.³ Further,

²refer to section 3.2 for more slope evaluation details

³Final state peaks can occur from unoccupied molecular orbitals located above the global

6.3. Electronic Structure FeTPyP/Au(111)

for high photon energies we find a contribution, showing a slope of one, and therefore originating from an intermediate state, which in agreement with STS measurements [65], is assigned to the LUMO+1 located 1.44 ± 0.09 eV above E_F . In between the LUMO+1 and the final state (FS) a further contribution is observed for high photon energies, but its energetic position can not be determined clearly, and so is not plotted in graph 6.6 (c). However, it can be assigned to the LUMO located 1.29 ± 0.07 eV above E_F as determined via dichromatic measurements (see below) and STS measurements [65]. In the enlarged shown high energy region of figure 6.6 (a) three additional peaks can be observed. Two of them showing a slope of about two, and so, in agreement with the UPS measurements shown in figure 6.5, originate from the HOMO and the OMOs₂₋₄, the latter here appearing as only one broad feature. From the slope evaluation of photon energy dependent measurements the third peak can be assigned to an intermediate state with its energetic position at 3.87 ± 0.07 eV above E_F and so 0.57 eV below E_{vac} , which corresponds well to the first ($n = 1$) IPS with an adsorbate induced quantum defect of $a = 0.22$. This quantum defect also is a clear hind for adsorbate-surface interactions, as for a clean undisturbed Au(111) surface a quantum defect of $a = 0$ is expected [134]. As mentioned above, the LUMO was not clearly observed within the 2PPE measurements with monochromatic photons, so to get a deeper insight, dichromatic measurements $h\nu_1 = \frac{1}{2}h\nu_2$ where carried out. The results can be seen in figure 6.6 (b) & (d), where (b) shows the dichromatic 2PPE spectra of 1 ML FeTPyP on Au(111) for different photon energies and (d) shows the photon energy dependent peak positions. To observe the correct peak positions the data in (b) were fitted with three to four Gaussian-shaped peaks. Besides contributions of the already known shifted SS' and the IPS ($n=1$) there are two contributions originating from unoccupied states. On the one hand the LUMO can be clearly identified, being located at 1.29 ± 0.1 eV above E_F which is in good agreement with the LUMO received from STS measurements [65] and confirms the LUMO assignment in the monochromatic evaluations above. On the other hand a further energetically lower lying contribution, resulting from an electronic state located at 0.87 ± 0.1 eV above E_F , can be identified. Here it must be pointed out, that STS measurements only have access to transport levels, because electrons tunnel into unoccupied molecular orbitals or states forming negative ion resonances. For 2PPE additionally to the transport levels populated from the metal substrate, an exciton generation by excitation from an occupied into an unoccupied molecular orbital is possible. 2PPE then

vacuum energy E_{vac} , and so show a slope of zero in photon energy dependent measurements, because both photons applied in the 2PPE process are needed to populate these orbitals. Due to their position above E_{vac} , a direct detachment of the electron leads to the observed signal.

6. Electronic Structure of N-Heteropolycycles

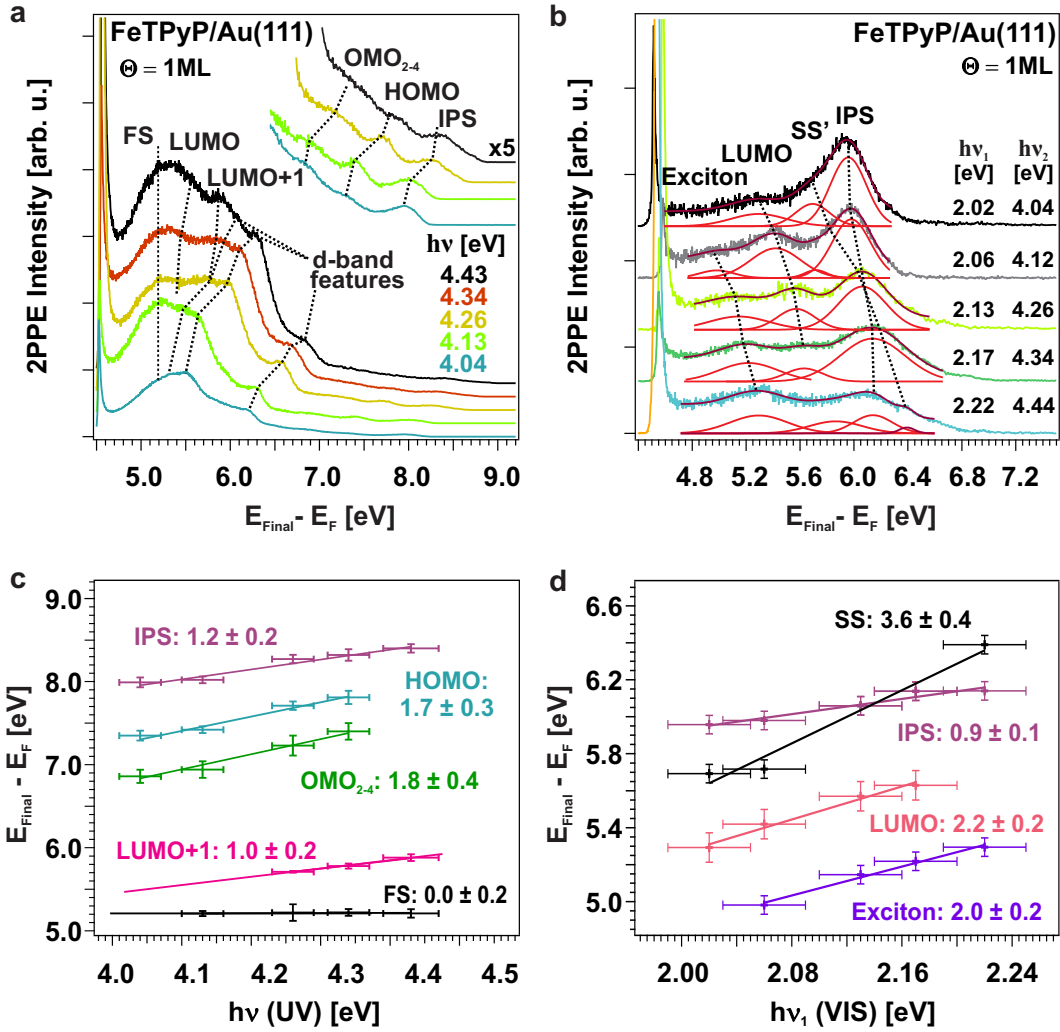


Figure 6.6.: (a) Monochromatic and (b) dichromatic 2PPE spectra of FeTPyP on Au(111) recorded with several photon energies. 2PPE intensity is given as a function of the final state energy. The dichromatic spectra were fitted with multiple gauss peaks to increase clarity. Dotted lines highlight peaks resulting from (the highest) occupied molecular orbitals ((H)OMO), (the lowest) unoccupied molecular orbitals ((L)UMO), a final state (FS), the first image potential state (IPS), and the shifted surface state (SS'). (c) and (d) show the corresponding photon energy dependent peak positions to assign peaks observed in the 2PPE spectrum. Figure adapted from [65].

measures the IP of this exciton. The electronic state observed at 0.87 eV, and so below the lowest unoccupied transport level, is thus assumed to be an excitonic state, leading to an exciton binding energy of 420 meV, which is at the lower edge of typical exciton binding energies in organic semiconductors (0.5 – 1.0 eV) [157]. In this context, it must be mentioned, that the exciton binding energy of a molecule adsorbed on a surface can be influenced by screening effects leading to variations compared to UV/Vis measurements. To gain more information about the exciton it would be advantageous to carry out TR-2PPE measurements, but unfortunately weak illumination effects on the sample are obtained preventing long lasting time resolved measurements. However, the illumination effects are sufficient weak so that no significant changes are observed in the spectra within the normal measuring window as can be seen in appendix B.1.

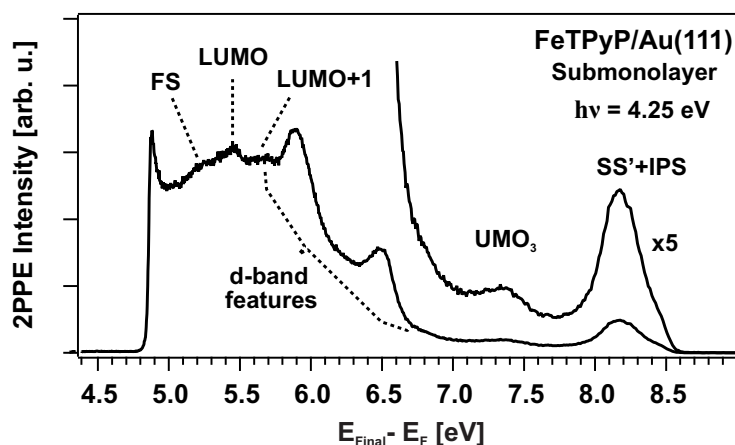


Figure 6.7.: 2PPE spectrum of a submonolayer coverage FeTPyP adsorbed on Au(111) taken with a photon energy of 4.25 eV. (L)UMO denotes (the lowest) unoccupied molecular orbitals, FS a final state, IPS the image potential state, and SS' the shifted surface state.

To complete the picture of the electronic structure of FeTPyP adsorbed on Au(111) further coverages, besides the 1 ML coverage described above, have been investigated via 2PPE. Figure 6.7 shows a monochromatic ($h\nu = 4.25$ eV) 2PPE spectrum of a low covered surface with approximately 0.3 ML.^{4,5} Here the FS and the LUMO can be seen more clearly separated. A misassignment of these to further gold d-band features can be ruled out, due to an increasing

⁴For all photon energy dependent measurements and the associated slope evaluation refer to appendix B.2.

⁵A monochromatic 2PPE measurement series with different coverages can be found in B.3.

6. Electronic Structure of *N*-Heteropolycycles

intensity of these peaks with increasing coverage and the assignments based on figure 6.6. Interestingly, a further molecule-induced contribution is observed in the high energy region of the spectrum, which is overwhelmed by the peaks originating from the occupied molecular orbitals in the monolayer spectra. This further contribution is assigned to an UMO_3 located at $3.07 \pm 0.06 \text{ eV}$ above E_F . To rule out a misassignment to the occupied sp-band feature, which also could be expected in this region of the spectrum and shows a comparable slope for the photon energy dependent peak position, AR-2PPE measurements have been carried out. The results are shown in the appendix in figure B.4. Only the peak assigned to the IPS and shifted SS shows a dispersion with an effective mass of $m_{eff} = 1.17 \pm 0.29m_e$. From this we can conclude that the peak is mainly dominated by the IPS, because, as mentioned in section 2.1.1, a SS should show a dispersion with an effective mass of 0.2 to 0.3 m_e , while for an IPS an effective mass of around 1.2 m_e is expected [146, 224, 239]. The peak originating from the UMO_3 shows no dispersion and so proves the correct assignment.

Combining the presented results we obtain the electronic structure of the FeTPyP/Au(111) interface (see figure 6.8). Besides the d-band features and the SS of the underlying substrate surface, eleven electronic states have been observed. These are the shifted SS', the IPS($n=1$), and several molecule-induced states, including an exciton, the HOMO, the LUMO (affinity level), and further higher, respectively lower lying UMOS and OMOs. At 1 ML coverage the HOMO is located at -0.91 eV with respect to E_F , and thus shows an ionization potential of 5.41 eV . For the purpose of comparison, refer to the publication of Yamashita and coworkers [236], where they observed the onset of the HOMO of H_2TPyP at approximately -1.1 eV below E_F for a 5 nm thick layer on a gold surface (work function (WF) = 4.7 eV). With the LUMO, populated by an electron out of the gold bulk, located at 1.29 eV with respect to E_F , and thus showing an electron affinity of 3.21 eV , a transport gap of 2.2 eV is determined. The, as well, observed excitonic state, where the LUMO is populated by an intramolecular excitation, is located at 0.87 eV with respect to E_F exhibiting an exciton binding energy of 420 meV . The resulting optical gap is thus estimated to be 1.78 eV .

Considering all results, after deposition at room temperature well-ordered islands of FeTPyP on Au(111) have been received as shown by STM. Via STS the negative ion resonances, for the two lowest unoccupied molecular orbitals, LUMO and LUMO+1 have been received [65]. The picture of the electronic structure was complemented by UPS measurements, to determine initial states, and by 2PPE to, on the one hand add the picture of the intermediate states,

6.3. Electronic Structure FeTPyP/Au(111)

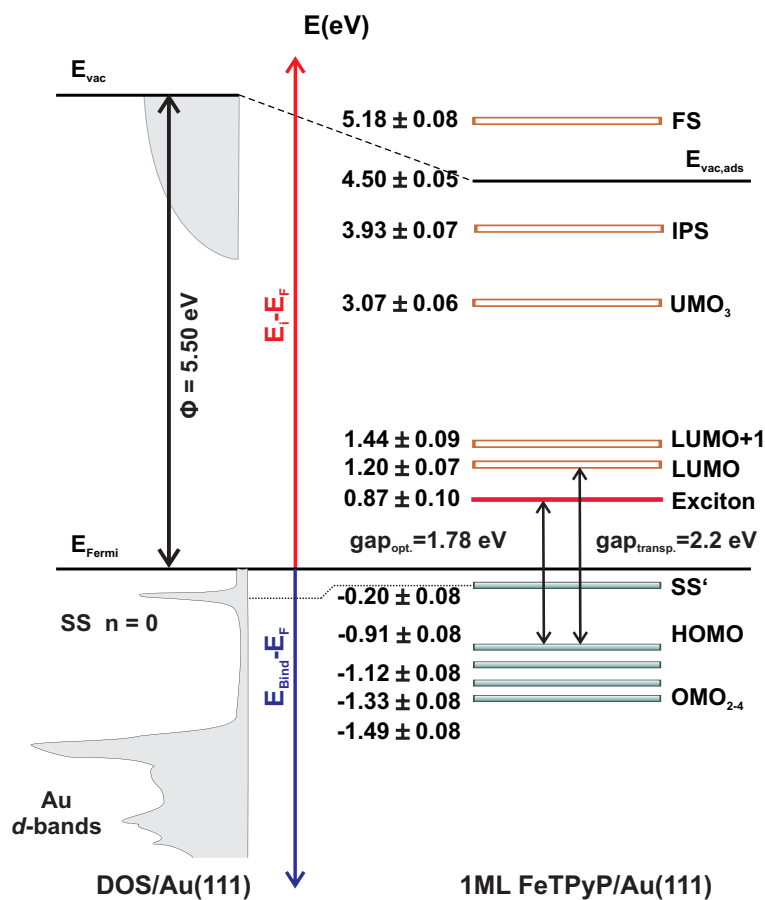


Figure 6.8.: Energy level diagram of one monolayer FeTPyP adsorbed on Au(111). On the left the density of states (DOS) of the bare gold surface is shown. Unoccupied electronic states are shown in red, while occupied electronic states are shown in blue. The molecule-induced surface state and work function shifts are highlighted by dashed lines. The energetic positions are given with respect to the Au(111) Fermi level (E_F).

and on the other hand, reveal the energetics of intramolecular photoexcitation at the interface.

6.4. Arrow-shaped N-Heteroacenes: Potential n-type Organic Semiconductors

Acenes with five or more polycycles have shown to be promising organic semiconductors, but show a lack on stability and solubility [70–72, 240–243]. To overcome this drawbacks TIPS-groups can be added as first done by Anthony *et al.* [74]. However, for larger acenes than pentacene even bulkier silyl-groups only provide moderate stability [87–89] and thus additional efforts have been made to stabilize these acenes [87, 243–245]. One approach was to add two additional benzene rings forming an arrow-shaped molecule [87]. In general acenes are rather p-type semiconductors but the substitution of CH units by nitrogens can lead to energetically stabilized acenes with lower lying HOMOs and LUMOs [90–95]. This increases the electron affinity, which is necessary for the formation of appropriate n-type semiconductors. Therefore, N-heteroacenes have become a field of great interest [94, 246–249], and have shown to work well in thin-film transistors [90, 250, 251]

Combining these two approaches, on the one hand stabilization via additional benzene rings and on the other hand forming a n-type semiconductor via nitrogen substitution leads to the 10,17-Bis((triisopropylsilyl)ethynyl)dibenzo[a,c]-naphtho[2,3-i]phenazinen (TIPS-BAP, TIPS-diBenzodiAzaPentacene), a novel compound first synthesized in 2016 by Hoff *et al.* [94] (see figure 6.9 (a)). This well-soluble molecule forms well-ordered crystals that pack “in a brick-wall-like motif with head-to-tail arrangement” [94], with a short distance between the π -conjugated backbones (see figure 6.9 (b)). This close packing is favorable for molecular electronic applications [94, 251] and therefore TIPS-BAP is a promising candidate for investigations at the metal/organic interface.

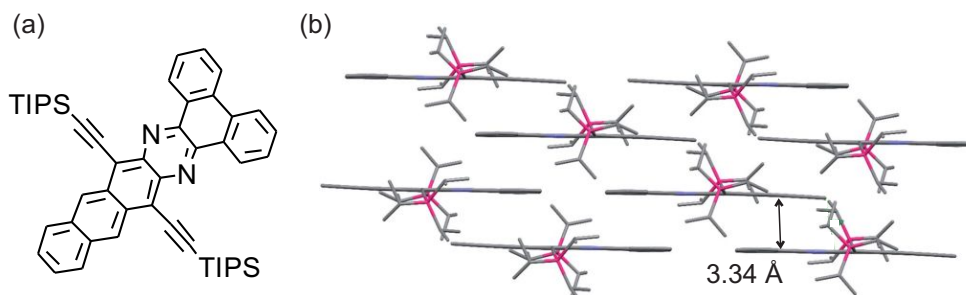


Figure 6.9.: Valence bond scheme (a) and single crystal packing (b) of TIPS-BAP. Figure adapted from Ref. [94]

6.5. Sample Preparation of the arrow-shaped N-Heteroacene on Au(111)

After cleaning and preparation of the Au(111) surface, according to the procedure described in section 3.3.1, TIPS-BAP was evaporated onto the surface with an effusion cell held at a temperature of 548 K and a substrate temperature of 300 K. The batch of molecules used in the framework of this thesis were synthesized by Matthias Müller in the group of Prof. Dr. Bunz at the University of Heidelberg according to the publication of Hoff *et al.* [94]. Figure 6.10 shows the EI-MS spectrum of TIPS-BAP as synthesized and after heating in the effusion cell.⁶ The EI-MS spectra are identical and thus a decomposition during the evaporation process can be excluded. The inset in figure 6.10 shows the part of the spectrum enlarged, which is accessible by the QMS used in our setup. Here important fragments are labeled. The most intense fragments $m/z = 59, 73, 87, 115, 180$ result from the TIPS side groups and unfortunately no backbone fragments can be detected within our experimental range. The fragments used for TPD measurements are shown in detail in the lower part of the figure.

TPD spectra (ionic fragment $m/z = 59$) for TIPS-BAP adsorbed on Au(111) are shown in figure 6.11. At low temperatures around 465 K a strong peak labeled as α_1 with a typical zero-order desorption-shape is observed, which can thus be assigned to the multilayer desorption. At 480 K a further contribution α_2 is observed, which most likely results from molecules adsorbed in a compressed phase as reported for several organic molecules on noble metal surfaces [69, 222, 252–257]. Around 560 K a peak α_3 is observed, which can be assigned to desorptions from the monolayer. The inset shows equivalent measurements at an initial multilayer coverage for different mass charge ratios ($m/z = 59, 115, \text{ and } 180$). It must be pointed out that the relative intensities between the mono- and multilayer peaks differ strongly for different m/z . This is a clear hint for a decomposition and incomplete desorption of the monolayer molecules, and thus TIPS-BAP shows a comparable behavior as TIPS-Pn (refer to section 5.2). A coverage estimation via TPD measurements for TIPS-BAP adsorbed on Au(111) is excluded, because of the strong deviation of the relative peak intensities. However, as the multilayer peak shows a typical shape and the EI-MS spectrum reveals an intact desorption from the effusion cell, an intact multilayer desorption from the substrate can be assumed and thus well-defined monolayers of TIPS-BAP on Au(111) can be prepared by

⁶EI-MS measurements were carried out by the Mass Spectrometry Facility of the Institut of Organic Chemistry of the University of Heidelberg under the lead of Juergen Gross.

6. Electronic Structure of N-Heteropolycycles

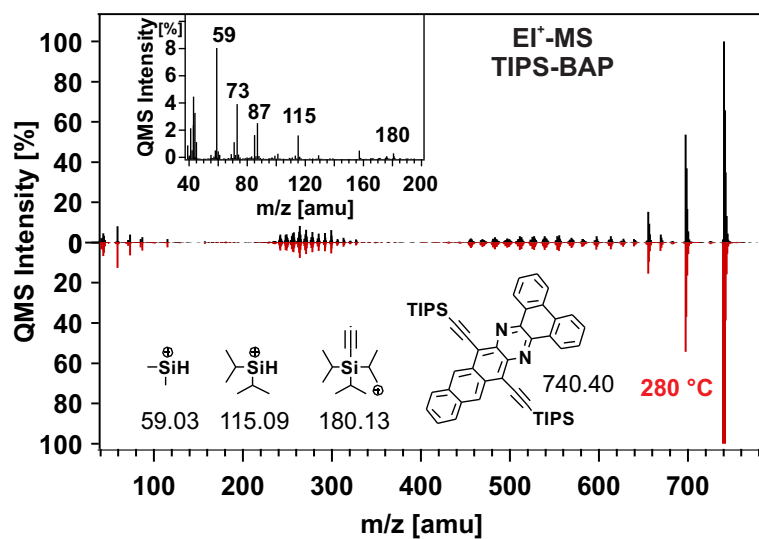


Figure 6.10.: EI-MS spectrum of TIPS-BAP, as synthesized (upper part) and after heating inside the doser (lower part). The part of the spectrum observable by the QMS attached to the UHV chamber is shown enlarged in the inset. Important fragments are labeled.

the creation of a multilayer coverage via evaporation and subsequent heating to 490 K.

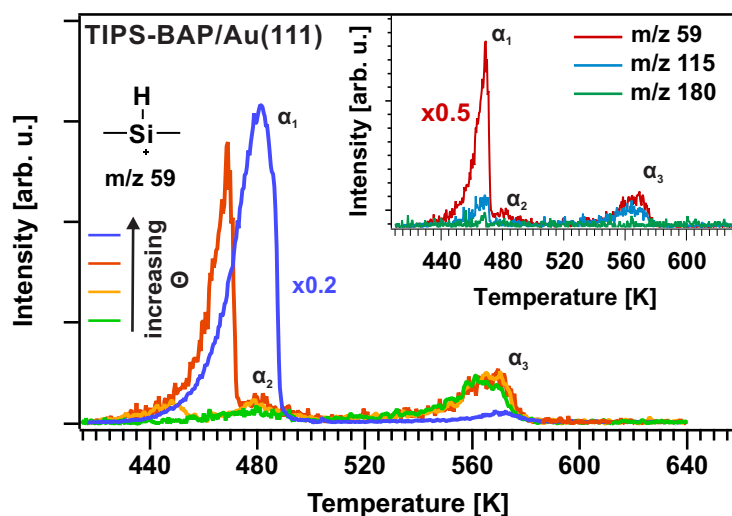


Figure 6.11.: TPD measurements (ionic fragment $m/z = 59$) of TIPS-BAP adsorbed on Au(111) for different initial coverages (Θ) recorded with a heating rate of 1 K/s . A clear coverage determination is not possible (see text). α_3 denotes the monolayer and α_1 the multilayer desorption peak. The contribution labeled as α_2 most likely results from a compressed phase. The inset shows equivalent measurements for an initial multilayer coverage for different mass charge ratios.

6.6. Electronic Structure of the arrow-shaped N-Heteroacene/Au(111) Interface

To gain insight into the electronic structure of the TIPS-BAP/Au(111) interface 2PPE measurements have been carried out. At a well-defined monolayer, spectra with several features resulting from the underlying gold surface and the adsorbed molecules can be obtained as can be seen in figure 6.12. While figure 6.12 (a-c) shows monochromatic measurements, figure 6.12 (d) shows dichromatic measurements for several photon energies at a coverage of 1 ML each. In total three d-band features, six additional peaks, and a work function reduction of $850 \pm 50 \text{ meV}$ are observed. The assignment of the observed peaks was carried out *via* energy-dependent measurements and the subsequent evaluation shown in figure 6.12 (e) and (f), revealing three intermediate and three initial states. Their energies with respect to E_{Fermi} are $E_{OMO} = -3.11 \pm 0.07 \text{ eV}$, $E_{HOMO} = -1.12 \pm 0.09 \text{ eV}$, $E_{SS'} = -0.25 \pm 0.10 \text{ eV}$, $E_{exciton} = 0.62 \pm 0.08 \text{ eV}$, $E_{UMO_1} = 3.75 \pm 0.07 \text{ eV}$, and $E_{UMO_2} = -3.97 \pm 0.07 \text{ eV}$. The initial state

6. Electronic Structure of *N*-Heteropolycycles

only observed as a weak contribution for high photon energies directly at the Fermi edge is assigned to the shifted and nearly quenched SS' as its energetic position is in good agreement with shifted SS' for other molecule covered surfaces (refer to section 5.3, 6.3, 7.3 and Refs. [128–131]). The two intermediate states with their contributions also located directly at the secondary edge seem to be molecule-induced and thus are assigned to UMOs. As a result of the work function shift the first IPS could also be expected in this area of the spectrum. To rule out a misassignment AR-2PPE measurements have been carried out. However, the two contributions do not show any significant dispersion (see appendix C.2 (b)) which would be a necessary condition for an IPS. The observation of the shifted SS' and the two UMOs gets underpinned by dichromatic measurements as displayed in figure 6.12 (d). At a final state energy of about 7 eV a weak contribution of an initial state is observed (for clarification fitted by an exponential background and a Gaussian-shaped peak in figure 6.12 (c)). Being energetically the highest occupied molecule induced contribution in the spectra it is assigned to the HOMO. Energetically below the well-known d-band features of the underlying gold surface, a further initial state is observed, which is assigned to a lower lying occupied molecular orbital. For high photon energies a broad contribution of an intermediate state is observed near the secondary edge, which is assigned to an optically excited LUMO (exciton). The optical gap can be determined to be 1.74 eV, which is in good agreement with the optical gap of 1.92 eV observed *via* UV/Vis in solution [94] and of 1.88 eV observed *via* HREELS.⁷ The 2PPE data were obtained at a monolayer coverage, while UV/Vis and HREELS data are gained in solution and at a multilayer coverage, respectively. Therefore the slight deviations of the optical gap can be attributed the electronic coupling between the molecules and the surface [67, 68].

⁷unpublished HREELS data measured by Mohsen Ajdari in the group of Prof. Dr. Petra Tegeder at the University of Heidelberg

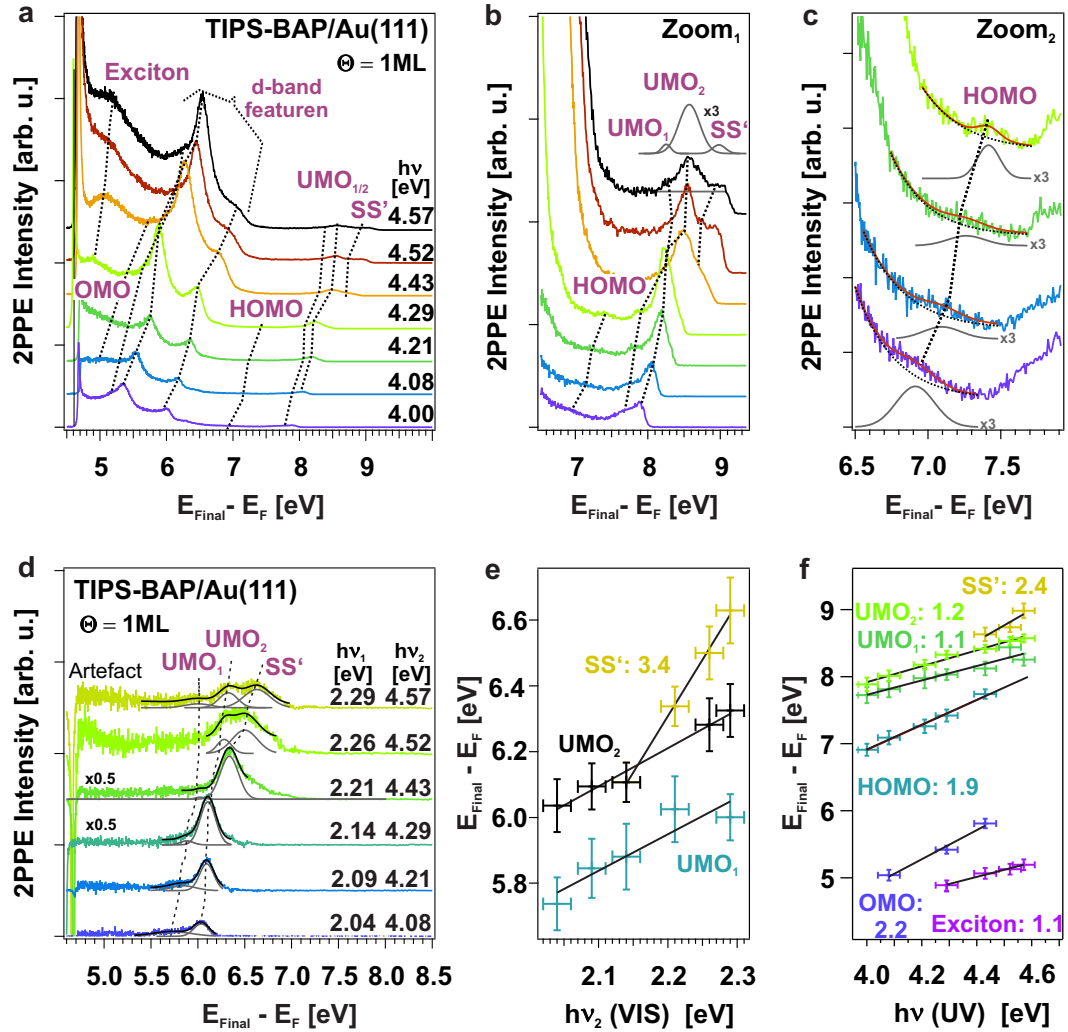


Figure 6.12.: (a, b, c) Monochromatic and (d) dichromatic 2PPE spectra of TIPS-BAP adsorbed on Au(111) recorded with different photon energies. 2PPE intensity is given as a function of the final state energy. Peaks resulting from (the highest) occupied molecular orbitals ((H)OMO), (the lowest) unoccupied molecular orbitals ((L)UMO), and the shifted surface state (SS') are highlighted by dashed lines. Additionally, some spectra were fitted by an exponential background and multiple Gaussian-shaped peaks to increase clarity. (e) and (f) show the corresponding photon energy dependent peak positions to assign peaks observed in the 2PPE spectrum.

6. Electronic Structure of N-Heteropolycycles

To gain further information about the exciton it would be advantageous to carry out TR-2PPE measurements. Unfortunately TR-2PPE measurements were not possible on TIPS-BAP covered Au(111) surfaces since photodegradation seems to take place during long-lasting exposure of the sample to the laser beam, as can be seen in appendix C.1 and C.2 (a). Figure C.1 (a) shows a strong increase of the signal at the secondary edge, probably resulting from decomposed molecular fragments on the surface, while (b) shows a clear change of the spectrum in the high energy region. The weak HOMO contribution vanishes entirely, while the $UMO_{1/2}$ contributions merge into one peak. The strong increase of the signal at the secondary edge also is the origin of the artefacts observed at the secondary edge of the dichromatic measurements displayed in figure 6.12 (d). At multilayer coverages the effect is even stronger as can be seen from figure C.2 (a). Within an illumination time of 15 *min* the 2PPE features in the spectrum seem to vanish nearly entirely, resulting in an undefined secondary electron background. This once more is a hint for a photodegradation of the molecules caused by irradiation with the laser beam. However, for short lasting measurements the changes are negligible small as can be seen from figure C.1 (c) and (d) and thus the evaluation of the electronic structure at the interface is valid.

The electron structure of 1 ML TIPS-BAP adsorbed on Au(111) determined by 2PPE can be found in figure 6.13. In total five molecule-induced electronic states and the shifted SS' are observed at the interface. Namely, these are the HOMO, an optically excited LUMO (exciton), two higher lying UMOs, and one lower lying OMO. The optical gap (1.74 *eV*) obtained *via* 2PPE at a monolayer coverage is slightly smaller than the one observed *via* UV/Vis (1.92 *eV*) measurements in solution [94] or *via* HREELS measurements (1.88 *eV*) at a multilayer coverage, which can be attributed to the electronic coupling between the molecules and the surface. The work function shift of about 850 *meV* resulting in a work function of 4.65 *eV* is identical to the shift observed for the TIPS-Pn/Au(111) interface (see section 5.3). The work function shift is the result of an interplay between CNL-level alignment, induced dipoles and the push-back effect as explained in section 2.1.3.

The present chapter treated the electronic structure of two N-Heteropolycycles adsorbed on Au(111). In the first part (section 6.1 - 6.3) a compound of the molecular class of the porphyrines, the FeTPyP, was investigated by a multi-experimental approach including several surface sensitive methods as STM, STS, UPS, 2PPE, and TPD. A well-ordered surface structure has been received and the electronic structure of the interface was clarified. Besides the first IPS and the shifted SS' several molecule-induced electronic states in-

6.6. Electronic Structure of N-Heteropolycycles

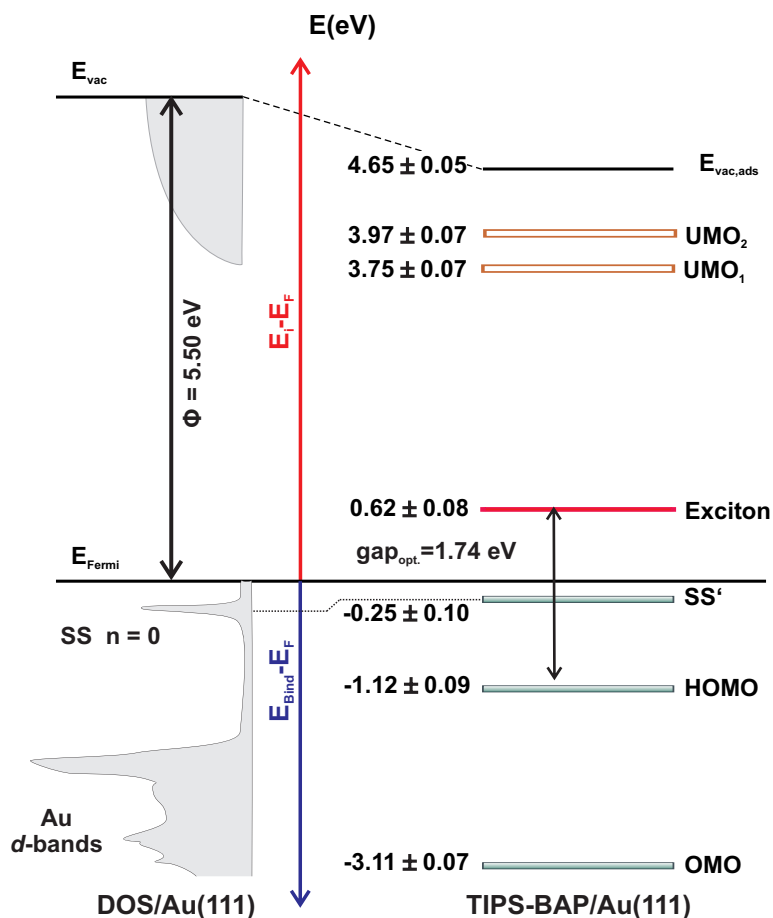


Figure 6.13.: Energy level diagram of 1 ML TIPS-BAP adsorbed on Au(111). On the left the DOS of the bare gold surface is shown. Unoccupied states are shown in red, while occupied states are shown in blue. The shift of the surface state and work function are highlighted by dashed lines. The energetic positions are given in respect to the Au(111) Fermi level (E_F).

cluding the HOMO, the transport LUMO, and the optical LUMO (exciton) were determined. The second part of this chapter (section 6.4 - 6.6) focused on the investigation of a novel n-channel semiconductor, the N-heteroacene TIPS-BAP. An investigation *via* TPD and 2PPE revealed a successful sample preparation via evaporation. Additionally, the electronic structure at the interface was determined, including the energetic positions of the HOMO and optical LUMO (exciton), besides further energetically higher and lower lying MOs. Porphyrines as well as N-heteroacenes are promising organic materials for semiconductor applications and therefore a quantitative determination of the en-

6. *Electronic Structure of N-Heteropolycycles*

energetic positions of molecular orbitals in direct contact to a metal electrode is crucial for the improvement and optimization of organic semiconductor based devices, as e.g. transistors or organic photovoltaics.

7. Band Formation at the Metal/Organic Interface

In this chapter a further aromatic N-heteropolycycles, the 1,3,8,10-tetraazaperopyrene (TAPP) and its fluorinated alkyn chain substituted derivatives (TAPP-(CF₃)₂ and TAPP-(C₃F₇)₂) (see figure 7.1), will be investigated, where the focus will lie on the interfacial hybrid band formation between molecular orbitals and metal bands. This band formation should foster efficient charge injection between the metal electrode and the organic semiconductor, which is crucial for the performance of organic semiconductor based devices in particular for organic field effect transistors.

Band formation in organic molecular crystals [55–58] is widely known, but so far band formation at the metal/organic interface is rare. Dispersion is a clear hind for efficient band formation, but it should be noted that most dispersing states at interfaces observed so far result from the modified SS of the metal substrate [129, 258–266]. Exceptions are a few metal/organic interfaces with strong electron donor or acceptor molecules, where in all cases a charge transfer has been proposed. Namely, these are 3,4,9,10-perylene-tetracarboxylic-dianhydride (PTCDA) [59], 1,4,5,8-naphthalenetetracarboxylic-dianhydride (NTCDA) [60], tetrafluoro-tetracyanoquinodimethane (F4TCNQ) [61, 62] and tetrathiafulvalene (TTF) [61]. However, this charge transfer might limit further charge injection at the metal/organic interface and therefore a band formation at a more weakly interacting interface, as it is the case for TAPP on Au(111), could be advantageous.

In section 7.1 a short introduction into the state of research regarding the TAPPs will be given, followed by the sample preparation and the determination of the electronic structure (section 7.2 and 7.3). Finally, the dispersion of electrons at the interface will be studied, identifying efficient band formation.

7. Band Formation at the Metal/Organic Interface

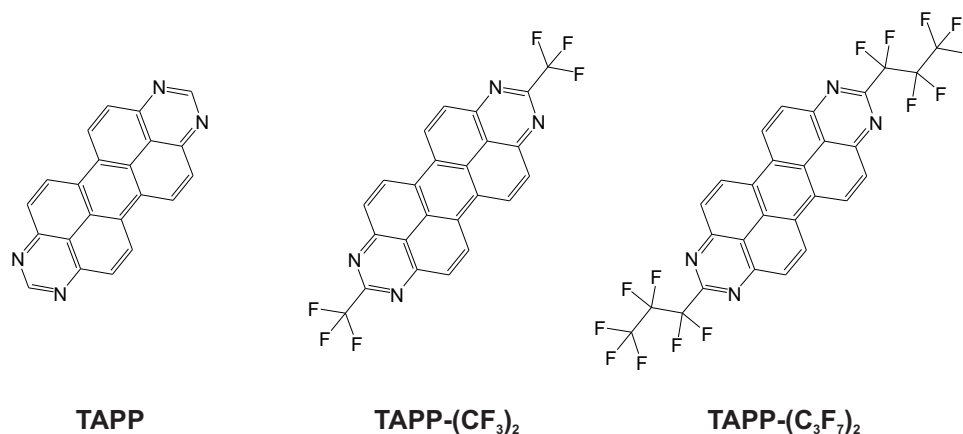


Figure 7.1.: Valence bond schemes of TAPP and its fluorinated alkyne chain substituted derivatives.

7.1. Tetraazaperopyrene: A promising n-type Organic Semiconductor

The introduction of nitrogen atoms into the π -backbone of aromatic organic semiconductors, as already mentioned for the family of the acenes in section 6.4, stabilizes the frontier orbitals energetically and increases the electron affinity and thus can change the molecules from p-type to n-type organic semiconductors. N-heteropolycycles are therefore promising candidates for organic semiconductor based devices and have received increasing attention over the past years [90, 94, 246–251, 267, 268]. A relative new class N-heteropolycyclic molecules are the TAPPs, which already have shown promising results, as on the one hand fluorescence markers and on the other hand organic semiconductors [96–100]. The material properties, photophysics, and redox chemistry can be widely tuned by modification, complexation and core substitutions [38, 99, 101–106]. Thermal stability up to 400 °C [103], allows vacuum deposition *via* evaporation, as was used to investigate films deposited on Cu(111) and Au(111) surfaces [105, 269–273]. For TAPP on Cu(111) well-ordered films were created in the first place. Since the copper surface is much more reactive than the noble gold surface different adsorbate structures could be obtained *via* temperature control. With increasing temperature the adsorbate structure evolves from a close-packed assembly similar to a projection of the bulk structure, over a porous copper-TAPP surface coordination network, to covalently linked molecular chains [269]. On the Au(111) surface TAPP shows a surface-induced strictly planar growth for monolayer as well as for multilayer

7.1. Tetraazaperopyrene: A promising n-type Organic Semiconductor

coverages (up to 10 ML) [273]. The π -conjugated backbone interacts with the gold surface leading to flat lying molecules. For higher coverages, the film then seems to continue growing with the same molecular orientation with respect to the Au(111) plane. By introducing bulky side chains as in the case of TAPP-(C₃F₇)₂ this planar structure is only obtained for the monolayer. In the multilayer the molecules are tilted around the short axis, but still well-ordered [105]. Recent atomic force microscopy (AFM) and STM investigations reveal the detailed surface structure of TAPP and TAPP-(CF₃)₂ adsorbed on Au(111).¹ Figure 7.2 shows the obtained STM (a-c) and AFM (d) images for TAPP-(CF₃)₂. The at room temperature deposited molecules arrange in large self-assembled island, while the underlying herringbone reconstruction of the Au(111) surface is still observable, which is a hind for a weak molecule-metal interaction. The high resolution STM images in figure 7.2 (b) and (c) and the Laplace-filtered constant height AFM image show the parallel alignment of the molecules, where the molecules of adjacent rows are shifted to each other in a way that the nitrogen atoms of adjacent molecules form a row perpendicular to the long axis of the molecules.

¹Unpublished data measured by Daniela Rolf in the group of Katharina J. Franke at the Freie Universität Berlin.

7. Band Formation at the Metal/Organic Interface

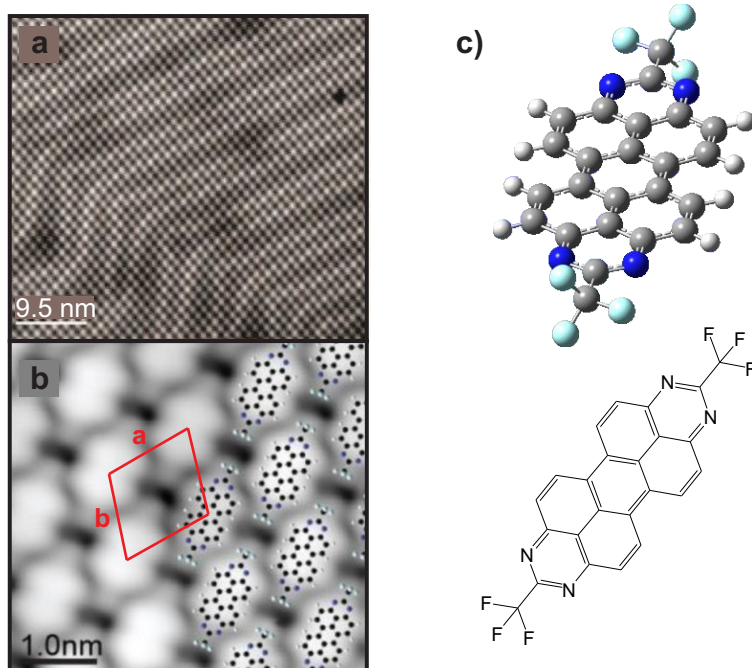


Figure 7.2.: (a) Overview STM image of TAPP-(CF₃)₂ adsorbed on Au(111) showing the underlying herringbone reconstruction of the gold surface. Topography recorded at $I = 220 \text{ pA}$, $V = 300 \text{ mV}$. (b) Close-up view of the molecular structure. The red lines show the unit cell of the structure with $a = 1.25 \text{ nm}$ and $b = 1.20 \text{ nm}$. Topography recorded at $I = 200 \text{ pA}$, $V = -300 \text{ mV}$. (c) Valence bond scheme and structure model of TAPP-(CF₃)₂.¹

7.2. Sample Preparation and Coverage Estimation of Tetraazaperopyrene on Au(111)

TAPP, TAPP-(CF₃)₂ and TAPP-(C₃F₇)₂ were evaporated onto a cleaned gold surface (refer to section 3.3.1) by heating the effusion cell to 523 K, 528 K, and 540 K, respectively.² The sample temperature was held at 300 K. Figure 7.3 shows EI-MS spectra of TAPP and TAPP-(CF₃)₂ with the most important fragmentations displayed. The TAPP fragmentation channel is dominated by HCN splitting. All resulting fragments form doubly charged ions, which have mass to charge ratios below $m/z = 200$ and therefore are within the detection range of the QMS attached to the UHV chamber used in the framework of this thesis. For TAPP-(CF₃)₂ the observed fragmentations get much more diverse, as the -CF₃ groups can split off easily, followed by CN or HCN cleavages. Besides the CF₃ fragment with $m/z = 69$, doubly charged ions of different fragments again dominate the detectable region of the QMS. For the sake of completeness the EI-MS spectrum of TAPP-(C₃F₇)₂ is displayed in appendix D.6 (a) showing the fragmentation of the C₃F₇ groups and again the formation of doubly charged ions. The coverages of the investigated molecules on top of the Au(111) surface were determined by TPD measurements by comparing the relative peak intensities of the multilayer and the monolayer peak as shown in figure 7.4 and D.6 (b). The figures display TPD spectra of different initial coverages of the TAPP and its derivatives adsorbed on Au(111) recorded with $m/z = 111$ for TAPP, and $m/z = 69$ for TAPP-(CF₃)₂ and TAPP-(C₃F₇)₂. For all three molecules a zero-order shaped multilayer peak (α_1) is observed between 400 – 470 K, while the contributions (α_1) at higher temperatures assigned to the monolayer differ in shape. For the bare TAPP the broad monolayer contribution is located around 600 K, while for the TAPP-(CF₃)₂ derivative it is more narrow and located around 640 K. For the TAPP-(C₃F₇)₂ derivative (appendix D.6 (b)) the formation of an compressed phase is predicted as an additional monolayer peak is obtained in the spectrum [69, 222, 252–257]. The desorption peaks of the TAPP-(CF₃)₂ are shifted around 40 K to higher temperatures, compared to the other two derivatives, leading to the assumption that it seems to be slightly stronger bound. The insets in figure 7.4 show TPD spectra for additional m/z ratios at a coverage of seven and four MLs, respectively. All fragments are detected at

²All data regarding TAPP-(C₃F₇)₂ were acquired by Dr. David Gerbert and Alexander Broska in the group of Petra Tegeder at the University of Heidelberg and were partly reevaluated by the author (also refer to Ref. [274].)

7. Band Formation at the Metal/Organic Interface

the same desorption temperature in the multi- as well as in the monolayer giving a clear hind for an intact desorption of the molecules. This is underpinned by the comparable relative intensity ratios between multi- and monolayer peak for all fragments. The intact desorption of the molecules on the one hand is a further hind for relative weak substrate-adsorbate interactions and on the other hand permits the preparation of well-defined monolayers by adsorbing a multilayer coverage and subsequent flashing the sample to 430 K and 470 K, respectively.

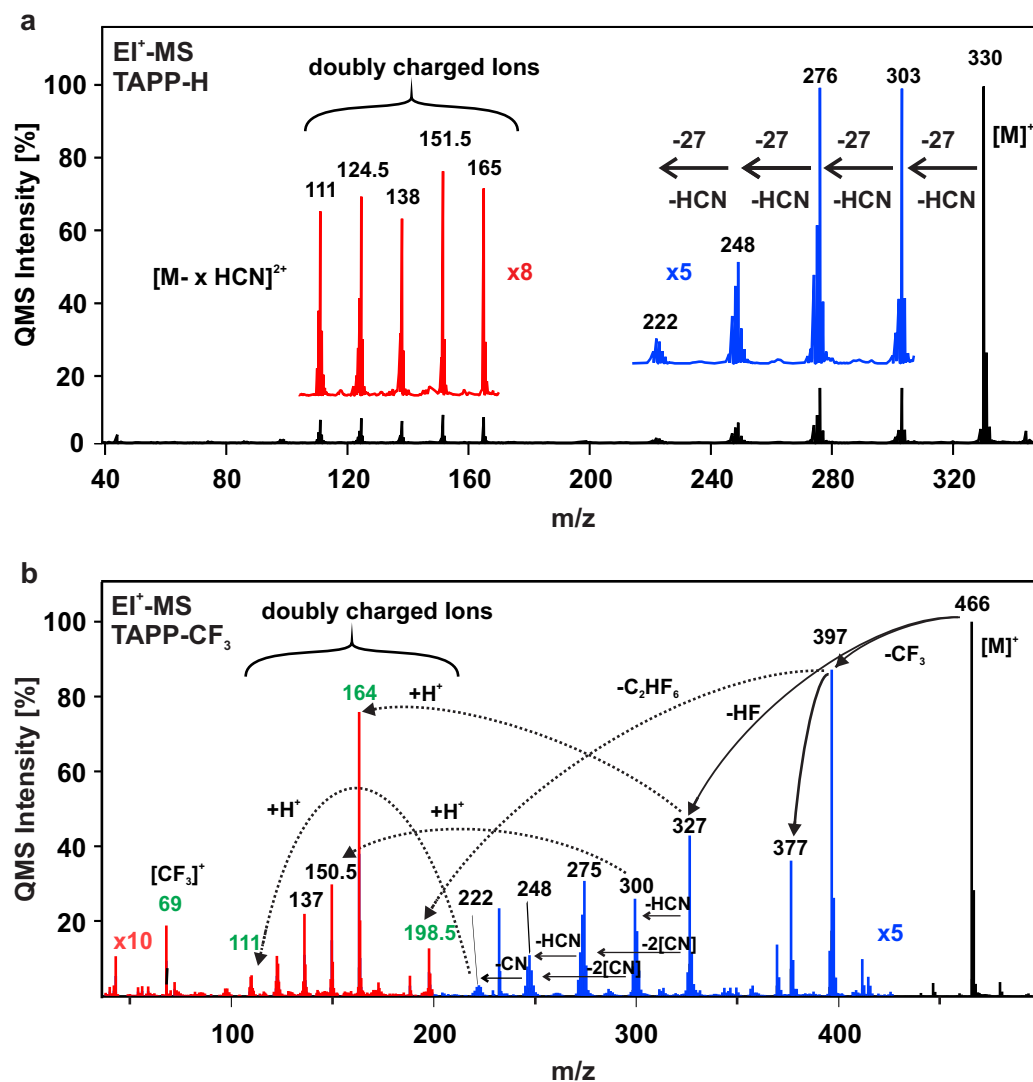


Figure 7.3.: EI-MS spectra of TAPP and TAPP-(CF₃)₂. The part of the spectrum observable by the QMS attached to the UHV chamber is shown enlarged. Important fragmentation steps are labeled.

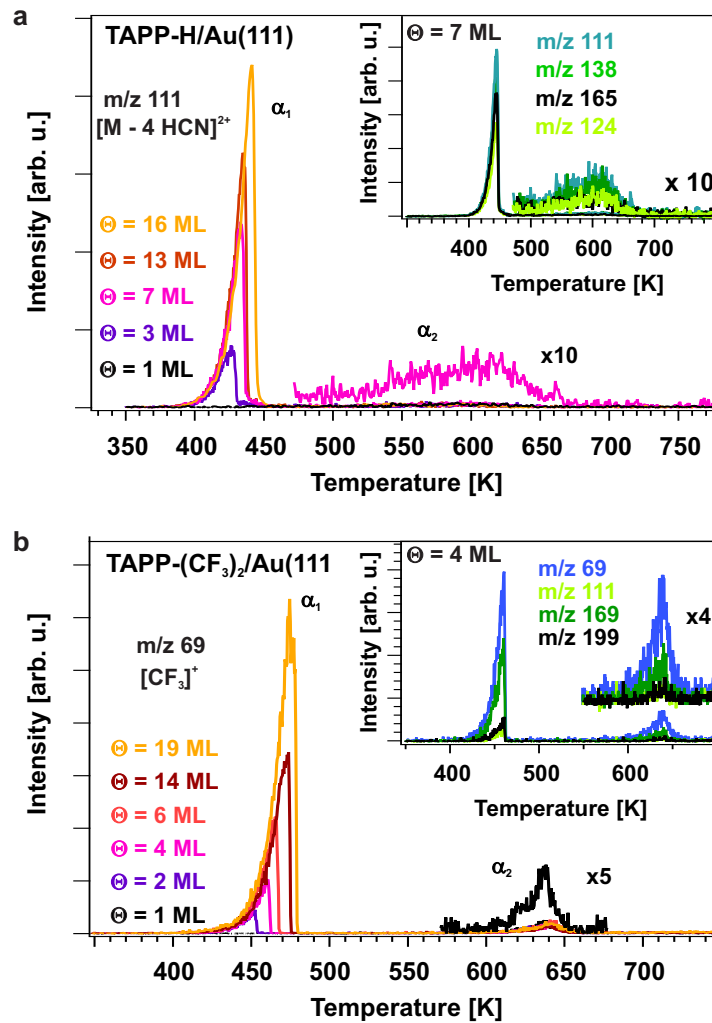


Figure 7.4.: TPD measurements of TAPP (ionic fragment $m/z = 111$) and TAPP-(CF₃)₂ (ionic fragment $m/z = 69$) adsorbed on Au(111) for different initial coverages recorded with a heating rate of 1 K/s. α_1 denotes the multilayer and α_2 the monolayer desorption peak. The inset shows equivalent measurements for different mass charge ratios at a coverage of 4 and 7 ML, respectively.

7.3. Electronic Structure of the Tetraazaperopyren/Au(111) Interface

To shed light onto the electronic structure at the interface between the TAPPs and the Au(111) surface 2PPE measurements have been carried out. Selected spectra obtained at the TAPP-(CF₃)₂/Au(111) interface (monolayer coverage) are displayed in figure 7.5. For a full set of spectra taken with several photon energies and at various coverages for all TAPP derivatives refer to appendix D. Figure 7.5 (a) shows monochromatic measurements with a photon energy of $h\nu = 4.2 \text{ eV}$ and $h\nu = 4.5 \text{ eV}$ while Figure 7.5 (c) shows dichromatic measurements with a photon energy of $h\nu_1 = 4.19 \text{ eV}$ and $h\nu_2 = 2.09 \text{ eV}$. Figure 7.5 (b) and (d) show the corresponding photon energy dependent peak positions, to assign the peaks to initial, intermediate or final states. The spectra are fitted by an exponential background and Gaussian-shaped peaks for clarity. Besides the well-known *d*-band features three initial states, five intermediate states, and two final states, with their energy in respect to E_{Fermi} being $E_{SS} = -0.29 \pm 0.08 \text{ eV}$, $E_{HOMO} = -1.73 \pm 0.06 \text{ eV}$, $E_{OIHB} = -2.53 \pm 0.06 \text{ eV}$, $E_{LUMO} = 1.40 \pm 0.08 \text{ eV}$, $E_{UMO_1} = 1.51 \pm 0.10 \text{ eV}$, $E_{UMO_3} = 3.19 \pm 0.05 \text{ eV}$, $E_{UMO_4} = 3.80 \pm 0.09 \text{ eV}$, $E_{IPS_{n=1}} = 4.40 \pm 0.07 \text{ eV}$, $E_{UIHB} = 5.48 \pm 0.06 \text{ eV}$, and $E_{UMO_5} = 5.65 \pm 0.06 \text{ eV}$ are revealed. The shifted SS' is assigned *via* its energetic position which is in good agreement with shifted SSs' for other molecule covered surfaces (refer to section 5.3, 6.3, 6.6 and Refs. [128–131]) and the observed dispersion. The energetically highest located molecule-induced state is associated with the HOMO getting underpinned by the coverage series shown in appendix D.2 (c), as the onset of the spectra obtained for high coverages is found to match the HOMOs peak position. The third peak showing a slope of two originates from an occupied interface hybrid band (OIHB) as will be discussed in more detail in section 7.4. The observed intermediate state related peaks origin from several UMOs and the first IPS, where UMO_{3–4} are found in the monochromatic spectra and UMO₁ is found in the dichromatic spectra. The peak assigned to the LUMO is only obtained for high photon energies, as the peak merges with the *d*-band features for lower photon energies and therefore the assignment *via* photon energy dependent measurements can only be estimated. However, the peak positions fit well to the LUMO position obtained more clearly for the bare TAPP as determined in appendix D.5, underpinning this assignment. Close to the secondary edge two peaks without a photon energy dependence are observed. The energetically higher lying peak is assigned on to an UMO located above the global work function (UMO₅) of the sample, while the lower lying peak origins from an unoccupied interface hybrid band (UIHB) (refer to section 7.4). Excitations

into these states can be viewed as resonant scattering events from photoexcited electrons being bound shortly in molecular or interface states above E_{vac} , followed by detachment and detection. The work function of the sample shifts downwards with increasing coverage of TAPP-(CF₃)₂, as can be seen from the coverage dependent measurements in the appendix (figure D.1 (c),(d) and D.2 (a),(c)). A strong decrease of the WF about 400 meV ($\Theta = 5.1 \pm 0.05$ eV), during the deposition of the first layer, is followed by a slower further decrease resulting in a work function of $\Theta = 5.0 \pm 0.05$ eV for around 20 ML. Interestingly the first IPS, which is actually pinned to the vacuum level and thus to the work function, shifts in the opposite direction for coverages exceeding 0.5 ML, as shown in figure D.2 (b). This behavior can be explained by a molecule-induced quantum defect increasing from $a \approx 0$ to $a \approx 0.2$ calculated *via* equation 2.1.8 (see figure D.2 (d)). The quantum defect a corrects the energy eigenvalues of the IPS for non-ideal surfaces (refer to section 2.1.1 for details.)

Equivalent measurements can be found in figure D.4 and D.5 for the TAPP/Au(111) interface, and in figure D.7 for the TAPP-(C₃F₇)₂/Au(111) interface. The overall electronic structure of all three interfaces at a monolayer coverage is found in figure 7.6. The shifted SS', the HOMO, and the occupied interfacial hybrid band are observed for all three metal/organic interfaces at the same energy leading to the conclusion, that the HOMO as well as the OMO forming the OIHB are located at the molecular backbone. This is also valid for the LUMO and UMO₁, even if both of them could not be approved within the TAPP-(C₃F₇)₂ measurements. The UMO₂ is only observed for the bare TAPP, the UMO₃ only for TAPP-(CF₃)₂, and the UMO₄ for TAPP-(CF₃)₂ and TAPP-(C₃F₇)₂. The peaks originating from these electronic states might be overimposed by neighboring peaks and *d*-band features in spectra were they could not be observed. The work function for the different interfaces ranges from $\Theta = 5.17 \pm 0.05$ eV for the TAPP-(C₃F₇)₂ to $\Theta = 4.50 \pm 0.05$ eV for the bare TAPP. This can be explained by a reduced push-back effect, as the bulkier side chains reduce the amount of molecules per area on the surface. With the LUMO located at 1.40 eV and the HOMO found at -1.73 eV in respect to E_{Fermi} a gap of around 3.1 eV is found. In contrast, the optical gap determined for TAPP and TAPP-(C₃F₇)₂ by HREELS at the interface [273] and UV/Vis in solution [105, 273] is only 2.85 eV. This leads to the assumption, that the transport LUMO was observed *via* 2PPE and an exciton binding energy of 250 meV is concluded. The energetic position of the HOMO and the LUMO being located far above and far below E_{Fermi} , additionally excludes a charge transfer at the interface.

7. Band Formation at the Metal/Organic Interface

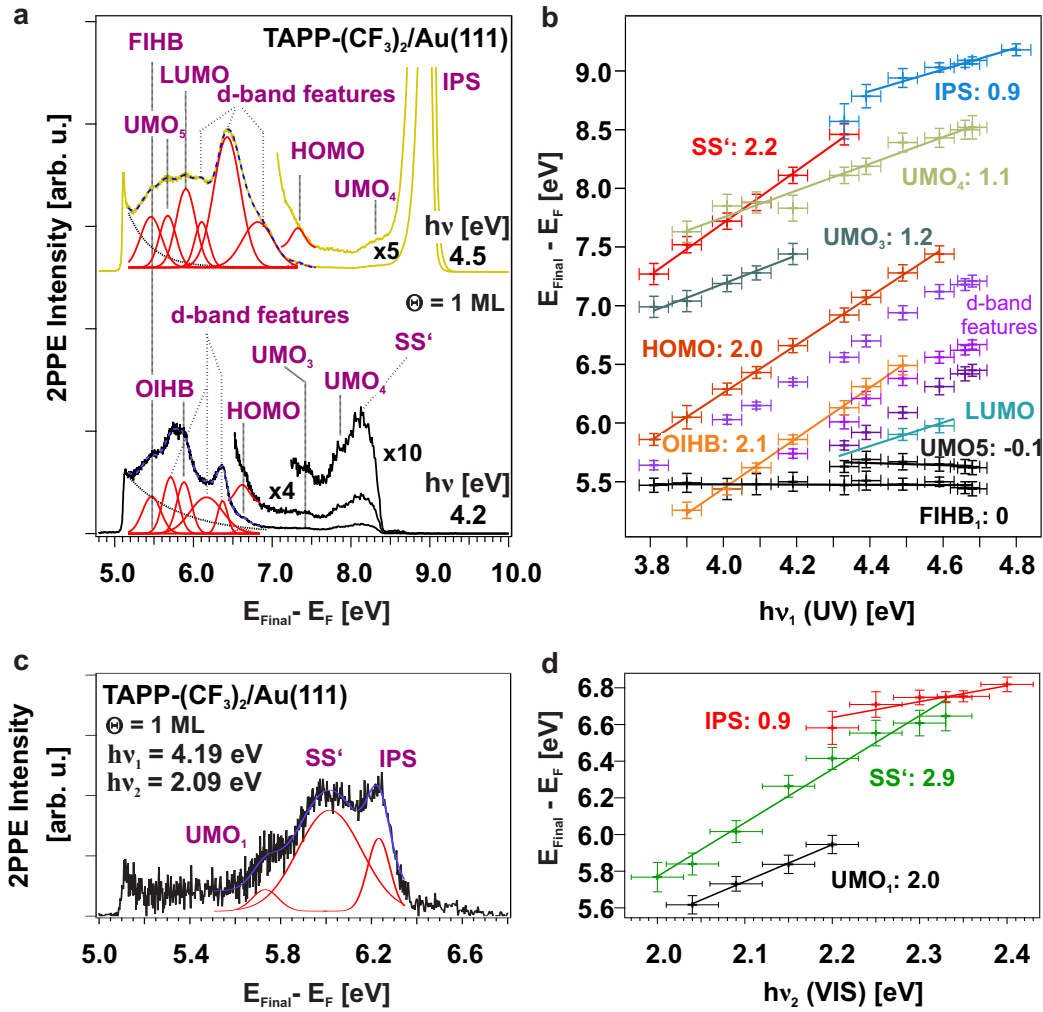


Figure 7.5.: (a) Monochromatic and (c) dichromatic 2PPE spectra of TAPP-(CF₃)₂ adsorbed on Au(111), recorded with different photon energies. 2PPE intensity is given as a function of the final state energy. The data is fitted by an exponential background and Gaussian-shaped peaks. Peaks resulting from (the highest) occupied molecular orbitals ((H)OMO), (the lowest) unoccupied molecular orbitals ((L)UMO), the shifted surface state (SS') and the first image potential state (IPS) are observed. Additionally, an unoccupied and an occupied interface hybrid band (UIHB, OIHB) are detected. (c) and (d) show the corresponding photon energy dependent peak positions to assign peaks observed in the 2PPE spectrum.

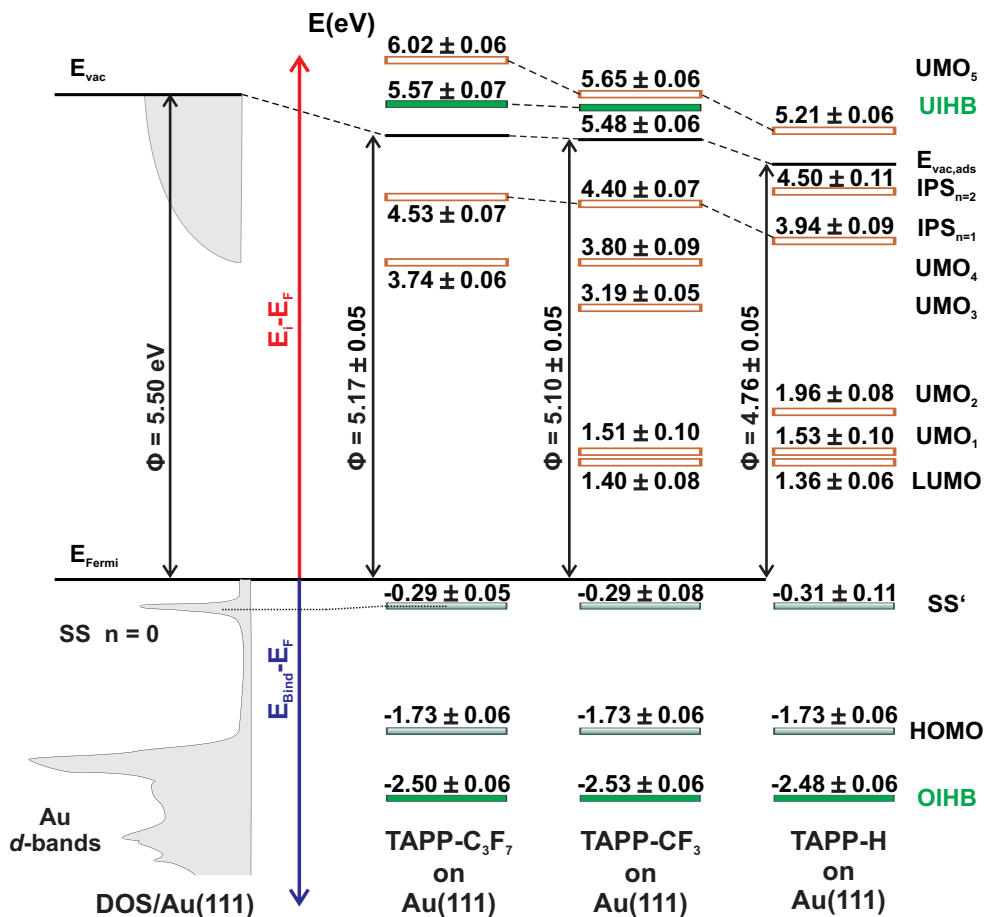


Figure 7.6.: Energy level diagrams of different TAPP derivatives adsorbed on Au(111). On the left the density of states (DOS) of the bare gold surface is shown. Unoccupied electronic states are shown in red, while occupied electronic states are shown in blue. The formed interface hybrid bands are marked green. Molecule dependent state and work function shifts are highlighted by dashed lines. The energetic positions are given in respect to the Au(111) Fermi level (E_F).

7.4. Dispersions in Molecule-Induced States

During the presentation of the electronic structure at the interfaces of the investigated TAPP derivatives on Au(111) in the previous section, an initial and a final state have been assigned to an occupied and an unoccupied interface hybrid band, respectively. This assignment is based on AR-2PPE measurements, which shall be discussed in the following section. In chapter 2 a basic introduction into band formation in metals and molecules, and the formation of interface hybrid states is given. It was concluded that dispersions of electrons are the direct consequence of “nearly free moving electrons” in a periodic lattice potential, as it is e.g. the case within an electronic band. Vice versa it follows that the observation of dispersing electronic states is a clear evidence for band formation.

Figure 7.7 shows AR-2PPE spectra for the different investigated TAPP-derivative/Au(111) interfaces. For TAPP-(CF₃)₂ (figure 7.7 (a)) two molecule-induced peaks observed in the spectrum clearly show a dispersion and therefore can be assigned to interface hybrid bands. It should be pointed out, that the *d*-band features of the gold substrate show no dispersion in the measured *k*-space, as it already was discussed in chapter 4. From photon energy dependent measurements (section 7.3) it is known that the OIHB is energetically located at $E_{OIHB} = -2.53 \pm 0.06 \text{ eV}$ in the region of the Au(111) *d*-band [147, 275]. The OIHB therefore most likely is formed *via* a hybridization of the HOMO-1 ($\Delta E_{HOMO,HOMO-1} = 0.82 \text{ eV}$)³ of the TAPP-(CF₃)₂ and the gold *d*-band. In contrast, the UIHB is located within the energetic region of the unoccupied *sp*-band of the gold substrate [147] and thus a hybridization between this band and an energetically high lying UMO can be concluded. It should be pointed out, that an intermolecular band formation is excluded because all TAPP derivatives are lying flat on the surface as has been shown *via* STM, AFM and HREELS measurements (see section 7.1 and Refs. [105, 273]), which denies any intermolecular $\pi - \pi$ interactions. Dispersion measurements at the TAPP/Au(111) interface also reveal the formation of the OIHB (figure 7.7 (b)), while for the TAPP-(C₃F₇)₂ interface an even more complex situation is found. The OIHB dispersion can also be clearly observed, but the unique positions of the peak can only be roughly estimated as the peak is merged into one broad contribution with the close by *d*-band feature. Besides the strong dispersing UIHB two further dispersing contributions (labeled *A* and *B*) are revealed, which seem to be

³Value obtained from DFT calculations (B3LYP/6-311G) carried out by Dr. Friedrich Maaß in the group of Petra Tegerder at the University of Heidelberg

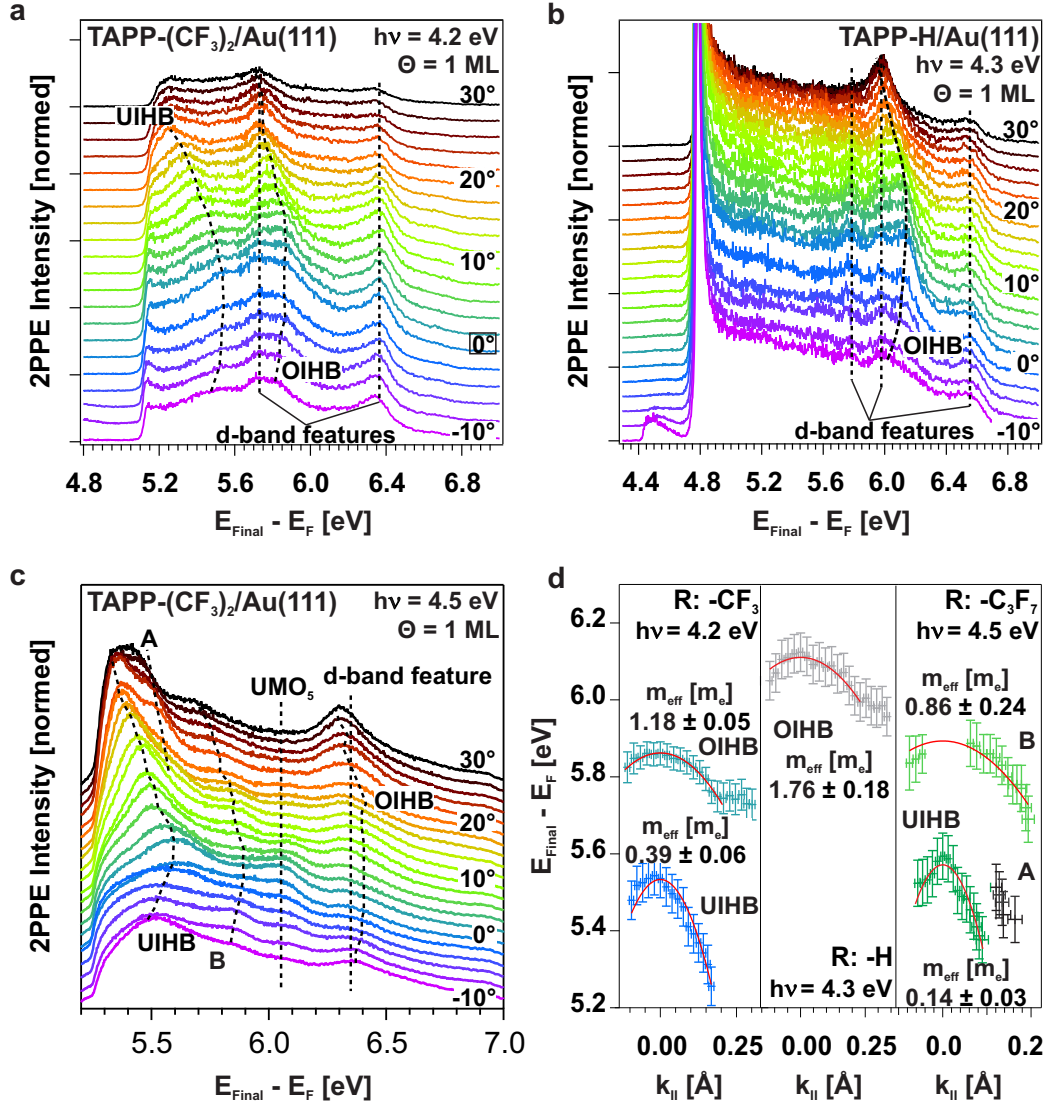


Figure 7.7.: (a-c) AR-2PPE measurements of different TAPP derivatives adsorbed on Au(111). Electronic states and interface bands are highlighted by dashed lines. (d) shows the observed peak positions in respect to k_{\parallel} .

7. Band Formation at the Metal/Organic Interface

superimposed by other contributions of the spectrum in normal emission mode. A clear assignment to an unoccupied or occupied interface hybrid band therefore is challenging, as no photon energy dependent measurements could be carried out for these peaks, but anyway they both underpin dispersion and band formation at the interface. Figure 7.7 (d) shows k_{\parallel} -dependent peak positions of all interfaces and calculated effective masses (see equation 3.2.4). For the OIHB relative weak dispersion, accompanied with a high effective mass (OIHB: $m_{eff,-CF_3} = 1.18 \pm 0.05 m_e$ and $m_{eff,-H} = 1.76 \pm 0.18 m_e$), are obtained, while for the UIHB much stronger dispersion (UIHB: $m_{eff,-CF_3} = 0.39 \pm 0.06 m_e$ and $m_{eff,-C_3F_7} = 0.14 \pm 0.03 m_e$) are observed. The strength of the dispersions confirm the band formation *via* hybridization of the HOMO-1 and the d -band as well as *via* hybridization of a higher lying UMO and the sp -band. Since the d -bands are rather localized around $k_{\parallel} = 0$ a rather weak dispersion of the OIHB is expected, while a strong dispersion is expected for a hybridization with the strong delocalized sp -bands, as it is the case for the UIHB. From this argumentation it can be proposed that the observed band labeled with B ($m_{eff,B} = 0.86 \pm 0.24 m_e$) is more likely an occupied band than an unoccupied band.

Within this chapter the electronic structures of the TAPP/Au(111), TAPP-(CF₃)₂/Au(111) and TAPP-(C₃F₇)₂/Au(111) interfaces have been presented. For this purpose the molecules were deposited on the gold surface *via* evaporation under UHV conditions leading to well-ordered adsorbate structures as proven by STM and HREELS measurements [105, 273]. It was shown, that an intact desorption of multi- and monolayer could be achieved *via* TPD measurements revealing a rather weak interaction and opening up the possibility for a clear coverage determination. By 2PPE measurements several interface and molecule-induced states, including the shifted SSs', IPSs, HOMOs, LUMOs and further higher lying UMOs, could be determined. Additionally, the formation of interface hybrid bands was observed by dispersion measurements. On the one hand, a hybridization of the gold d -band the molecular HOMO-1, and on the other hand of the unoccupied gold sp -band and a higher lying UMO was purposed. This band formation is sketched in figure 7.8 showing the surface arrangement of TAPP-(CF₃)₂ on Au(111) with the calculated⁴ spatial electron density distribution of the HOMO-1 added to the molecules. The electron density of the HOMO-1 for an isolated molecule is mainly located on the nitrogen atoms, which form chains perpendicular to the long molecule axis and therefore an ideal geometry for efficient band formation is given by the adsorption structure. This band

⁴DFT calculations (B3LYP/6-311G) carried out by Dr. Friedrich Maaß in the group of Petra Tegeder at the University of Heidelberg

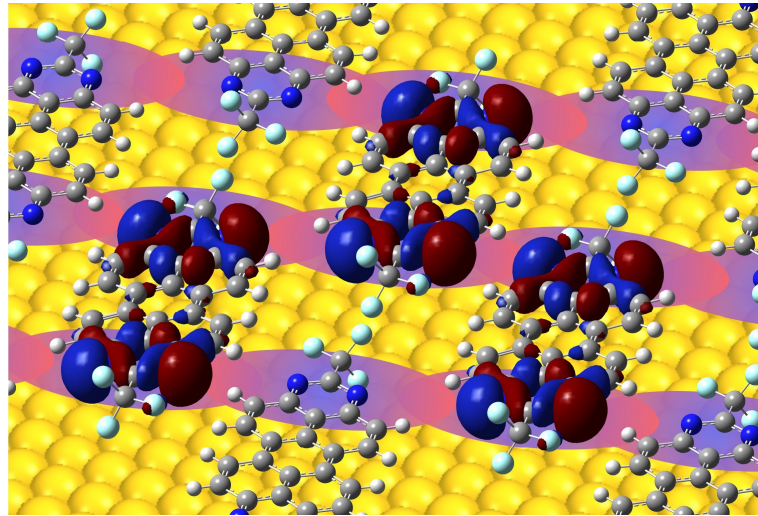


Figure 7.8.: Sketch of the band formation, illustrated by means of the example of the TAPP-(CF₃)₂/Au(111) interface.

formation due to hybridization of delocalized metal band and localized molecular orbitals at a weak interacting not charged interface, should foster efficient charge injection, and therefore TAPP is a promising candidate for applications in organic field effect transistors.

8. Conclusion and Outlook

The aim of the present thesis has been the investigation of fundamental aspects of the metal/organic interface and in thin adsorbate layers, since a detailed understanding is crucial for a systematical improvement of the performance of (opto-)electronic devices such as organic light emitting diodes (OLEDs), organic field effect transistors (OFETs), and organic solar cells (OSCs). The thesis has focused on the electronic properties of promising N-heteropolycyclic molecules. Overall three main aspects, the electronic structure i.e. the energetic position of unoccupied and occupied electronic states, excited state dynamics and band formation have been addressed. Two-photon photoemission spectroscopy (2PPE) is a powerful tool capable to access both occupied as well as unoccupied electronic states at surfaces. The assignment of occupied electronic states could be confirmed by ultraviolet photoelectron spectroscopy (UPS), while the information gained *via* temperature-programmed desorption (TPD) has helped to determine coverages and ensured reproducible sample preparations, especially for measurements at well-defined monolayers.

The first topic of this thesis has been the examination of the 10,17-bis((triisopropylsilyl)ethynyl)-pentacene (TIPS-Pn)/Au(111) interface. The multilayer desorbs intact from the surface during heating, and thus, well-defined monolayers could be achieved by heating the sample to a certain temperature after multilayer deposition. TPD additionally enabled coverage determinations for multilayer samples. The electronic structure at the interface has been determined by 2PPE and UPS, revealing several interface and molecule induced states. Besides the shifted Shockley surface state (SS)', and the first and second image potential state, the highest occupied molecular orbital (HOMO), the optical lowest unoccupied molecular orbital (LUMO) (S_1) and further higher and lower lying molecular states have been observed. Examining the excited state dynamics at the TIPS-Pn/Au(111) interface with femtosecond (fs) time-resolved 2PPE (TR-2PPE), singlet fission could be resolved. The dynamics are strongly influenced by the underlying gold substrate as the observed lifetimes are coverage dependent. The lifetimes decrease strongly for decreasing layer thickness, which can be explained by

8. Conclusion and Outlook

the availability of two relaxation channels, on the one hand, an intrinsic bulk material decay channel and, on the other hand, a distance dependent external decay channel, in which the excited states get quenched by the metal substrate. For films in which the influence of the gold surface gets negligible, a coherent excitation of the S_1 and the multiexciton (ME) state followed by a contemporaneous decay with a lifetime of 160 ± 60 fs into hot triplet states have been concluded. A subsequent “intra-band” stabilization of the resulting triplet states has been achieved on a timescale of 1.6 ± 0.9 ps. The final decay of the stabilized triplet into the ground state then occurs within 620 ± 190 ps. Since TIPS-Pn is a promising candidate for applications in organic semiconductor based solar cells, the electronic structure at the interface between the metal (electrode) and the organic molecule is of great importance. The gained results help to understand the underlying photophysics in singlet fission based solar cells and might support the development of future organic semiconductor based photovoltaics.

Within the second topic of this thesis, several N-heteropolycycle/Au(111) interfaces have been investigated. Namely, these are Fe-5,10,15,20-tetra-pyridilporphyrin (FeTPyP), 10,17-bis((triisopropylsilyl)ethynyl)dibenzo[a,c]naphtho[2,3-i]phenazinen (TIPS-BAP), 1,3,8,10-tetraazaperopyrene (TAPP), 2,9-bis(trifluoromethyl)-1,3,8,10-tetraazaperopyrene (TAPP-(CF₃)₂), and 2,9-bis(perfluoropropyl)-1,3,8,10-tetraazaperopyrene (TAPP-(C₃F₇)₂).

FeTPyP is a molecule from the class of the porphyrins, which stand out due to their flexibility, tunability, and versatility. The molecule consists of the porphine core with four pyridil substituents connected in *meso* position, an incorporated Fe(III) ion and a Cl⁻ counterion. UPS and 2PPE measurements have revealed the electronic structure at the interface, containing the shifted SS', the first IPS and several molecule-induced states. The energetic position of the HOMO, LUMO (transport and affinity levels) and further higher and lower lying molecular states have been received. The transport gap has been determined to be 2.2 eV. Additionally, the energetic position of an excitonic state, where the LUMO is populated by an intramolecular excitation, has been obtained. The resulting optical gap is 1.78 eV, and therefore, an exciton binding energy of 420 meV has been concluded.

TIPS-BAP is an arrow-shaped acene like molecule with two incorporated nitrogens. It has been shown that a successful sample preparation *via* evaporation is possible. TPD measurements have led to the conclusion that molecules adsorbed in the multilayer could be desorbed intact from the surface, in contrast to molecules adsorbed in the monolayer. The energetic positions of several molecular states and the shifted SS' have been determined. From the energetic positions of the HOMO and the LUMO

(exciton), the optical gap has been calculated to be 1.74 eV at a coverage of 1 ML TIPS-BAP adsorbed on Au(111).

A further group of N-heterocycles are the TAPPs. In the presented work, the bare TAPP and two derivatives with fluorinated alkyl chains adsorbed on the Au(111) surface have been investigated. A rather weak interaction between the molecules and the gold substrate has been derived, as TPD measurements showed an intact desorption of multi- and monolayer during heating of the sample. This has enabled a clear coverage determination for the investigated samples. The energetic positions of the determined frontier orbitals are nearly unaffected by the fluorinated alkyl side chains. The same is true for the shifted SS', and most of the observed higher and lower lying molecular states. In contrast, the shift of the work function resulting from the adsorption of a monolayer of the different molecules differs strongly. This has been attributed to a varying push-back effect as a consequence of a molecule dependent density of packing on the surface. The lowest observed unoccupied molecular orbital has been assigned to an affinity level with a resulting transport gap of 3.1 eV. From the comparison with HREELS and UV/Vis measurements, an exciton binding energy for on Au(111) adsorbed TAPPs of around 250 meV has been concluded. From the energetic positions of the frontier orbitals with respect to E_{Fermi} of the gold substrate, a charge transfer at the interface has most likely been excluded.

The determination of electronic structures of high potential organic semiconductors at the metal (electrode) interface is crucial for applications, since it dominantly influences the necessary charge carrier injection between the materials. Charge injection can additionally be fostered by hybrid band formation between metal bands and molecular orbitals. A consequence of band formation is the free charge carrier movement in the band, resulting in dispersions of the charges. The third topic of this thesis has treated the observation of band formation at the interface between the TAPP derivatives and the gold surface *via* AR-2PPE. These bands have proposed to be formed by a hybridization between the HOMO-1 and gold *d*-bands, and an energetically high lying UMO and the unoccupied gold *sp*-band. A relative strong dispersion with an effective mass (m_{eff}) between 0.1-0.4 m_e has been observed for the unoccupied interface hybrid band, while the dispersion observed for the occupied interface hybrid band has shown an m_{eff} between 1.2-1.8 m_e . This kind of band formation at the metal/organic interface has so far only been predicted for systems showing an initial charge transfer, e.g. the F₄TCNQ/Au(111) and TTF/Au(111) interface. Therefore, the band formation obtained for the TAPP/Au(111) interfaces stands out and should support efficient charge injection from the metal electrode into the organic material and *vice versa*.

8. Conclusion and Outlook

In summary, this work has contributed to a better understanding of the electronic structure and excited state dynamics at metal/organic interfaces. The achieved experimental result may give feedback to synthesize further tailored organic semiconductors and give basic information to develop more efficient and customized organic molecule based applications.

Future investigations should address in how far the band formation at the interface can lead to an increased performance of devices. A systematic investigation of further N-heteropolycycles should be carried out as being aspired within the scope of the collaborative research center *SFB1249*. Finally, this should help to identify key construction principles to tune molecular properties for individual needs and expand the amount of possible building blocks for organic electronics.

List of Figures

2.1.	Electron dispersion and band formation in a periodic potential .	14
2.2.	Theoretical Description of Shockley surface states and image potential states	16
2.3.	Electronic band structure of an Au(111) surface	19
2.4.	Illustration of the linear combination of the molecular orbitals of ethylen	21
2.5.	Illustration of the exciton binding energy	23
2.6.	Illustration of the induced density of interfacial states model . .	24
2.7.	Illustration of the molecule/metal hybrid state formation	25
2.8.	Simplified illustration of the frontier orbitals during the singlet fission process	27
3.1.	Schematic illustration of temperature programmed desorption measurements	30
3.2.	Sketch of a typical 2PPE spectrum	33
3.3.	Sketch of the 2PPE peak assignment	34
3.4.	AR-PES conditions	35
3.5.	Sketch of the UHV chamber	37
3.6.	Sketch of the laser setup	38
3.7.	Illustration of the beam characteristics	39
4.1.	PES on the bare gold surface	42
4.2.	AR-2PPE on the bare gold surface	43
5.1.	TIPS-Pn adsorbed on Au(111): EI-MS spectrum	47
5.2.	TIPS-Pn adsorbed on Au(111): TPD measurements	48
5.3.	TIPS-Pn adsorbed on Au(111): 2PPE measurements	50
5.4.	TIPS-Pn adsorbed on Au(111): Energy level diagram	52
5.5.	TIPS-Pn adsorbed on Au(111): TR measurements	53
5.6.	TIPS-Pn adsorbed on Au(111): Excited state dynamics	55
6.1.	FeTPyP adsorbed on Au(111): STM images	59
6.2.	FeTPyP adsorbed on Au(111): dI/dV spectrum	60
6.3.	FeTPyP adsorbed on Au(111): EI-MS	61

List of Figures

6.4.	FeTPyP adsorbed on Au(111): TPD measurements	62
6.5.	FeTPyP adsorbed on Au(111): UPS spectra	64
6.6.	FeTPyP adsorbed on Au(111): 2PPE measurements at 1 ML	66
6.7.	FeTPyP adsorbed on Au(111): Submonolayer measurement	67
6.8.	FeTPyP adsorbed on Au(111): Energy level diagram	69
6.9.	TIPS-BAP adsorbed on Au(111): Valence bond scheme and crystal packing	70
6.10.	TIPS-BAP adsorbed on Au(111): EI-MS spectrum	72
6.11.	TIPS-BAP adsorbed on Au(111): TPD measurements	73
6.12.	TIPS-BAP adsorbed on Au(111): 2PPE measurements	75
6.13.	TIPS-BAP adsorbed on Au(111): Energy level diagram	77
7.1.	TAPPs molecules	80
7.2.	TAPPs adsorbed on Au(111): STM images	82
7.3.	TAPPs adsorbed on Au(111): EI-MS spectra	84
7.4.	TAPPs adsorbed on Au(111): TPD measurements	85
7.5.	TAPP-(CF ₃) ₂ adsorbed on Au(111): 2PPE measurements	88
7.6.	TAPPs adsorbed on Au(111): Energy level diagrams	89
7.7.	TAPPs adsorbed on Au(111): AR-2PPE measurements	91
7.8.	TAPPs adsorbed on Au(111): Bandformation	93
A.1.	TIPS-Pn adsorbed on Au(111): Additional 2PPE and UPS mea- surements	109
A.2.	TIPS-Pn adsorbed on Au(111): Coverage series.	110
A.3.	TIPS-Pn adsorbed on Au(111): AR-2PPE measurements	110
B.1.	FeTPyP adsorbed on Au(111): Illumination series	112
B.2.	FeTPyP adsorbed on Au(111): Submonolayer measurements	112
B.3.	FeTPyP adsorbed on Au(111): Coverage series.	113
B.4.	FeTPyP adsorbed on Au(111): Submonolayer AR-2PPE	114
C.1.	TIPS-BAP adsorbed on Au(111): Illumination series	116
C.2.	TIPS-BAP adsorbed on Au(111): AR-2PPE and multilayer measurements.	117
D.1.	TAPP-(CF ₃) ₂ adsorbed on Au(111): Photon energy- and cov- erage series	119
D.2.	TAPP-(CF ₃) ₂ adsorbed on Au(111): Coverage series (IPS and WF shifts).	120
D.3.	TAPP-(CF ₃) ₂ adsorbed on Au(111): AR-2PPE measurements.	121
D.5.	TAPP adsorbed on Au(111): Fitted 2PPE spectra.	122
D.4.	TAPP adsorbed on Au(111): 2PPE measurements	123
D.6.	TAPP-(C ₃ F ₇) ₂ adsorbed on Au(111): EI-MS-Spectrum and TPD measurements	125

D.7. TAPP-(C₃F₇)₂ adsorbed on Au(111): 2PPE measurements . . . 126

List of Acronyms

1C-2PPE	monochromatic 2PPE
2C-2PPE	dichromatic 2PPE
2H-TPP	<i>meso</i> -tetraphenyl-porphyrin
2PPE	two-photon photoemission spectroscopy
AC	auto-correlation
AFM	atomic force microscopy
AO	atomic orbital
AR-2PPE	angle-resolved 2PPE
CNL	charge neutrality level
CT	charge transfer
DOS	density of states
E_F	Fermi energy
E_{vac}	vacuum energy
EI-MS	electron ionization mass spectroscopy
EA	electron affinity
fcc	face-centered cubic
FE	Fermi edge
FeTPyP	Fe-5,10,15,20-tetra-pyridil-porphyrin
FS	final state
FWHM	full width at half maximum
GIXD	grazing incidence X-ray diffraction
H ₂ TPyP	H ₂ -5,10,15,20-tetra(4-pyridyl)porphyrin

List of Acronyms

hcp	hexagonal closed packed
HOMO	highest occupied molecular orbital
HREELS	high resolution electron energy loss spectroscopy
IP	ionization potential
IPS	image potential state
IPS	inverse photoemission spectroscopy
LCAO	linear combination of atomic orbitals
LEED	low energy electron diffraction
LUMO	lowest unoccupied molecular orbital
Nd:YVO4	neodymium-doped yttrium orthovanadate
ME	multiexciton
ML	monolayer
MO	molecular orbital
NEXAFS	near edge X-ray absorption fine structure
OIHB	occupied interface hybrid band
OMO	occupied molecular orbital
OPA	optical parametric amplifier
OFET	organic field effect transistor
OLED	organic light emitting diode
OSC	organic solar cell
PES	photoemission spectroscopy
QMS	quadrupole mass spectrometer
SE	secondary edge
SF	singlet fission
SS	Shockley surface state
STM	scanning tunneling microscopy
STS	scanning tunneling spectroscopy

TA	transient absorption
TAPP	1,3,8,10-tetraazaperopyrene
TAPP-(CF₃)₂	2,9-bis(trifluoromethyl)-1,3,8,10-tetraazaperopyrene
TAPP-(C₃F₇)₂	2,9-bis(perfluoropropyl)-1,3,8,10-tetraazaperopyrene
TAPPor	tetra(4-aminophenyl)porphyrin
TIPS-BAP	10,17-bis((triisopropylsilyl)ethynyl)dibenzo[a,c]naphtho[2,3-i]phenazinen
TIPS-Pn	10,17-bis((triisopropylsilyl)ethynyl)-pentacene
TIPS	(triisopropylsilyl)ethynyl
TOF	time-of-flight spectrometer
TPD	temperature-programmed desorption
TR-2PPE	time-resolved 2PPE
UHV	ultra high vacuum
UIHB	unoccupied interface hybrid band
UMO	unoccupied molecular orbital
UPS	ultraviolet photoelectron spectroscopy
UV/Vis	ultraviolet-visible spectroscopy
WF	work function
XC	cross-correlation
XPS	x-ray photoelectron spectroscopy

Appendix

A. Additional TIPS-Pn Measurements

This section of the appendix covers all additional data that complements and underpins the interpretation and evaluation of chapter 5. Figure A.1 (a) shows the full series of monochromatic 2PPE spectra taken at the TIPS-Pn/Au(111) interface at a coverage of 1 ML. Spectra for several photon energies have been recorded to carry out the slope evaluation as shown in figure 5.3 (c). The low energy part of the spectra is mainly dominated by the secondary electron background and the *d*-band features of the underlying gold substrate. Molecule induced peaks only show weak contributions near the Fermi edge of the spectrum, as can be seen in the zoomed figure A.1 (b). Figure A.1 (b) displays the spectra of Figure A.1 (a) zoomed in a way, that the peaks with low intensity near the Fermi edge can be seen more clearly. The peak positions are highlighted by dashed lines. The peaks assigned to the HOMO and the UMO₂ are only observed for low photon energies. First due to a low cross section and latter due to an overlay by the *d*-band features for high photon energies. The peaks assigned to the UMO₁, and the first and second IPS are located directly at the secondary edge. The full series of dichromatic 2PPE spectra taken at the TIPS-Pn/Au(111) interface at a coverage of 1 ML is found in Figure A.1 (c). The observed peaks underpin the energetic positions of the UMO₁ and the two observed IPSs. Figure A.1 (d) shows coverage dependent UPS measurements at the TIPS-Pn/Au(111). The molecule induced shift and quenching of the SS is observed and the energetic position of the HOMO is underpinned. Coverage dependent 2PPE measurements at the TIPS-Pn/Au(111) are presented in figure A.2. Exceeding the monolayer coverage the spectrum gets more and more dominated by the peaks assigned to the HOMO and the optical LUMO (*S*₁-state), while the IPS gets quenched rapidly. The coverage dependent shift of the two dominating states can be seen and the secondary electron background increases strongly. The assignment of the two observed IPSs was based on AR-2PPE data obtained for 1 ML TIPS-Pn adsorbed on Au(111), as shown in figure A.3. The peak positions in respect to $k_{||}$ as well as the calculated

Appendix

effective masses (see equation 3.2.4) are displayed in the right graph. The obtained values fit to values obtained for other molecule covered metal surfaces (refer to section 2 and Refs. [138, 140]).

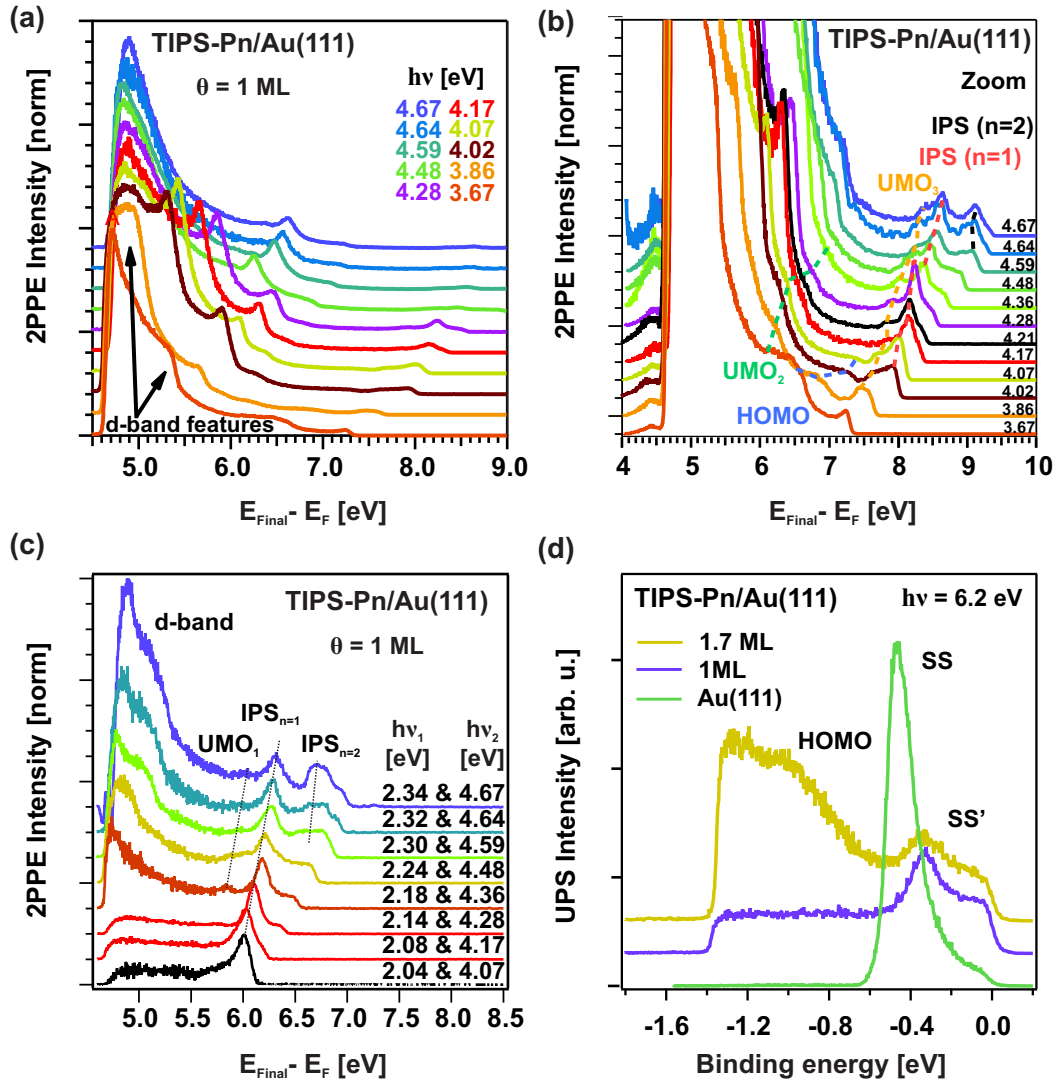


Figure A.1.: (a) & (b) Monochromatic and (c) dichromatic 2PPE spectra of 1 ML TIPS-Pn on Au(111) recorded with several photon energies. 2PPE intensity is given as a function of the final state energy. Refer to section 3.2 for additional information. UPS measurements ($h\nu = 6.2\text{eV}$) for different coverages of TIPS-Pn adsorbed on Au(111) are shown in (d). Dotted lines highlight peaks resulting from (the highest) occupied molecular orbitals ((H)OMO), unoccupied molecular orbitals (UMO), image potential states (IPS), and the (shifted) surface state ($SS^{(\prime)}$).

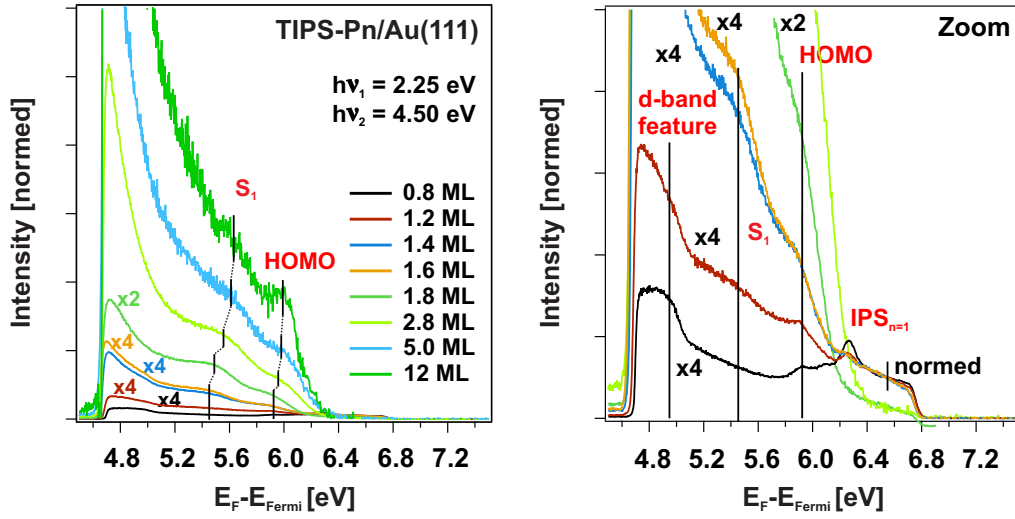


Figure A.2.: Left: 2PPE Spectra of different coverages of TIPS-Pn adsorbed on Au(111). The coverage dependent shift of the S_1 state and the highest occupied molecular orbital (HOMO) can be seen clearly. Right: The spectra are shown enlarged, so that the low coverage measurements can be seen in more detail.

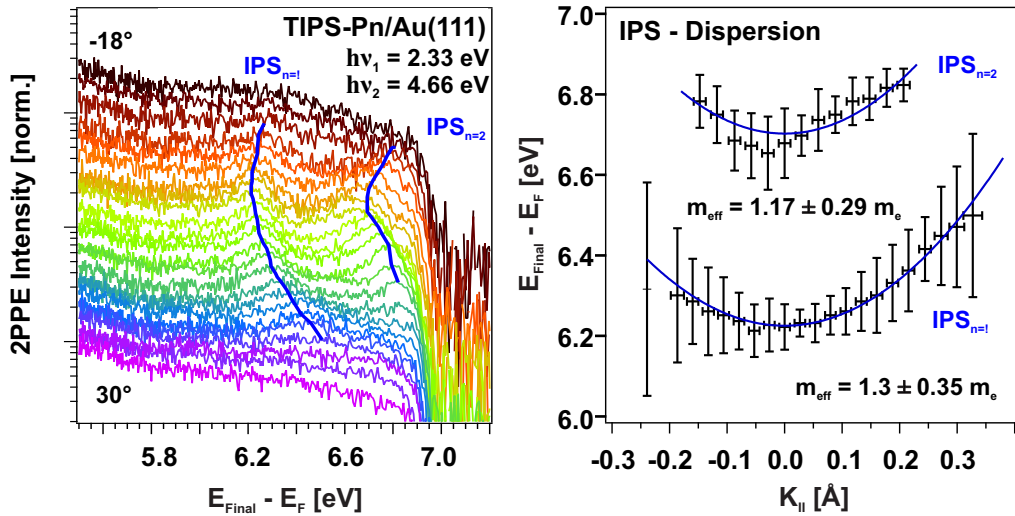


Figure A.3.: Dichromatic AR-2PPE measurements of 1 ML of TIPS-Pn adsorbed on Au(111) taken with a photon energy of 2.33 and 4.26 eV. Blue lines highlight the peak positions from the observed IPSs. An effective mass of $1.3 \pm 0.35 m_e$ and of $1.17 \pm 0.29 m_e$ is observed for the $\text{IPS}_{n=1}$ and $\text{IPS}_{n=2}$, respectively.

B. Additional FeTPyP Measurements

In this section of the appendix additional spectra obtained for the FeTPyP/Au(111) interface are presented. Figure B.1 shows several spectra of the cumulated signal, which is obtained when illuminating the sample with the UV- and the VIS-beam, for increasing illumination times. The cumulated spectrum contains both the monochromatic and the dichromatic spectrum. Usually the dichromatic spectrum is obtained from the cumulated spectrum by subtracting the monochromatic spectrum, which is obtained if the sample is only illuminated with the UV-beam. However, it can be seen, that the cumulated signal shows no significant change during short time illuminations, which means that neither the monochromatic nor the dichromatic spectrum shows a significant change, and therefore the measurements carried out for the FeTPyP/Au(111) interface can be regarded as not influenced by the laser beam. The full series of submonolayer measurements revealing an additional UMO, as it was discussed in section 6.3 is displayed in figure B.2 (a) and the related slope evaluation is given in figure B.2 (b). Additionally, the peak assigned to the LUMO is much better resolved for the submonolayer coverage than in figure 6.6. The peak observed directly at the Fermi edge of the spectrum is a peak resulting from merged contributions of the SS, the shifted SS' and the IPS and thus no clear slope evaluation could be carried out. A coverage series taken at the interface with a photon energy of $h\nu = 4.25 \text{ eV}$ can be found in figure B.3. The shift of the work function with increasing coverage can be clearly obtained. In the high energy region of the spectrum, which is shown enlarged, the shift and quenching of the SS with increasing coverage is observed. At around 7.3 eV the contribution of the UMO is observed, which get superimposed by the HOMO and OMOs contributions when the coverage is about 1 ML. The d-band features show a constant intensity, while the other molecule induced peaks assigned to the FS, LUMO and LUMO+1 gain in intensity while enlarging the amount of deposited molecules. For a coverage above 1 ML the contributions in the spectrum get very broad, probably due to a disordered surface arrangement, which makes a clear assignment difficult. Finally, B.4 shows AR-2PPE data observed for a submonolayer coverage. This data is shown to rule out a misassignment of the UMO₃ peak to the gold *sp*-band. There is no dispersion observed for this peak, which should be the case for the *sp*-band of the gold.

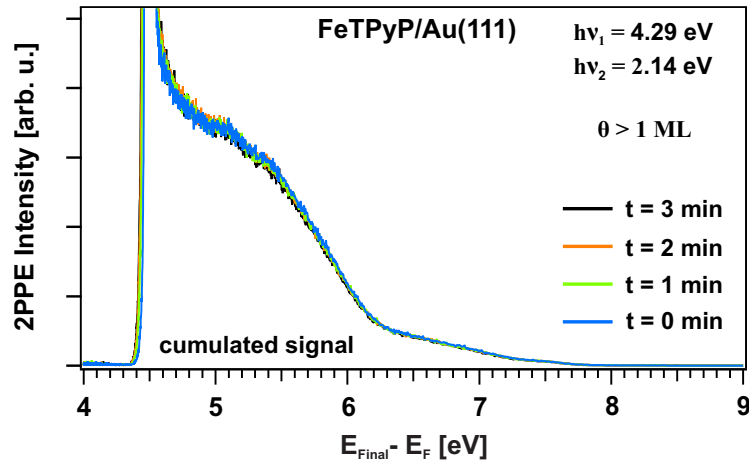


Figure B.1.: 2PPE Spectra of FeTPyP adsorbed on Au(111), after short time illuminations with the VIS- and the UV-beam. Shown is the superposition of the monochromatic and the dichromatic signal. Within short illumination times no significant change of the spectrum is obtained.

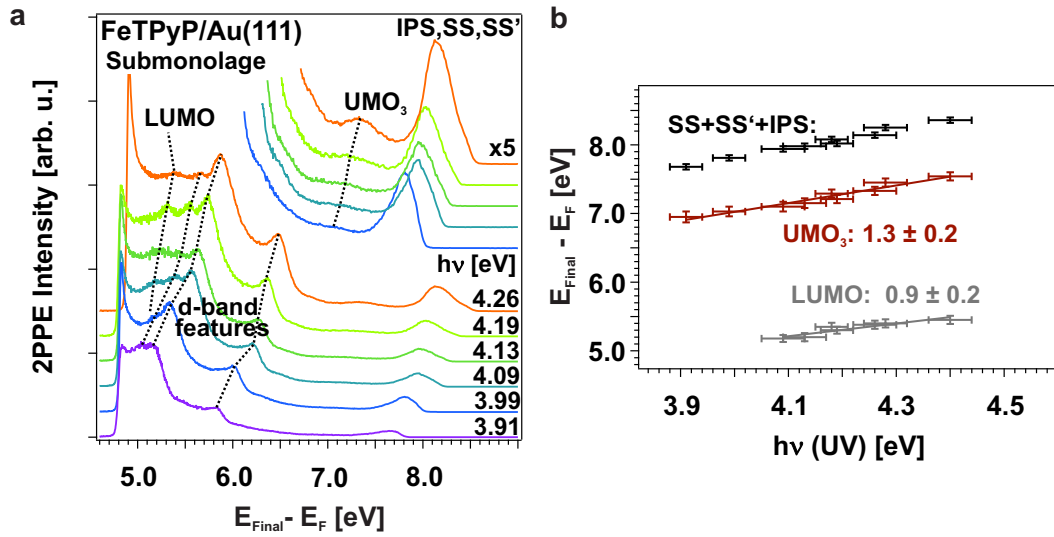


Figure B.2.: Monochromatic 2PPE spectra of approximately 0.3 ML FeTPyP on Au(111) recorded with several photon energies. 2PPE intensity is given as a function of the final state energy. Dotted lines highlight peaks resulting from the LUMO, d-band features and a higher lying UMO. On the right the slope evaluation of photon energy dependent measurements is given.

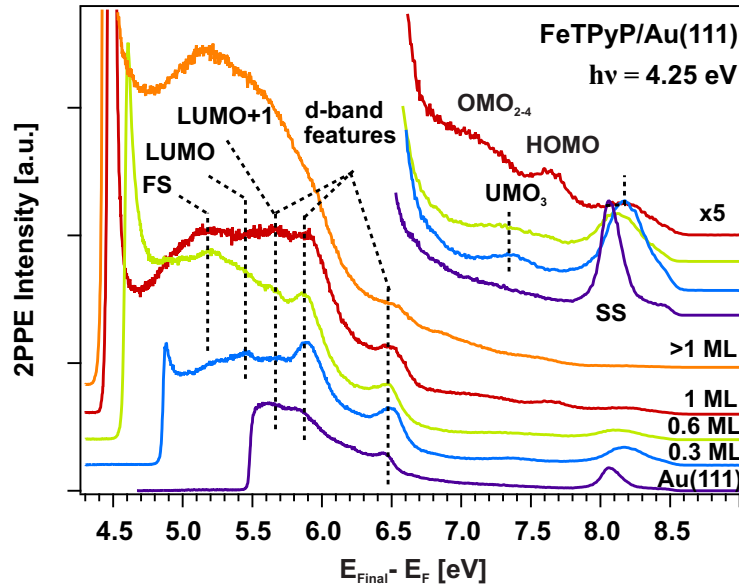


Figure B.3.: 2PPE Spectra of different coverages of FeTPyP adsorbed on Au(111). The coverage dependent shift of the work function can be seen clearly. Several molecule induced states are observed. Probably due to disarray of the adsorbed molecules, the peaks observed in the spectrum for coverages above one monolayer get very broad making a detailed analysis difficult. A misassignment of the LUMO being a further gold d-band features is ruled out, due to the increasing intensity, with increasing coverage. For $h\nu = 4.25 \text{ eV}$ the LUMO+1 and a d-band feature are located at the same position but photon energy dependent measurements show the presence of both. See section 6.3 for a more detailed discussion.

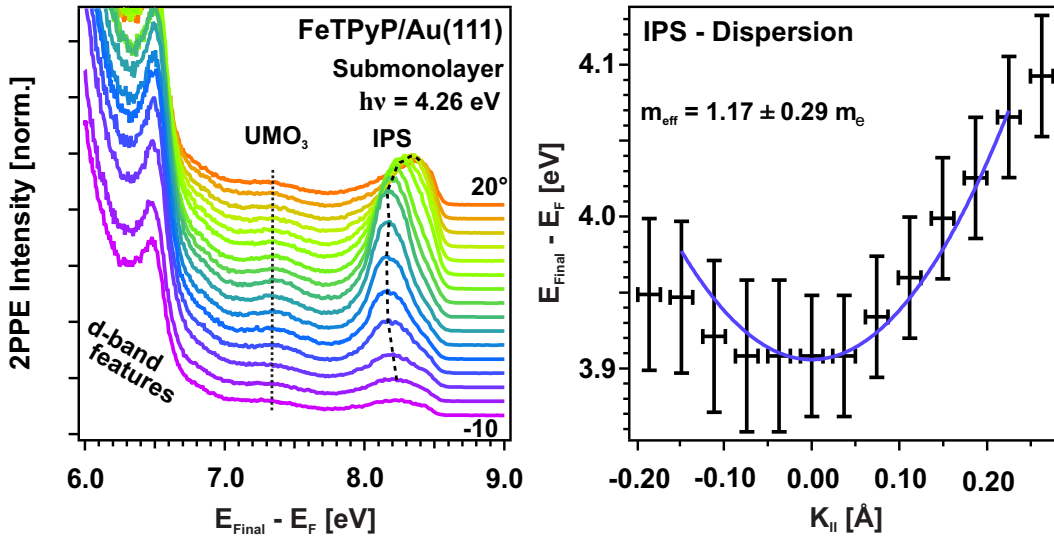


Figure B.4.: AR-2PPE measurements of a submonolayer coverage FeTPyP adsorbed on Au(111) taken with a photon energy of 4.26 eV. Dotted lines highlight the peak positions from a higher lying UMO and the IPS. An effective mass of $1.17 \pm 0.29 m_e$ is observed for the IPS, while the UMO_3 shows no observable dispersion parallel to the surface and so a disassignment to the gold sp-band is ruled out.

C. Additional TIPS-BAP Measurements

This section of the appendix mainly focuses on the illumination effects observed at the TIPS-BAP/Au(111) interface and some additional measurements to complete the picture of the electronic structure discussed in section 6.6. During the recording of the spectra, illumination induced changes were observed as can be seen in figure C.1 (a) and (b), where two spectra taken on a fresh and an illuminated spot ($t = 17 \text{ min}$; $h\nu = 4.29 \text{ eV}$) are shown. A strong intensity increase at the secondary edge and of the secondary electron background is accompanied with a disappearance of the weak HOMO related peak. Additionally, the peaks observed directly at the Fermi edge of the spectra resulting from the $\text{UMO}_{1/2}$ merge into one broad contribution. These all are hints for an illumination induced photodegradation of the adsorbed molecules, especially as this effect is even stronger observed for multilayer coverages (see figure C.2 (a)). To verify the interpretations made in section 6.6, so called illumination series were carried out. Several short lasting measurements are carried out, one behind the other, with short data acquisition times. This kind of spectra are displayed in figure C.1 (c) and (d) showing ten measurements taken at the same spot on the sample with an acquisition time of 10 s, each. In total an illumination time of 100 s is achieved, covering the time window needed for normal 2PPE measurements ($\approx 90 \text{ s}$). In contrast to long-lasting measurements, no significant changes in the spectra are observed confirming the validity of the electronic structure obtained from the measurements presented in section 6.6. Figure C.2 (b) shows the AR-2PPE spectra obtained to rule out a misassignment of the $\text{UMO}_{1/2}$ peaks observed directly at the Fermi edge of the spectrum, where the IPS could be expected. The IPS states show a significant dispersion, and therefore the peaks seem to be molecule induced. Short lasting measurements at the multilayer covered substrate reveal the position of the slightly shifted LUMO. The high energy cutoff of the spectrum is linked to excitations from the HOMO of TIPS-BAP and was fitted by a parabolic function to obtain the onset value.

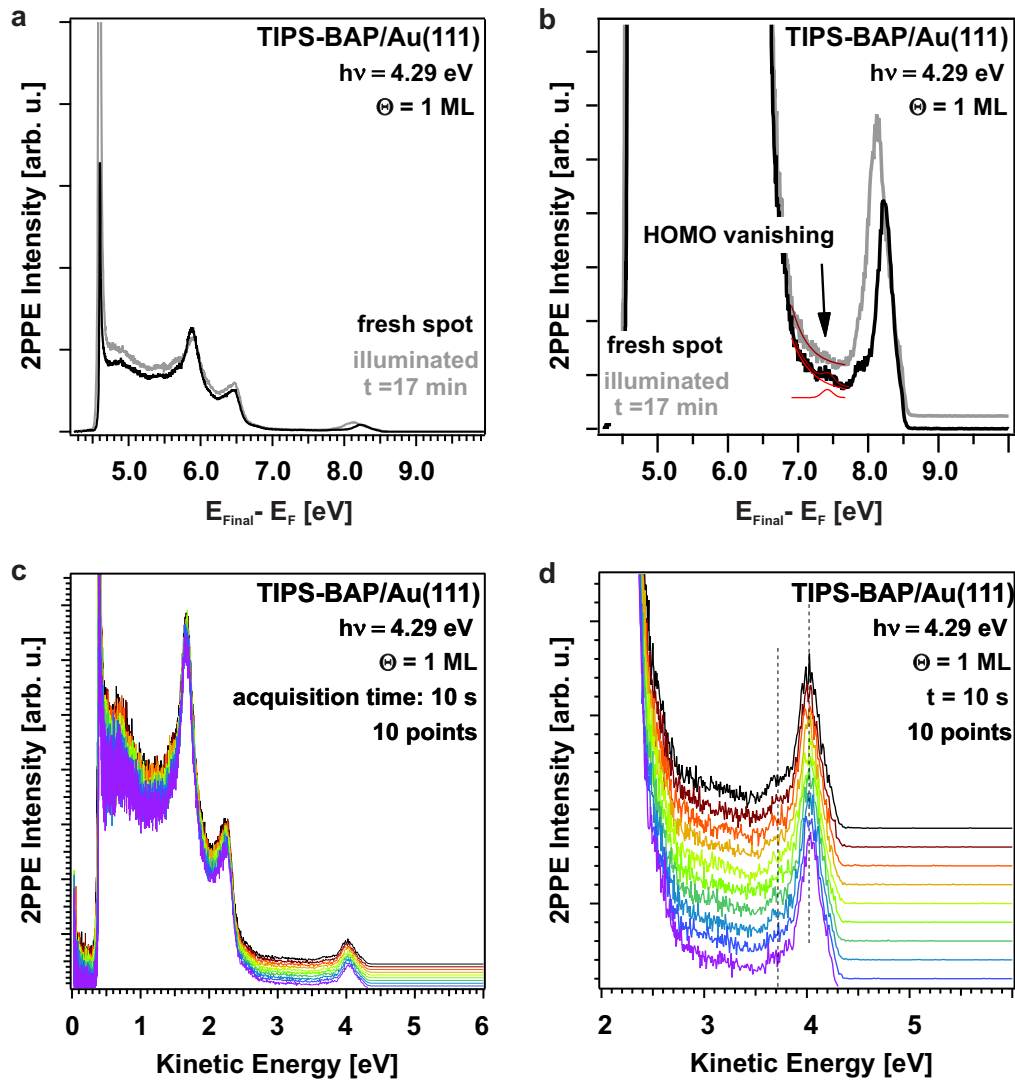


Figure C.1.: 2PPE measurements of 1 ML TIPS-BAP adsorbed on Au(111) taken with a photon energy of 4.29 eV. (a) and (b) show two spectra taken on a fresh and an illuminated spot. (c) and (d) show an illumination series with ten spectra, each acquired for 10 s.

C. Additional TIPS-BAP Measurements

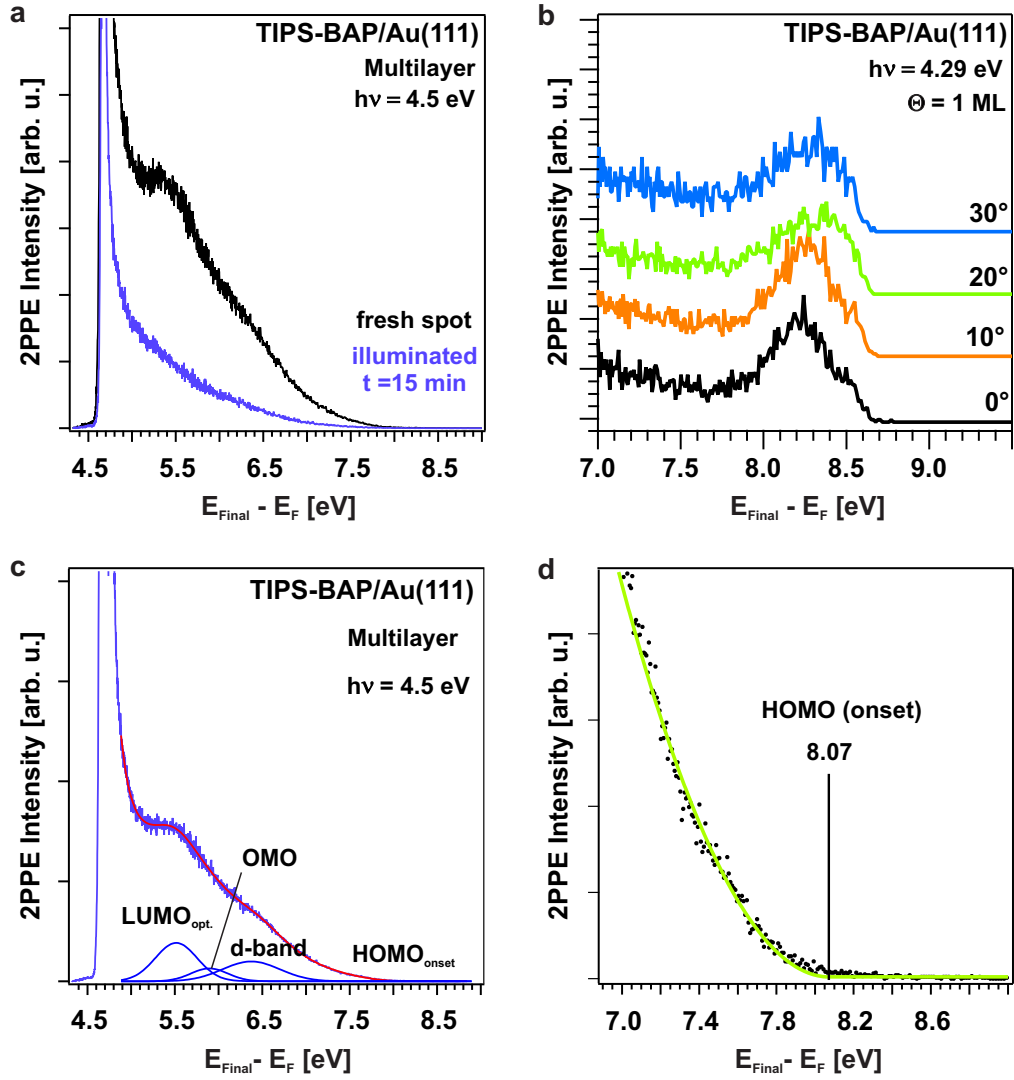


Figure C.2.: (a) 2PPE measurements of a TIPS-BAP multilayer adsorbed on Au(111) for a fresh spot and after illumination with a 4.5 eV beam for 15 min. (b) AR-2PPE measurements of 1 ML TIPS-BAP adsorbed on Au(111). (c) and (d) show a multilayer measurement on a fresh spot fitted by an exponential background and Gaussian-shaped peaks. The onset of the HOMO was fitted by a parabolic function.

D. Additional TAPP Measurements

This chapter contains all additional information used to complete the picture of the electronic structure observed at the interface between the TAPP derivatives and Au(111).

TAPP-(CF₃)₂

A full set of photon energy dependent measurements recorded at a coverage of 1 ML TAPP-(CF₃)₂ adsorbed on Au(111) is shown in figure D.1 (a) and (b). The monochromatic measurement in (a) contain several contributions in the low energy part of the spectra. The features assigned to the UMO₅ and the UIHB are independent of the photon energy but are most clear observed for high photon energies, as the *d*-band features and further molecule induced initial and intermediates states for those are shifted to higher final state energies. The peak originating from the LUMO is completely overimposed by the *d*-band features for photon energies below $h\nu = 4.33 \text{ eV}$ and is best observed for the spectrum obtained with a photon energy of $h\nu = 4.59 \text{ eV}$. Directly next to most intense *d*-band feature, the peak assigned to the OIHB is observed as a right shoulder or an individual peak, depending on the used photon energy. The first peak observed at higher final state energies than the *d*-band features originates from the HOMO and the contributions at the Fermi edge are attributed to the UMO_{3/4}, the shifted SS', and the IPS (not labeled). The shifted SS' and the first IPS can also be obtained nicely in the dichromatic measurements shown in figure D.1 (b), where a contribution of an additional state, the UMO₁, is observed as a weak low energy shoulder. The molecule induced shift and quenching of the SS is observed in coverage dependent measurements displayed in figure D.1 (c) and (d). Additionally, it can be seen clearly, that the contributions assigned to the UMO_{3/4} are molecule induced as they rise in intensity with increasing coverage. For coverages exceeding about 4 ML all molecule induced peaks merge into one broad contribution and thus a clear assignment gets challenging. Figure D.2 (a) and (b) also show coverage dependent spectra, where in (a) it can be seen, that the rise of the peak assigned to the UMO₁ and the shift of the SS is related to the deposition of molecules on the substrate, while in (b) the coverage dependent shift of the IPS is observed. Interestingly, the IPS shifts in the opposite direction as the work function (figure D.2 (c)), which can be explained by an increase of the molecule induced quantum defect a , calculated by equation 3.2.4 (figure D.1 (d)). To rule out a misassignment of the peak AR-2PPE measurements have

D. Additional TAPP Measurements

been carried out as can be seen in figure D.3. A clear dispersion is observed, but the determination of the effective mass is challenging, since the peak assigned to the IPS is located directly at the Fermi edge of the spectrum. This might explain the determination of a slightly to high effective mass for an IPS of $m_{eff} = 2.3 \pm 1.0 m_e$.

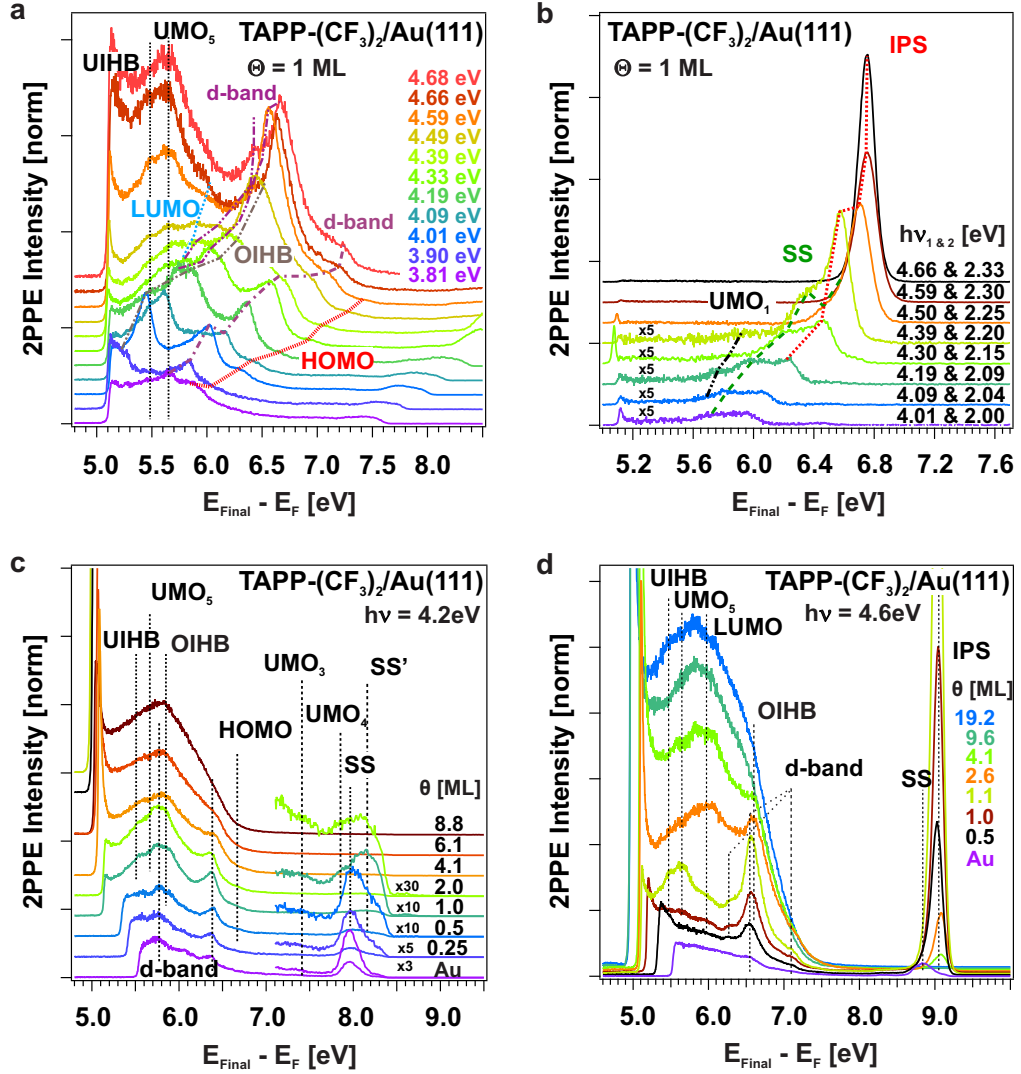


Figure D.1.: 2PPE measurements of TAPP-(CF₃)₂ adsorbed on Au(111) taken for several photon energies and at different coverages. Dotted lines highlight the peak positions resulting from multiple electronic states and interface bands. See text and section 7.1 for additional information.

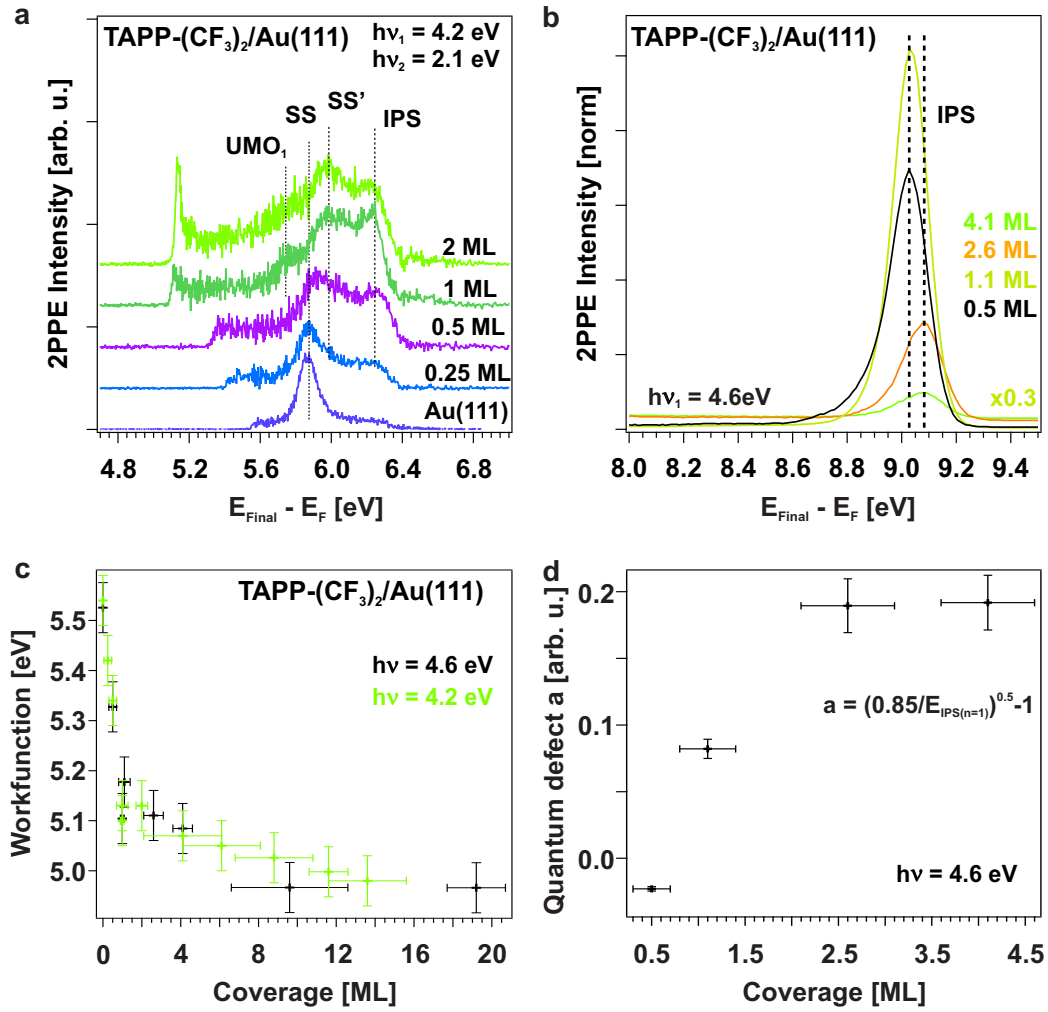


Figure D.2.: (a) and (b) 2PPE measurements of TAPP-(CF₃)₂ adsorbed on Au(111) taken for several photon energies and at different coverages. (c) Coverage dependent work function shift of TAPP-(CF₃)₂ adsorbed on Au(111). Coverage dependent quantum defect of the first IPS at the TAPP-(CF₃)₂ covered Au(111) surface.

D. Additional TAPP Measurements

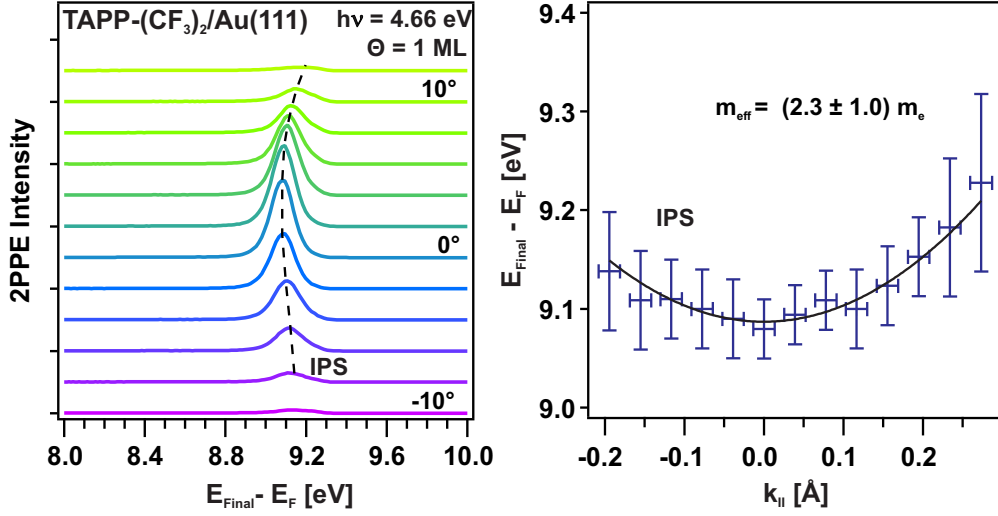


Figure D.3.: AR-2PPE measurements of TAPP-(CF₃)₂ adsorbed on Au(111) taken at a coverage of 1 ML. Dotted lines highlight the peak positions from the first IPS. An effective mass of $2.3 \pm 1.0 m_e$ is observed for the IPS, ruling out a misassignment to a molecule derived UMO.

TAPP

Here the measurements leading to the electronic structure of the TAPP/Au(111) interface shown in figure 7.6 are displayed. Figure D.4 shows monochromatic (a) and dichromatic (b) measurements at a coverage of 1 ML with peaks highlighted by dashed lines. The peaks were assigned to initial, intermediate, and final states by the slope evaluation shown in figure D.4 (c) and (d) with their energies being $E_{SS'} = -0.31 \pm 0.11$ eV, $E_{HOMO} = -1.73 \pm 0.06$ eV, $E_{OIHB} = -2.48 \pm 0.06$ eV, $E_{LUMO} = 1.36 \pm 0.06$ eV, $E_{UMO_1} = 1.53 \pm 0.10$ eV, $E_{UMO_2} = 1.96 \pm 0.08$ eV, $E_{IPS_{n=1}} = 3.94 \pm 0.09$ eV, $E_{IPS_{n=2}} = 4.50 \pm 0.11$ eV, and $E_{UMO_5} = 5.21 \pm 0.06$ eV. The peaks assigned to the shifted SS' and the IPS states are located directly at the secondary edge of the monochromatic spectra and the assignment is based on the determination of their dispersion and their energy in respect to E_{Fermi} and E_{vac} , respectively. The HOMO is assigned to the energetically highest observed molecule induced initial state. For the assignment of the OIHB, observed directly next to the high intensity *d*-band feature refer to section 7.4. The peaks originating from the LUMO and higher lying UMOs are located at a final state energy below the *d*-band features and thus stand out only weakly. For clarity, the spectrum

Appendix

obtained for a photon energy of $h\nu = 4.3 \text{ eV}$ is shown separated and fitted by an exponential background and Gaussian-shaped peaks in figure D.5 (a). The dichromatic spectra (figure D.4 (b)) reveal a further UMO_2 and for high photon energies a weak contribution of the second IPS is observed directly at the Fermi edge. To complete the picture, dichromatic measurements with the 3 eV -beam were carried out. A clear peak originating from the UMO_5 , and contributions underpinning the energetic positions of the HOMO, LUMO, $\text{IPS}_{n=1}$, and shifted SS' are observed.

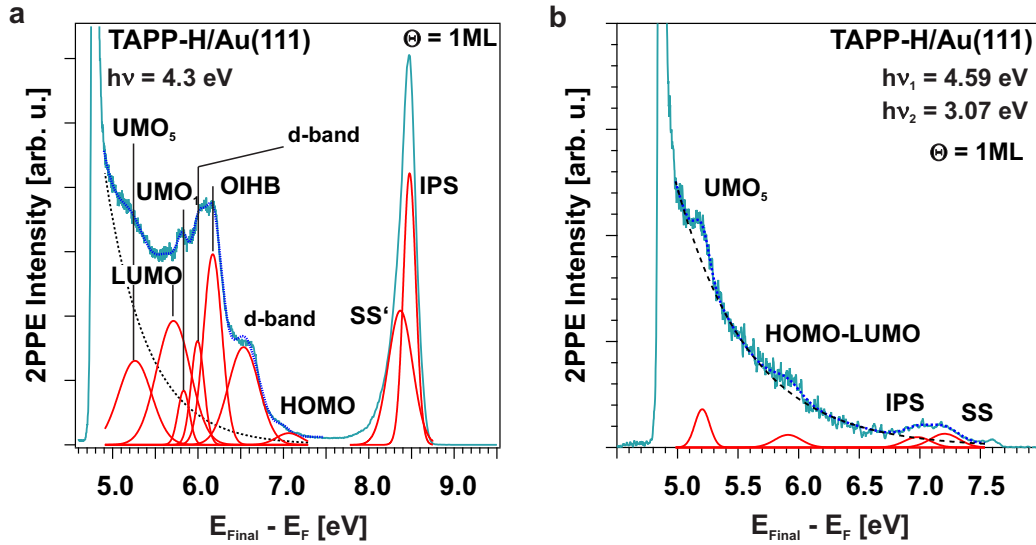


Figure D.5.: Spectra of 1 ML TAPP adsorbed on Au(111) fitted with an exponential background and Gaussian-shaped peaks. (a) Monochromatic spectrum taken with a photon energy of $h\nu = 4.3 \text{ eV}$. (b) Dichromatic spectrum taken with photon energies of $h\nu = 3.07 \text{ eV}$ and $h\nu = 4.59 \text{ eV}$.

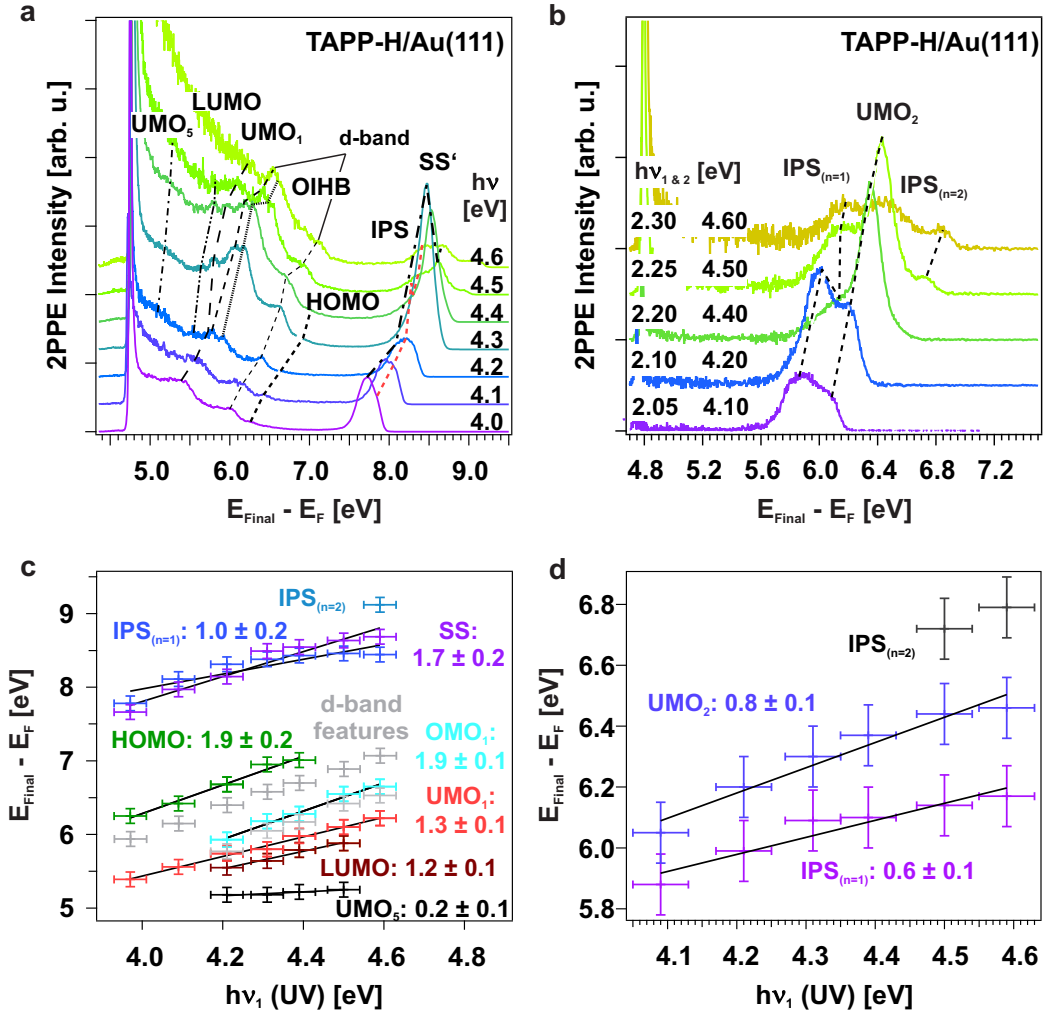


Figure D.4.: (a) Monochromatic and (b) dichromatic 2PPE spectra of TAPP adsorbed on Au(111) recorded with different photon energies. Dotted lines highlight the peak positions from multiple electronic states and interface bands. See text and section 7.1 for additional information. (c) and (d) show the corresponding photon energy dependent peak positions to assign peaks observed in the 2PPE spectrum.

TAPP-(C₃F₇)₂

For the sake of completeness, in this section all measurements regarding the TAPP-(C₃F₇)₂/Au(111) interface are presented. The TPD and 2PPE measurements were carried out by Dr. David Gerbert and Alexander Broska (also refer to [274]). The EI-MS spectrum of TAPP-(C₃F₇)₂ displayed in D.6 (a) was carried out by the Mass Spectrometry Facility of the Institut of Organic Chemistry of the University of Heidelberg under the lead of Juergen Gross. It shows the peak of the molecular mass as well as several masses created *via* fragmentations. D.6 (b) shows TPD spectra for different initial coverages, measured for the ionic fragment $m/z = 69$, which can be assigned to a -CF₃ group. A zero-order shaped multilayer peak (α_1) is observed around 400 K, while the monolayer (α_3) and a condensed phase (α_2) are observed between 600 – 700 K. Figure D.7 shows several 2PPE measurements at the interface (1 ML) carried out with different photon energies. The peaks were assigned to initial, intermediate, and final states by the slope evaluation shown in figure D.7 (c) and (d) with their energies being $E_{SS} = -0.29 \pm 0.05$ eV, $E_{HOMO} = -1.73 \pm 0.06$ eV, $E_{OIHB} = -2.50 \pm 0.06$ eV, $E_{UMO_4} = 3.74 \pm 0.06$ eV, $E_{UMO_5} = 6.02 \pm 0.07$ eV, $E_{UIHB} = 5.57 \pm 0.06$ eV, and $E_{IPS_{n=1}} = 4.53 \pm 0.07$ eV with respect to E_{Fermi} . The assignments of the peaks are based on the determined energetic positions with respect to E_{Fermi} and the dispersion measurements shown in figure 7.7 (section 7.4). The contributions of the HOMO are only observed for low photon energies in the monochromatic and high photon energies in the dichromatic spectra. IPS and SS contribution are found directly at the Fermi edge. The UIHB and UMO₅ contributions are located energetically below the *d*-band features in the monochromatic spectra, while they are rather weak in the dichromatic spectra.

D. Additional TAPP Measurements

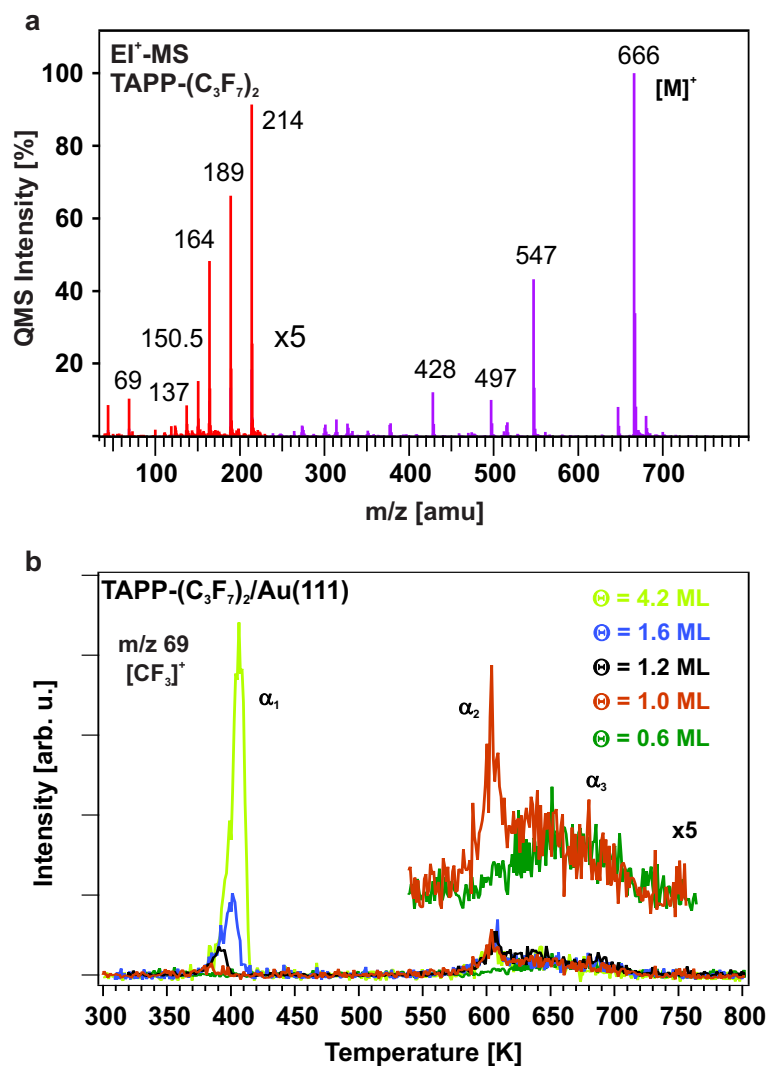


Figure D.6.: (a) EI-MS spectrum of TAPP-(C₃F₇)₂. The part of the spectrum observable by the QMS attached to the UHV chamber is shown enlarged. Important fragments are labeled. (b) TPD measurements (ionic fragment $m/z = 69$) of TAPP-(C₃F₇)₂ adsorbed on Au(111) for different initial coverages recorded with a heating rate of 1 K/s. α_3 and α_2 denote the monolayer, while α_1 denotes the multilayer. Data measured by Dr. David Gerbert and Alexander Broska.

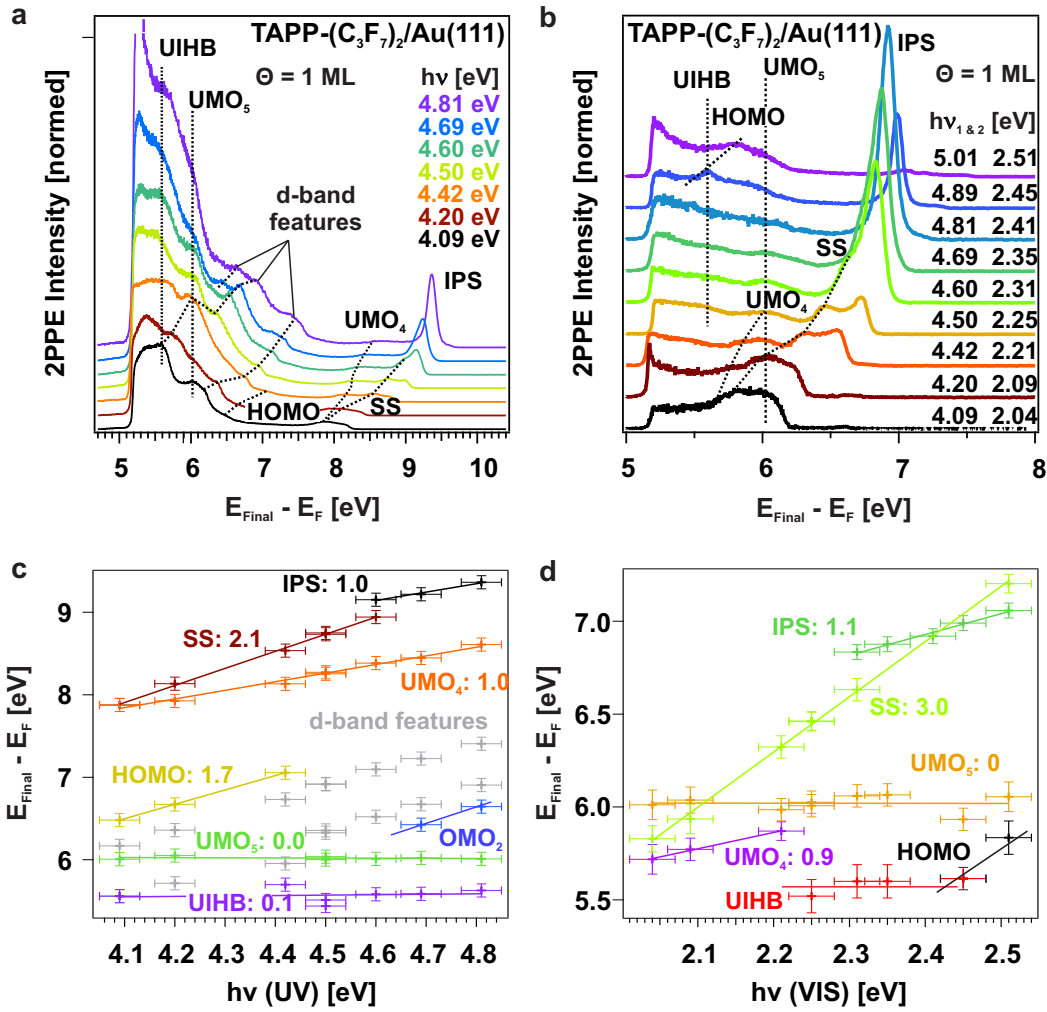


Figure D.7.: (a) Monochromatic and (b) dichromatic 2PPE spectra of 1 ML TAPP-(C₃F₇)₂ adsorbed on Au(111) recorded with different photon energies. Dotted lines highlight the peak positions from multiple electronic states and interface bands. See text and chapter 7 for additional information. (c) and (d) show the corresponding photon energy dependent peak positions to assign peaks observed in the 2PPE spectrum. Data measured by Dr. David Gerbert and Alexander Broska and reevaluated by the author.

Bibliography

- [1] O. Ostroverkhova. Organic optoelectronic materials: Mechanisms and applications. *Chemical Reviews*, 116(22):13279–13412, 2016.
- [2] T. Ameri, P. Khoram, J. Min, and C. J. Brabec. Organic ternary solar cells: A review. *Advanced Materials*, 25(31):4245–4266, 2013.
- [3] M. Wright and A. Uddin. Organic - inorganic hybrid solar cells: A comparative review. *Solar Energy Materials and Solar cells*, 107:87–111, 2012.
- [4] V. Coropceanu, J. Cornil, D. A. da Silva Filho, Y. Olivier, R. Silbey, and J. Brédas. Charge transport in organic semiconductors. *Chemical Reviews*, 107(4):926–952, 2007.
- [5] S. R. Forrest. Ultrathin organic films grown by organic molecular beam deposition and related techniques. *Chemical Reviews*, 97(6):1793–1896, 1997.
- [6] L. S. Hung and C. H. Chen. Recent progress of molecular organic electroluminescent materials and devices. *Materials Science and Engineering: R: Reports*, 39(5-6):143–222, 2002.
- [7] D. Berner, H. Houili, W. Leo, and L. Zuppiroli. Insights into OLED functioning through coordinated experimental measurements and numerical model simulations. *Physica Status Solidi (a)*, 202(1):9–36, 2005.
- [8] K. Walzer, B. Maennig, M. Pfeiffer, and K. Leo. Highly efficient organic devices based on electrically doped transport layers. *Chemical Reviews*, 107(4):1233–1271, 2007.
- [9] S. Reineke, F. Lindner, G. Schwartz, N. Seidler, K. Walzer, B. Lüssem, and K. Leo. White organic light-emitting diodes with fluorescent tube efficiency. *Nature*, 459(7244):234, 2009.
- [10] H. Sirringhaus, N. Tessler, and R. H. Friend. Integrated optoelectronic devices based on conjugated polymers. *Science*, 280(5370):1741–1744, 1998.

Bibliography

- [11] B. W. D'Andrade and S. R. Forrest. White organic light-emitting devices for solid-state lighting. *Advanced Materials*, 16(18):1585–1595, 2004.
- [12] Z. B. Wang, M. G. Helander, J. Qiu, D. P. Puzzo, M. T. Greiner, Z. M. Hudson, S. Wang, Z. W. Liu, and Z. H. Lu. Unlocking the full potential of organic light-emitting diodes on flexible plastic. *Nature Photonics*, 5(12):753, 2011.
- [13] J. Lee, H. Chen, T. Batagoda, C. Coburn, P. I. Djurovich, M. E. Thompson, and S. R. Forrest. Deep blue phosphorescent organic light-emitting diodes with very high brightness and efficiency. *Nature Materials*, 15(1):92, 2016.
- [14] H. Sirringhaus. Device physics of solution-processed organic field-effect transistors. *Advanced Materials*, 17(20):2411–2425, 2005.
- [15] T. Sekitani, U. Zschieschang, H. Klauk, and T. Someya. Flexible organic transistors and circuits with extreme bending stability. *Nature Materials*, 9(12):1015, 2010.
- [16] L. Torsi, M. Magliulo, K. Manoli, and G. Palazzo. Organic field-effect transistor sensors: A tutorial review. *Chemical Society Reviews*, 42(22):8612–8628, 2013.
- [17] C. D. Dimitrakopoulos and D. J. Masearo. Organic thin-film transistors: A review of recent advances. *IBM Journal of Research and Development*, 45(1):11–27, 2001.
- [18] C. D. Dimitrakopoulos and P. R. L. Malenfant. Organic thin film transistors for large area electronics. *Advanced Materials*, 14(2):99–117, 2002.
- [19] Y. Wen, Y. Liu, Y. Guo, G. Yu, and W. Hu. Experimental techniques for the fabrication and characterization of organic thin films for field-effect transistors. *Chemical Reviews*, 111(5):3358–3406, 2011.
- [20] Y. Guo, G. Yu, and Y. Liu. Functional organic field-effect transistors. *Advanced Materials*, 22(40):4427–4447, 2010.
- [21] P. Peumans, A. Yakimov, and S. R. Forrest. Small molecular weight organic thin-film photodetectors and solar cells. *Journal of Applied Physics*, 93(7):3693–3723, 2003.
- [22] S. E. Shaheen, D. S. Ginley, and G. E. Jabbour. Organic-based photovoltaics: toward low-cost power generation. *MRS Bulletin*, 30(1):10–19, 2005.

- [23] Y. Liu, J. Zhao, Z. Li, C. Mu, W. Ma, H. Hu, K. Jiang, H. Lin, H. Ade, and H. Yan. Aggregation and morphology control enables multiple cases of high-efficiency polymer solar cells. *Nature Communications*, 5:5293, 2014.
- [24] C. Chen, W. Chang, K. Yoshimura, K. Ohya, J. You, J. Gao, Z. Hong, and Y. Yang. An efficient triple-junction polymer solar cell having a power conversion efficiency exceeding 11 %. *Advanced Materials*, 26(32):5670–5677, 2014.
- [25] W. Zhao, S. Li, H. Yao, S. Zhang, Y. Zhang, B. Yang, and J. Hou. Molecular optimization enables over 13% efficiency in organic solar cells. *Journal of the American Chemical Society*, 139(21):7148–7151, 2017.
- [26] Y. Yang, Z. Zhang, H. Bin, S. Chen, L. Gao, L. Xue, C. Yang, and Y. Li. Side-chain isomerization on an n-type organic semiconductor ITIC acceptor makes 11.77% high efficiency polymer solar cells. *Journal of the American Chemical Society*, 138(45):15011–15018, 2016.
- [27] J. Hou, O. Inganäs, R. H. Friend, and F. Gao. Organic solar cells based on non-fullerene acceptors. *Nature Materials*, 17(2):119, 2018.
- [28] T. Yokota, P. Zalar, M. Kaltenbrunner, H. Jinno, N. Matsuhisa, H. Kitano, Y. Tachibana, W. Yukita, M. Koizumi, and T. Someya. Ultraflexible organic photonic skin. *Science Advances*, 2(4):e1501856, 2016.
- [29] T. Sekitani, H. Nakajima, H. Maeda, T. Fukushima, T. Aida, K. Hata, and T. Someya. Stretchable active-matrix organic light-emitting diode display using printable elastic conductors. *Nature Materials*, 8(6):494, 2009.
- [30] S. R. Forrest. The path to ubiquitous and low-cost organic electronic appliances on plastic. *Nature*, 428(6986):911, 2004.
- [31] M. C. Gather, A. Koehnen, A. Falcou, H. Becker, and K. Meerholz. Solution-processed full-color polymer organic light-emitting diode displays fabricated by direct photolithography. *Advanced Functional Materials*, 17(2):191–200, 2007.
- [32] G. Yu. Image sensors made from organic semiconductors, October 9 2001. US Patent 6,300,612.
- [33] T. Sekitani, T. Yokota, U. Zschieschang, H. Klauk, S. Bauer, K. Takeuchi, M. Takamiya, T. Sakurai, and T. Someya. Organic

Bibliography

- nonvolatile memory transistors for flexible sensor arrays. *Science*, 326(5959):1516–1519, 2009.
- [34] B. Crone, A. Dodabalapur, A. Gelperin, L. Torsi, H. E. Katz, A. J. Lovinger, and Z. Bao. Electronic sensing of vapors with organic transistors. *Applied Physics Letters*, 78(15):2229–2231, 2001.
- [35] L.P. Ma, J. Liu, and Y. Yang. Organic electrical bistable devices and rewritable memory cells. *Applied Physics Letters*, 80(16):2997–2999, 2002.
- [36] S. Möller, C. Perlov, W. Jackson, C. Taussig, and S. R. Forrest. A polymer/semiconductor write-once read-many-times memory. *Nature*, 426(6963):166, 2003.
- [37] C. Chu, J. Ouyang, J. Tseng, and Y. Yang. Organic donor–acceptor system exhibiting electrical bistability for use in memory devices. *Advanced Materials*, 17(11):1440–1443, 2005.
- [38] S. Geib, S. C. Martens, M. Märken, A. Rybina, H. Wadepohl, and L. H. Gade. Tuning redox chemistry and photophysics in core-substituted tetraazaperopyrenes (TAPPs). *Chemistry—A European Journal*, 19(41):13811–13822, 2013.
- [39] W. Brutting and W. Rieß. Grundlagen der organischen Halbleiter. *Physik Journal*, 7(5):33, 2008.
- [40] A. Facchetti. Semiconductors for organic transistors. *Materials Today*, 10(3):28–37, 2007.
- [41] N. Koch, N. Ueno, and A. T. S. Wee. *The Molecule-Metal Interface*. John Wiley & Sons, 2013.
- [42] H. Ishii, K. Sugiyama, E. Ito, and K. Seki. Energy level alignment and interfacial electronic structures at organic/metal and organic/organic interfaces. *Advanced Materials*, 11(8):605–625, 1999.
- [43] X. Zhou, J. Blochwitz, M. Pfeiffer, A. Nollau, T. Fritz, and K. Leo. Enhanced hole injection into amorphous hole-transport layers of organic light-emitting diodes using controlled p-type doping. *Advanced Functional Materials*, 11(4):310–314, 2001.
- [44] J. C. Scott. Metal–organic interface and charge injection in organic electronic devices. *Journal of Vacuum Science & Technology A: Vacuum, Surfaces, and Films*, 21(3):521–531, 2003.

- [45] S. Braun, W. R. Salaneck, and M. Fahlman. Energy-level alignment at organic/metal and organic/organic interfaces. *Advanced Materials*, 21(14-15):1450–1472, 2009.
- [46] P. K. H. Ho, J. Kim, J. H. Burroughes, H. Becker, S. F. Y. Li, T. M. Brown, F. Cacialli, and R. H. Friend. Molecular-scale interface engineering for polymer light-emitting diodes. *Nature*, 404(6777):481, 2000.
- [47] A. Kumatani, Y. Li, P. Darmawan, T. Minari, and K. Tsukagoshi. On practical charge injection at the metal/organic semiconductor interface. *Scientific Reports*, 3:1026, 2013.
- [48] M. Oehzelt, N. Koch, and G. Heimel. Organic semiconductor density of states controls the energy level alignment at electrode interfaces. *Nature Communications*, 5:4174, 2014.
- [49] D. J. Gundlach, Y. Lin, T. N. Jackson, S. F. Nelson, and D. G. Schlom. Pentacene organic thin-film transistors-molecular ordering and mobility. *IEEE Electron Device Letters*, 18(3):87–89, 1997.
- [50] H. Sirringhaus, P. J. Brown, R. H. Friend, M. M. Nielsen, K. Bechgaard, B. M. W. Langeveld-Voss, A. J. H. Spiering, R. A. J. Janssen, E. W. Meijer, P. Herwig, et al. Two-dimensional charge transport in self-organized, high-mobility conjugated polymers. *Nature*, 401(6754):685, 1999.
- [51] N. Koch. Organic electronic devices and their functional interfaces. *ChemPhysChem*, 8(10):1438–1455, 2007.
- [52] Q. Bao, S. Fabiano, M. Andersson, S. Braun, Z. Sun, X. Crispin, M. Berggren, X. Liu, and M. Fahlman. Energy level bending in ultrathin polymer layers obtained through langmuir–shäfer deposition. *Advanced Functional Materials*, 26(7):1077–1084, 2016.
- [53] S. Rhee and D. Yun. Metal–semiconductor contact in organic thin film transistors. *Journal of Materials Chemistry*, 18(45):5437–5444, 2008.
- [54] R. Pfattner, C. Rovira, and M. Mas-Torrent. Organic metal engineering for enhanced field-effect transistor performance. *Physical Chemistry Chemical Physics*, 17(40):26545–26552, 2015.
- [55] H. Yamane, S. Kera, K. K. Okudaira, D. Yoshimura, K. Seki, and N. Ueno. Intermolecular energy-band dispersion in PTCDA multilayers. *Physical Review B*, 68(3):033102, 2003.

Bibliography

- [56] S. Machida, Y. Nakayama, S. Duhm, Q. Xin, A. Funakoshi, N. Ogawa, S. Kera, N. Ueno, and H. Ishii. Highest-occupied-molecular-orbital band dispersion of rubrene single crystals as observed by angle-resolved ultraviolet photoelectron spectroscopy. *Physical Review Letters*, 104(15):156401, 2010.
- [57] Q. Xin, S. Duhm, F. Bussolotti, K. Akaike, Y. Kubozono, H. Aoki, T. Kosugi, S. Kera, and N. Ueno. Accessing surface Brillouin zone and band structure of picene single crystals. *Physical Review Letters*, 108(22):226401, 2012.
- [58] J. Brédas, J. P. Calbert, D. A. da Silva Filho, and J. Cornil. Organic semiconductors: A theoretical characterization of the basic parameters governing charge transport. *Proceedings of the National Academy of Sciences*, 99(9):5804–5809, 2002.
- [59] M. Wießner, J. Ziroff, F. Forster, M. Arita, K. Shimada, P. Puschnig, A. Schöll, and F. Reinert. Substrate-mediated band-dispersion of adsorbate molecular states. *Nature Communications*, 4:1514, 2013.
- [60] M. Wießner, J. Kübert, V. Feyer, P. Puschnig, A. Schöll, and F. Reinert. Lateral band formation and hybridization in molecular monolayers: NTCDA on Ag(110) and Cu(100). *Physical Review B*, 88(7):075437, 2013.
- [61] D. Gerbert, O. T. Hofmann, and P. Tegeder. Formation of occupied and unoccupied hybrid bands at interfaces between metals and organic donors/acceptors. *The Journal of Physical Chemistry C*, 122(48):27554–27560, 2018.
- [62] H. Yamane and N. Kosugi. High hole-mobility molecular layer made from strong electron acceptor molecules with metal adatoms. *The Journal of Physical Chemistry Letters*, 8(21):5366–5371, 2017.
- [63] C. Bronner, M. Schulze, S. Hagen, and P. Tegeder. The influence of the electronic structure of adsorbate–substrate complexes on photoisomerization ability. *New Journal of Physics*, 14(4):043023, 2012.
- [64] A. Stein, F. Maaß, and P. Tegeder. Triisopropylsilylethynyl-pentacene on Au(111): Adsorption properties, electronic structure, and singlet fission dynamics. *The Journal of Physical Chemistry C*, 121(33):18075–18083, 2017.

- [65] A. Stein, D. Rolf, C. Lotze, C. Czekelius, K. J. Franke, and P. Tegeder. Electronic structure of an iron porphyrin derivative on Au(111). *Journal of Physics: Condensed Matter*, 31(4):044002, 2018.
- [66] C. Bronner, G. Schulze, K. J. Franke, J. I. Pascual, and P. Tegeder. Switching ability of nitro-spiropyran on Au(111): Electronic structure changes as a sensitive probe during a ring-opening reaction. *Journal of Physics: Condensed Matter*, 23(48):484005, 2011.
- [67] L. Bogner, Z. Yang, S. Baum, M. Corso, R. Fitzner, P. Bäuerle, K. J. Franke, J. I. Pascual, and P. Tegeder. Electronic states and exciton dynamics in dicyanovinyl-sexithiophene on Au(111). *The Journal of Physical Chemistry C*, 120(48):27268–27275, 2016.
- [68] L. Bogner, Z. Yang, M. Corso, R. Fitzner, P. Bäuerle, K. J. Franke, J. I. Pascual, and P. Tegeder. Electronic structure and excited state dynamics in a dicyanovinyl-substituted oligothiophene on Au(111). *Physical Chemistry Chemical Physics*, 17(40):27118–27126, 2015.
- [69] F. Maaß, Y. Jiang, W. Liu, A. Tkatchenko, and P. Tegeder. Binding energies of benzene on coinage metal surfaces: Equal stability on different metals. *The Journal of Chemical Physics*, 148(21):214703, 2018.
- [70] J. H. Schön, S. Berg, C. Kloc, and B. Batlogg. Ambipolar pentacene field-effect transistors and inverters. *Science*, 287(5455):1022–1023, 2000.
- [71] J. H. Schön, C. Kloc, E. Bucher, and B. Batlogg. Efficient organic photovoltaic diodes based on doped pentacene. *Nature*, 403(6768):408, 2000.
- [72] C. D. Dimitrakopoulos, S. Purushothaman, J. Kymissis, A. Callegari, and J. M. Shaw. Low-voltage organic transistors on plastic comprising high-dielectric constant gate insulators. *Science*, 283(5403):822–824, 1999.
- [73] Z. Huang, Y. Jang, X. Yang, W. Cao, and J. Zhang. The synthesis and photoelectric study of 6,13-bis(4-propylphenyl)pentacene, and its TiO₂ nano-sized composite films. *Journal of Physics and Chemistry of Solids*, 71(3):296–302, 2010.
- [74] J. E. Anthony, J. S. Brooks, D. L. Eaton, and S. R. Parkin. Functionalized pentacene: improved electronic properties from control of solid-state order. *Journal of the American Chemical Society*, 123(38):9482–9483, 2001.

Bibliography

- [75] H. L. Stern, A. Cheminal, S. R. Yost, K. Broch, S. L. Bayliss, K. Chen, M. Tabachnyk, K. Thorley, N. Greenham, J. M. Hodgkiss, et al. Vibronically coherent ultrafast triplet-pair formation and subsequent thermally activated dissociation control efficient endothermic singlet fission. *Nature Chemistry*, 9(12):1205, 2017.
- [76] W. Chan, M. Ligges, and X-Y Zhu. The energy barrier in singlet fission can be overcome through coherent coupling and entropic gain. *Nature Chemistry*, 4(10):840, 2012.
- [77] P. M. Zimmerman, F. Bell, D. Casanova, and M. Head-Gordon. Mechanism for singlet fission in pentacene and tetracene: from single exciton to two triplets. *Journal of the American Chemical Society*, 133(49):19944–19952, 2011.
- [78] D. Beljonne, H. Yamagata, J. L. Brédas, F. C. Spano, and Y. Olivier. Charge-transfer excitations steer the Davydov splitting and mediate singlet exciton fission in pentacene. *Physical Review Letters*, 110(22):226402, 2013.
- [79] A. Rao, M. W. B. Wilson, J. M. Hodgkiss, S. Albert-Seifried, H. Bassler, and R. H. Friend. Exciton fission and charge generation via triplet excitons in pentacene/C₆₀ bilayers. *Journal of the American Chemical Society*, 132(36):12698–12703, 2010.
- [80] N. Monahan and X-Y. Zhu. Charge transfer-mediated singlet fission. *Annual Review of Physical Chemistry*, 66:601–618, 2015.
- [81] S. Sharifzadeh, P. Darancet, L. Kronik, and J. B. Neaton. Low-energy charge-transfer excitons in organic solids from first-principles: The case of pentacene. *The Journal of Physical Chemistry Letters*, 4(13):2197–2201, 2013.
- [82] W. Chan, M. Ligges, A. Jailaubekov, L. Kaake, L. Miaja-Avila, and X-Y. Zhu. Observing the multiexciton state in singlet fission and ensuing ultrafast multielectron transfer. *Science*, 334(6062):1541–1545, 2011.
- [83] M. W. B. Wilson, A. Rao, J. Clark, R. S. S. Kumar, D. Brida, G. Cerullo, and R. H. Friend. Ultrafast dynamics of exciton fission in polycrystalline pentacene. *Journal of the American Chemical Society*, 133(31):11830–11833, 2011.
- [84] S. R. Yost, J. Lee, M. W. B. Wilson, T. Wu, D. P. McMahon, R. R. Parkhurst, N. J. Thompson, D. N. Congreve, A. Rao, K. Johnson,

- et al. A transferable model for singlet-fission kinetics. *Nature Chemistry*, 6(6):492, 2014.
- [85] N. R. Monahan, D. Sun, H. Tamura, K. W. Williams, B. Xu, Y. Zhong, B. Kumar, C. Nuckolls, A. R. Harutyunyan, G. Chen, et al. Dynamics of the triplet-pair state reveals the likely coexistence of coherent and incoherent singlet fission in crystalline hexacene. *Nature Chemistry*, 9(4):341, 2017.
- [86] J. E. Anthony. The larger acenes: Versatile organic semiconductors. *Angewandte Chemie International Edition*, 47(3):452–483, 2008.
- [87] M. Müller, E. C. Rüdiger, S. Koser, O. Tverskoy, F. Rominger, F. Hinkel, J. Freudenberg, and U. H. F. Bunz. "Butterfly Wings" stabilize heptacene. *Chemistry—A European Journal*, 24(32):8087–8091, 2018.
- [88] B. Purushothaman, S. R. Parkin, and J. E. Anthony. Synthesis and stability of soluble hexacenes. *Organic Letters*, 12(9):2060–2063, 2010.
- [89] M. M. Payne, S. R. Parkin, and J. E. Anthony. Functionalized higher acenes: hexacene and heptacene. *Journal of the American Chemical Society*, 127(22):8028–8029, 2005.
- [90] J. Herz, T. Buckup, F. Paulus, J. Engelhart, U. H. F. Bunz, and M. Motzkus. Acceleration of singlet fission in an aza-derivative of TIPS-pentacene. *The Journal of Physical Chemistry Letters*, 5(14):2425–2430, 2014.
- [91] S. Miao, A. L. Appleton, N. Berger, S. Barlow, S. R. Marder, K. I. Hardcastle, and U. H. F. Bunz. 6, 13-diethynyl-5, 7, 12, 14-tetraazapentacene. *Chemistry—A European Journal*, 15(20):4990–4993, 2009.
- [92] A. L. Appleton, S. M. Brombosz, S. Barlow, J. S. Sears, J. Bredas, S. R. Marder, and U. H. F. Bunz. Effects of electronegative substitution on the optical and electronic properties of acenes and diazaacenes. *Nature Communications*, 1:91, 2010.
- [93] O. Tverskoy, F. Rominger, A. Peters, H. Himmel, and U. H. F. Bunz. An efficient synthesis of tetraazapentacenes. *Angewandte Chemie International Edition*, 50(15):3557–3560, 2011.
- [94] J. J. Hoff, L. Zhu, Y. Dong, T. Albers, P. J. Steel, X. Cui, Y. Wen, I. Lebedyeva, and S. Miao. Diazapentacene derivatives: Synthesis, properties, and structures. *RSC Advances*, 6(90):86824–86828, 2016.

Bibliography

- [95] M. Winkler and K. N. Houk. Nitrogen-rich oligoacenes: Candidates for n-channel organic semiconductors. *Journal of the American Chemical Society*, 129(6):1805–1815, 2007.
- [96] L. Hahn, S. Öz, H. Wadepohl, and L. H. Gade. Highly emissive water-soluble tetraazaperopyrenes as fluorescent markers. *Chemical Communications*, 50(38):4941–4943, 2014.
- [97] S. C. Martens, U. Zschieschang, H. Wadepohl, H. Klauk, and L. H. Gade. Tetrachlorinated tetraazaperopyrenes (TAPPs): Highly fluorescent dyes and semiconductors for air-stable organic n-channel transistors and complementary circuits. *Chemistry—A European Journal*, 18(12):3498–3509, 2012.
- [98] S. Geib, U. Zschieschang, M. Gsänger, M. Stolte, F. Würthner, H. Wadepohl, H. Klauk, and L. H. Gade. Core-brominated tetraazaperopyrenes as n-channel semiconductors for organic complementary circuits on flexible substrates. *Advanced Functional Materials*, 23(31):3866–3874, 2013.
- [99] S. C. Martens, T. Riehm, S. Geib, H. Wadepohl, and L. H. Gade. Substituent effects in the periphery of 2, 9-bisaryl-tetraazaperopyrene dyes. *J. Org. Chem*, 76(2):609–617, 2011.
- [100] S. Hoefener, B. Günther, M. E. Harding, and L. H. Gade. Understanding UV/Vis spectra of halogenated tetraazaperopyrenes (TAPPs): A computational study. *The Journal of Physical Chemistry A*, 2019.
- [101] S. Langbein, H. Wadepohl, and L. H. Gade. Ditopic N-heterocyclic pincer carbene complexes containing a perylene backbone. *Organometallics*, 35(5):809–815, 2016.
- [102] L. Hahn, H. Wadepohl, and L. H. Gade. Tetralithiated tetraazaperopyrene as a key intermediate for the synthesis of functionalized derivatives. *Organic letters*, 17(9):2266–2269, 2015.
- [103] T. Riehm, G. De Paoli, A. E. Konradsson, L. De Cola, H. Wadepohl, and L. H. Gade. Tetraazaperopyrenes: A new class of multifunctional chromophores. *Chemistry—A European Journal*, 13(26):7317–7329, 2007.
- [104] S. Langbein, H. Wadepohl, and L. H. Gade. Arylmercapto substituted tetraazaperopyrene derivatives and their oxidation to tetrasulfones: Photophysics and electrochemistry. *The Journal of Organic Chemistry*, 80(24):12620–12626, 2015.

- [105] L. Hahn, F. Maaß, T. Bleith, U. Zschieschang, H. Wadepohl, H. Klauk, P. Tegeder, and L. H. Gade. Core halogenation as a construction principle in tuning the material properties of tetraazaperopyrenes. *Chemistry—A European Journal*, 21(49):17691–17700, 2015.
- [106] L. Hahn, A. Hermannsdorfer, B. Günther, T. Wesp, B. Bühler, U. Zschieschang, H. Wadepohl, H. Klauk, and L. H. Gade. (Oligo-) thiophene functionalized tetraazaperopyrenes: Donor–acceptor dyes and ambipolar organic semiconductors. *The Journal of Organic Chemistry*, 82(23):12492–12502, 2017.
- [107] J. M. Gottfried. Surface chemistry of porphyrins and phthalocyanines. *Surface Science Reports*, 70(3):259–379, 2015.
- [108] M. Jurow, A. E. Schuckman, J. D. Batteas, and C. M. Drain. Porphyrins as molecular electronic components of functional devices. *Coordination Chemistry Reviews*, 254(19-20):2297–2310, 2010.
- [109] J. Otsuki. STM studies on porphyrins. *Coordination Chemistry Reviews*, 254(19-20):2311–2341, 2010.
- [110] W. Auwärter, D. Écija, F. Klappenberger, and J. V. Barth. Porphyrins at interfaces. *Nature Chemistry*, 7(2):105, 2015.
- [111] J. Kesters, P. Verstappen, M. Kelchtermans, L. Lutsen, D. Vanderzande, and W. Maes. Porphyrin-based bulk heterojunction organic photovoltaics: The rise of the colors of life. *Advanced Energy Materials*, 5(13):1500218, 2015.
- [112] H. Marbach. Surface-mediated in situ metalation of porphyrins at the solid–vacuum interface. *Accounts of Chemical Research*, 48(9):2649–2658, 2015.
- [113] B. W. Heinrich, L. Braun, J. I. Pascual, and K. J. Franke. Tuning the magnetic anisotropy of single molecules. *Nano Letters*, 15(6):4024–4028, 2015.
- [114] H. Bockmann, S. Liu, J. Mielke, S. Gawinkowski, J. Waluk, L. Grill, M. Wolf, and T. Kumagai. Direct observation of photoinduced tautomerization in single molecules at a metal surface. *Nano Letters*, 16(2):1034–1041, 2016.
- [115] S. Karan, C. García, M. Karolak, D. Jacob, N. Lorente, and R. Berndt. Spin control induced by molecular charging in a transport junction. *Nano Letters*, 18(1):88–93, 2017.

Bibliography

- [116] D. Rolf, C. Lotze, C. Czekelius, B. W. Heinrich, and K. J. Franke. Visualizing intramolecular distortions as the origin of transverse magnetic anisotropy. *The Journal of Physical Chemistry Letters*, 9(22):6563–6567, 2018.
- [117] S. Hunklinger. *Festkörperphysik*. Oldenbourg Verlag, 2009.
- [118] H. Ibach and H. Lüth. *Festkörperphysik: Einführung in die Grundlagen*. Springer-Verlag, 2009.
- [119] R. Gross and A. Marx. *Festkörperphysik*. Walter de Gruyter GmbH & Co KG, 2018.
- [120] H. Lüth. *Solid surfaces, Interfaces and thin Films*, volume 4. Springer, 2001.
- [121] I. J. Tamm. Über eine mögliche Art der Elektronenbindung an Kristalloberflächen. *Zeitschrift für Physik*, 76(11-12):849–850, 1932.
- [122] W. Shockley. On the surface states associated with a periodic potential. *Physical Review*, 56(4):317, 1939.
- [123] K. Oura, V. G. Lifshits, A. A. Saranin, A. V. Zotov, and M. Katayama. *Surface Science: an Introduction*. 2013.
- [124] H. Ibach. *Physics of Surfaces and Interfaces*, volume 12. Springer, 2006.
- [125] P. Sandl, U. Bischler, and E. Bertel. The interaction of atomic hydrogen with Cu(110). *Surface Science*, 291(1-2):29–38, 1993.
- [126] T. Andreev, I. Barke, and H. Hövel. Adsorbed rare-gas layers on Au(111): Shift of the Shockley surface state studied with ultraviolet photoelectron spectroscopy and scanning tunneling spectroscopy. *Physical Review B*, 70(20):205426, 2004.
- [127] F. Forster, A. Bendounan, F. Reinert, V. G. Grigoryan, and M. Springborg. The Shockley-type surface state on Ar covered Au(111): High resolution photoemission results and the description by slab-layer DFT calculations. *Surface Science*, 601(23):5595–5604, 2007.
- [128] D. Gerbert and P. Tegeder. Molecular ion formation by photoinduced electron transfer at the Tetracyanoquinodimethane/Au(111) interface. *The Journal of Physical Chemistry Letters*, 8(19):4685–4690, 2017.

- [129] A. Scheybal, K. Müller, R. Bertschinger, M. Wahl, A. Bendounan, P. Aebi, and T. A. Jung. Modification of the Cu(110) Shockley surface state by an adsorbed pentacene monolayer. *Physical Review B*, 79(11):115406, 2009.
- [130] J. Ziroff, P. Gold, A. Bendounan, F. Forster, and F. Reinert. Adsorption energy and geometry of physisorbed organic molecules on Au(111) probed by surface-state photoemission. *Surface Science*, 603(2):354–358, 2009.
- [131] H. Yamane and N. Kosugi. Photoelectron angular distribution induced by weak intermolecular interaction in highly ordered aromatic molecules. *The Journal of Physical Chemistry C*, 122(46):26472–26479, 2018.
- [132] J-Y. Park, U. D. Ham, S-J. Kahng, Y. Kuk, K. Miyake, K. Hata, and H. Shigekawa. Modification of surface-state dispersion upon Xe adsorption: A scanning tunneling microscope study. *Physical Review B*, 62(24):R16341, 2000.
- [133] F. Forster, G. Nicolay, F. Reinert, D. Ehm, S. Schmidt, and S. Hüfner. Surface and interface states on adsorbate covered noble metal surfaces. *Surface Science*, 532:160–165, 2003.
- [134] T. Fauster and W. Steinmann. Two-photon photoemission spectroscopy of image states. *Electromagnetic Waves: Recent Developments in Research*, 2:347–411, 1995.
- [135] H. Lüth. Adsorption on solid surfaces. In *Solid Surfaces, Interfaces and Thin Films*. Springer, 2015.
- [136] J. Güdde and U. Höfer. Femtosecond time-resolved studies of image-potential states at surfaces and interfaces of rare-gas adlayers. *Progress in Surface Science*, 80(3-4):49–91, 2005.
- [137] P. M. Echenique and J. B. Pendry. Theory of image states at metal surfaces. *Progress in Surface Science*, 32(2):111–159, 1989.
- [138] D. Straub and F. J. Himpsel. Spectroscopy of image-potential states with inverse photoemission. *Physical Review B*, 33(4):2256, 1986.
- [139] E. V. Chulkov, V. M. Silkin, and P. M. Echenique. Image potential states on metal surfaces: Binding energies and wave functions. *Surface Science*, 437(3):330–352, 1999.

Bibliography

- [140] A. Hotzel. Electron dynamics of image potential states in weakly bound adsorbate layers: A short review. *Progress in Surface Science*, 82(4-6):336–354, 2007.
- [141] B. K. Min, A. R. Alemozafar, M. M. Biener, J. Biener, and C. M. Friend. Reaction of Au(111) with sulfur and oxygen: Scanning tunneling microscopic study. *Topics in Catalysis*, 36(1-4):77–90, 2005.
- [142] F. Hanke and J. Björk. Structure and local reactivity of the Au(111) surface reconstruction. *Physical Review B*, 87(23):235422, 2013.
- [143] N. Takeuchi, C. T. Chan, and K. M. Ho. Au(111): A theoretical study of the surface reconstruction and the surface electronic structure. *Physical Review B*, 43(17):13899, 1991.
- [144] S. D. Kevan and R. H. Gaylord. High-resolution photoemission study of the electronic structure of the noble-metal (111) surfaces. *Physical Review B*, 36(11):5809, 1987.
- [145] F. Reinert. Spin-orbit interaction in the photoemission spectra of noble metal surface states. *Journal of Physics: Condensed Matter*, 15(5):S693, 2003.
- [146] K. Schouteden, P. Lievens, and C. Van Haesendonck. Fourier-transform scanning tunneling microscopy investigation of the energy versus wave vector dispersion of electrons at the Au(111) surface. *Physical Review B*, 79(19):195409, 2009.
- [147] H. Eckardt, L. Fritsche, and J. Noffke. Self-consistent relativistic band structure of the noble metals. *Journal of Physics F: Metal Physics*, 14(1):97, 1984.
- [148] K. Lauwaet, K. Schouteden, E. Janssens, C. Van Haesendonck, P. Lievens, M. I. Trioni, L. Giordano, and G. Pacchioni. Resolving all atoms of an alkali halide via nanomodulation of the thin NaCl film surface using the Au(111) reconstruction. *Physical Review B*, 85(24):245440, 2012.
- [149] G. Wedler. *Lehrbuch der Physikalischen Chemie*. John Wiley & Sons, 5 edition, 2004.
- [150] T. Miyamae, S. Hasegawa, D. Yoshimura, H. Ishii, N. Ueno, and K. Seki. Intramolecular energy-band dispersion in oriented thin films of

- $n\text{-CF}_3(\text{CF}_2)_{22}\text{CF}_3$ observed by angle-resolved photoemission with synchrotron radiation. *The Journal of Chemical Physics*, 112(7):3333–3338, 2000.
- [151] K. Seki, U. Karlsson, R. Engelhardt, and E. E. Koch. Intramolecular energy band dispersion of $n\text{-C}_{36}\text{H}_{74}$ observed by angle-resolved photoemission with synchrotron radiation. *Chemical Physics Letters*, 103(5):343–346, 1984.
- [152] H. Fujimoto, T. Mori, H. Inokuchi, N. Ueno, K. Sugita, and K. Seki. Intramolecular band mapping of $n\text{-CH}_3(\text{CH}_2)_{34}\text{CH}_3$ over the whole Brillouin zone by angle-resolved photoemission. *Chemical Physics Letters*, 141(6):485–488, 1987.
- [153] C. Zubrügél, F. Schneider, M. Neumann, G. Hähner, C. Wöll, and M. Grunze. Electronic structure of alkane chains. Complete one-dimensional band structures of the valence states. *Chemical Physics Letters*, 219(1-2):127–131, 1994.
- [154] K. Seki, N. Ueno, U. O. Karlsson, R. Engelhardt, and E. Koch. Valence bands of oriented finite linear chain molecular solids as model compounds of polyethylene studied by angle-resolved photoemission. *Chemical Physics*, 105(1-2):247–265, 1986.
- [155] S. Narioka, H. Ishii, K. Edamatsu, K. Kamiya, S. Hasegawa, T. Ohta, N. Ueno, and K. Seki. Angle-resolved photoelectron spectroscopic study of oriented p-sexiphenyl: Wave-number conservation and blurring in a short model compound of poly(p-phenylene). *Physical Review B*, 52(4):2362, 1995.
- [156] D. Yoshimura, H. Ishii, Y. Ouchi, E. Ito, T. Miyamae, S. Hasegawa, K. K. Okudaira, N. Ueno, and K. Seki. Angle-resolved ultraviolet photoelectron spectroscopy and theoretical simulation of a well-ordered ultrathin film of tetratetracontane ($n\text{-C}_{44}\text{H}_{90}$) on Cu(100): Molecular orientation and intramolecular energy-band dispersion. *Physical Review B*, 60(12):9046, 1999.
- [157] J. Bredas. Mind the gap! *Materials Horizons*, 1(1):17–19, 2014.
- [158] P. I. Djurovich, E. I. Mayo, S. R. Forrest, and M. E. Thompson. Measurement of the lowest unoccupied molecular orbital energies of molecular organic semiconductors. *Organic Electronics*, 10(3):515–520, 2009.
- [159] M. Henzler and W. Göpel. Oberflächenphysik des Festkörpers. *Teubner*, 1994.

Bibliography

- [160] H. Vázquez, F. Flores, R. Oszwaldowski, J. Ortega, R. Perez, and A. Kahn. Barrier formation at metal–organic interfaces: Dipole formation and the charge neutrality level. *Applied Surface Science*, 234(1-4):107–112, 2004.
- [161] H. Vázquez, W. Gao, F. Flores, and A. Kahn. Energy level alignment at organic heterojunctions: Role of the charge neutrality level. *Physical Review B*, 71(4):041306, 2005.
- [162] H. Vazquez, F. Flores, and A. Kahn. Induced density of states model for weakly-interacting organic semiconductor interfaces. *Organic Electronics*, 8(2-3):241–248, 2007.
- [163] R. Smoluchowski. Anisotropy of the electronic work function of metals. *Physical Review*, 60(9):661, 1941.
- [164] D. Gerbert, F. Maaß, and P. Tegeder. Extended space charge region and unoccupied molecular band formation in epitaxial tetrafluorotetracyanoquinodimethane films. *The Journal of Physical Chemistry C*, 121(29):15696–15701, 2017.
- [165] A. Terentjevs, M. P. Steele, M. L. Blumenfeld, N. Ilyas, L. L. Kelly, E. Fabiano, O. L. A. Monti, and F. Della Sala. Interfacial electronic structure of the dipolar vanadyl naphthalocyanine on Au(111): "Push-Back" vs dipolar effects. *The Journal of Physical Chemistry C*, 115(43):21128–21138, 2011.
- [166] G. Witte, S. Lukas, P. S. Bagus, and C. Wöll. Vacuum level alignment at organic/metal junctions: Cushion effect and the interface dipole. *Applied Physics Letters*, 87(26):263502, 2005.
- [167] P. C. Rusu, G. Giovannetti, C. Weijtens, R. Coehoorn, and G. Brocks. Work function pinning at metal-organic interfaces. *The Journal of Physical Chemistry C*, 113(23):9974–9977, 2009.
- [168] O. T. Hofmann, D. A. Egger, and E. Zojer. Work-function modification beyond pinning: When do molecular dipoles count? *Nano Letters*, 10(11):4369–4374, 2010.
- [169] W. Shockley and H. J. Queisser. Detailed balance limit of efficiency of p-n junction solar cells. *Journal of Applied Physics*, 32(3):510–519, 1961.
- [170] M. B. Smith and J. Michl. Singlet fission. *Chemical Reviews*, 110(11):6891–6936, 2010.

- [171] M. B. Smith and J. Michl. Recent advances in singlet fission. *Annual Review of Physical Chemistry*, 64:361–386, 2013.
- [172] K. Miyata, F. S. Conrad-Burton, F. L. Geyer, and X-Y. Zhu. Triplet pair states in singlet fission. *Chemical Reviews*, 119(6):4261–4292, 2019.
- [173] E. C. Greyson, J. Vura-Weis, J. Michl, and M. A. Ratner. Maximizing singlet fission in organic dimers: Theoretical investigation of triplet yield in the regime of localized excitation and fast coherent electron transfer. *The Journal of Physical Chemistry B*, 114(45):14168–14177, 2010.
- [174] D. Casanova. Theoretical modeling of singlet fission. *Chemical Reviews*, 118(15):7164–7207, 2018.
- [175] M. J. Y. Tayebjee, S. N. Sanders, E. Kumarasamy, L. M. Campos, M. Y. Sfeir, and D. R. McCamey. Quintet multiexciton dynamics in singlet fission. *Nature Physics*, 13(2):182, 2017.
- [176] W. Chan, T. C. Berkelbach, M. R. Provorse, N. R. Monahan, J. R. Tritsch, M. S. Hybertsen, D. R. Reichman, J. Gao, and X-Y. Zhu. The quantum coherent mechanism for singlet fission: Experiment and theory. *Accounts of Chemical Research*, 46(6):1321–1329, 2013.
- [177] A. A. Bakulin, S. E. Morgan, T. B. Kehoe, M. W. B. Wilson, A. W. Chin, D. Zigmantas, D. Egorova, and A. Rao. Real-time observation of multiexcitonic states in ultrafast singlet fission using coherent 2D electronic spectroscopy. *Nature Chemistry*, 8(1):16, 2016.
- [178] H. Nagashima, S. Kawaoka, S. Akimoto, T. Tachikawa, Y. Matsui, H. Ikeda, and Y. Kobori. Singlet-fission-born quintet state: Sublevel selections and trapping by multiexciton thermodynamics. *The Journal of Physical Chemistry Letters*, 9(19):5855–5861, 2018.
- [179] A. J. Musser, M. Liebel, C. Schnedermann, T. Wende, T. B. Kehoe, A. Rao, and P. Kukura. Evidence for conical intersection dynamics mediating ultrafast singlet exciton fission. *Nature Physics*, 11(4):352, 2015.
- [180] P. E. Teichen and J. D. Eaves. Collective aspects of singlet fission in molecular crystals. *The Journal of Chemical Physics*, 143(4):044118, 2015.
- [181] J. Herz, T. Buckup, F. Paulus, J. U. Engelhart, U. H. F. Bunz, and M. Motzkus. Unveiling singlet fission mediating states in TIPS-pentacene and its aza derivatives. *The Journal of Physical Chemistry A*, 119(25):6602–6610, 2015.

Bibliography

- [182] R. D. Pensack, E. E. Ostroumov, A. J. Tilley, S. Mazza, C. Grieco, K. J. Thorley, J. B. Asbury, D. S. Seferos, J. E. Anthony, and G. D. Scholes. Observation of two triplet-pair intermediates in singlet exciton fission. *The Journal of Physical Chemistry Letters*, 7(13):2370–2375, 2016.
- [183] Z. Birech, M. Schwoerer, T. Schmeiler, J. Pflaum, and H. Schwoerer. Ultrafast dynamics of excitons in tetracene single crystals. *The Journal of Chemical Physics*, 140(11):114501, 2014.
- [184] J. J. Burdett and C. J. Bardeen. The dynamics of singlet fission in crystalline tetracene and covalent analogs. *Accounts of Chemical Research*, 46(6):1312–1320, 2013.
- [185] M. W. B. Wilson, A. Rao, K. Johnson, S. Gélinas, R. Di Pietro, J. Clark, and R. H. Friend. Temperature-independent singlet exciton fission in tetracene. *Journal of the American Chemical Society*, 135(44):16680–16688, 2013.
- [186] E. M. Grumstrup, J. C. Johnson, and N. H. Damrauer. Enhanced triplet formation in polycrystalline tetracene films by femtosecond optical-pulse shaping. *Physical Review Letters*, 105(25):257403, 2010.
- [187] J. B. Taylor and I. Langmuir. The evaporation of atoms, ions and electrons from caesium films on tungsten. *Physical Review*, 44(6):423, 1933.
- [188] P. A. Redhead. Thermal desorption of gases. *Vacuum*, 12(4):203–211, 1962.
- [189] D. A. King. Thermal desorption from metal surfaces: A review. *Surface Science*, 47(1):384–402, 1975.
- [190] C. G. Goymour and D. A. King. Chemisorption of carbon monoxide on tungsten. Part 2. Lateral interaction model for desorption kinetics. *Journal of the Chemical Society, Faraday Transactions 1: Physical Chemistry in Condensed Phases*, 69:749–760, 1973.
- [191] E. G. Seebauer, A. C. F. Kong, and L. D. Schmidt. The coverage dependence of the pre-exponential factor for desorption. *Surface Science*, 193(3):417–436, 1988.
- [192] A. M. De Jong and J. W. Niemantsverdriet. Thermal desorption analysis: Comparative test of ten commonly applied procedures. *Surface Science*, 233(3):355–365, 1990.

- [193] Friedrich Maaß. *The Metal/Organic Interface - Binding, Adsorption Geometry, and Electronic Structure*. PhD thesis, Universität Heidelberg - Fachbereich Chemie, 2018.
- [194] C. Bronner, J. Björk, and P. Tegeder. Tracking and removing Br during the on-surface synthesis of a graphene nanoribbon. *The Journal of Physical Chemistry C*, 119(1):486–493, 2014.
- [195] E. N. Sickafus. Linearized secondary-electron cascades from the surfaces of metals. I. Clean surfaces of homogeneous specimens. *Physical Review B*, 16(4):1436, 1977.
- [196] K. K. Okudaira, S. Hasegawa, P. T. Sprunger, E. Morikawa, V. Saile, K. Seki, Y. Harada, and N. Ueno. Photoemission study of pristine and photodegraded poly(methyl methacrylate). *Journal of Applied Physics*, 83(8):4292–4298, 1998.
- [197] T. Yamada, M. Shibuta, Y. Ami, Y. Takano, A. Nonaka, K. Miyakubo, and T. Munakata. Novel growth of naphthalene overlayer on Cu(111) studied by STM, LEED, and 2PPE. *The Journal of Physical Chemistry C*, 114(31):13334–13339, 2010.
- [198] D. Wisbey, N. Wu, Y. Losovyj, I. Ketsman, A. N. Caruso, D. Feng, J. Belot, E. Vescovo, and P. A. Dowben. Radiation-induced decomposition of the metal-organic molecule Bis(4-cyano-2, 2, 6, 6-tetramethyl-3, 5-heptanedionato) copper (II). *Applied Surface Science*, 255(6):3576–3580, 2009.
- [199] N. Koch, D. Pop, R. L. Weber, N. Böwering, B. Winter, M. Wick, G. Leising, I. V. Hertel, and W. Braun. Radiation induced degradation and surface charging of organic thin films in ultraviolet photoemission spectroscopy. *Thin Solid Films*, 391(1):81–87, 2001.
- [200] P. Bröms, N. Johansson, R. W. Gymer, S. C. Graham, R. H. Friend, and W. R. Salaneck. Low energy electron degradation of poly(p-phenylenevinylene). *Advanced Materials*, 11(10):826–832, 1999.
- [201] D. Velic, E. Knoesel, and M. Wolf. Observation of a direct transition in the sp-band of Cu(111) and (3×3) R30°-CO/Cu(111) in one-and two-photon photoemission. *Surface Science*, 424(1):1–6, 1999.
- [202] H. Ueba and B. Gumhalter. Theory of two-photon photoemission spectroscopy of surfaces. *Progress in Surface Science*, 82(4-6):193–223, 2007.

Bibliography

- [203] Christopher Bronner. *Photoinduced and Thermal Reactions of Functional Molecules at Surfaces*. PhD thesis, Freien Universität Berlin - Fachbereich Physik, 2014.
- [204] Christopher Bronner. Electronic Structure and Ultrafast Charge Carrier Dynamics at the Interfaces between Molecular Switches and the Au(111) Surface Investigated with Time-Resolved Photoemission. Master's thesis, Freien Universität Berlin - Fachbereich Physik, 2010.
- [205] Sascha Feldmann. Electronic Structure of the Tetraazaperopyrene/Au(111) Interface and Band Dispersion Probed by Two-Photon Photoemission Spectroscopy. Master's thesis, Universität Heidelberg - Fachbereich Chemie, 2017.
- [206] H. Petek and S. Ogawa. Femtosecond time-resolved two-photon photoemission studies of electron dynamics in metals. *Progress in Surface Science*, 56(4):239–310, 1997.
- [207] C. Timm and K. H. Bennemann. Response theory for time-resolved second-harmonic generation and two-photon photoemission. *Journal of Physics: Condensed Matter*, 16(4):661, 2004.
- [208] Sebastian Hagen. *Isomerization behavior of photochromic molecules in direct contact with noble metal surfaces*. PhD thesis, Freien Universität Berlin - Fachbereich Physik, 2009.
- [209] Anton Haase. Graphene Nanoribbons on the Au(111) Surface Investigated with Two-Photon Photoemission. Master's thesis, Universität Berlin - Fachbereich Physik, 2012.
- [210] G. M. McGuirk, H. Shin, M. Caragiu, S. Ash, P. K. Bandyopadhyay, R. H. Prince, and R. D. Diehl. Au(111) surface structures induced by adsorption: LEED I (E) analysis of (1×1) and (5×5) Au(111)-S phases. *Surface Science*, 610:42–47, 2013.
- [211] O. L. Griffith, J. E. Anthony, A. G. Jones, Y. Shu, and D. L. Lichtenberger. Substituent effects on the electronic characteristics of pentacene derivatives for organic electronic devices: Dioxolane-substituted pentacene derivatives with triisopropylsilylethynyl functional groups. *Journal of the American Chemical Society*, 134(34):14185–14194, 2012.
- [212] S. C. B. Mannsfeld, M. L. Tang, and Z. Bao. Thin film structure of triisopropylsilylethynyl-functionalized pentacene and tetraceno [2, 3-b]thiophene from grazing incidence X-Ray diffraction. *Advanced Materials*, 23(1):127–131, 2011.

- [213] M. J. Y. Tayebjee, K. N. Schwarz, R. W. MacQueen, M. Dvorak, A. W. C. Lam, K. P. Ghiggino, D. R. McCamey, T. W. Schmidt, and G. J. Conibeer. Morphological evolution and singlet fission in aqueous suspensions of TIPS-pentacene nanoparticles. *The Journal of Physical Chemistry C*, 120(1):157–165, 2015.
- [214] C. Ramanan, A. L. Smeigh, J. E. Anthony, T. J. Marks, and M. R. Wasielewski. Competition between singlet fission and charge separation in solution-processed blend films of 6,13-bis(triisopropylsilylethynyl) pentacene with sterically-encumbered perylene-3,4:9,10-bis(dicarboximide)s. *Journal of the American Chemical Society*, 134(1):386–397, 2012.
- [215] B. J. Walker, A. J. Musser, D. Beljonne, and R. H. Friend. Singlet exciton fission in solution. *Nature Chemistry*, 5(12):1019, 2013.
- [216] O. L. Griffith, A. G. Jones, J. E. Anthony, and D. L. Lichtenberger. Intermolecular effects on the hole states of triisopropylsilylethynyl-substituted oligoacenes. *The Journal of Physical Chemistry C*, 114(32):13838–13845, 2010.
- [217] O. L. Griffith, N. E. Gruhn, J. E. Anthony, B. Purushothaman, and D. L. Lichtenberger. Electron transfer parameters of triisopropylsilylethynyl-substituted oligoacenes. *The Journal of Physical Chemistry C*, 112(51):20518–20524, 2008.
- [218] J. B. Sherman, K. Moncino, T. Baruah, G. Wu, S. R. Parkin, B. Purushothaman, R. Zope, J. Anthony, and M. L. Chabinyc. Crystalline alloys of organic donors and acceptors based on TIPS-pentacene. *The Journal of Physical Chemistry C*, 119(36):20823–20832, 2015.
- [219] A. Gnoli, H. Ustunel, D. Toffoli, L. Yu, D. Catone, S. Turchini, S. Lizzit, N. Stingelin, and R. Larciprete. Bis(triisopropylsilylethynyl)-pentacene/Au(111) interface: Coupling, molecular orientation, and thermal stability. *The Journal of Physical Chemistry C*, 118(39):22522–22532, 2014.
- [220] J. Chen, J. Anthony, and D. C. Martin. Thermally induced solid-state phase transition of bis(triisopropylsilylethynyl)-pentacene crystals. *The Journal of Physical Chemistry B*, 110(33):16397–16403, 2006.
- [221] S. Sharifzadeh, C. Y. Wong, H. Wu, B. L. Cotts, L. Kronik, N. S. Ginsberg, and J. B. Neaton. Relating the physical structure and optoelec-

Bibliography

- tronic function of crystalline TIPS-pentacene. *Advanced Functional Materials*, 25(13):2038–2046, 2015.
- [222] S. Hagen, F. Leyssner, D. Nandi, M. Wolf, and P. Tegeder. Reversible switching of tetra-tert-butyl-azobenzene on a Au(111) surface induced by light and thermal activation. *Chemical Physics Letters*, 444(1-3):85–90, 2007.
- [223] E. Varene, L. Bogner, S. Meyer, Y. Pennec, and P. Tegeder. Coverage-dependent adsorption geometry of octithiophene on Au(111). *Physical Chemistry Chemical Physics*, 14(2):691–696, 2012.
- [224] E. Varene, I. Martin, and P. Tegeder. Optically induced inter- and intrafacial electron transfer probed by two-photon photoemission: Electronic states of sexithiophene on Au(111). *The Journal of Physical Chemistry Letters*, 2(3):252–256, 2011.
- [225] I. F. Torrente, K. J. Franke, and J. I. Pascual. Structure and electronic configuration of tetracyanoquinodimethane layers on a Au(111) surface. *International Journal of Mass Spectrometry*, 277(1-3):269–273, 2008.
- [226] Y. Wu, K. Liu, H. Liu, Y. Zhang, H. Zhang, J. Yao, and H. Fu. Impact of intermolecular distance on singlet fission in a series of TIPS-pentacene compounds. *The Journal of Physical Chemistry Letters*, 5(20):3451–3455, 2014.
- [227] H. Fischer and F. Meyer-Betz. Zur Kenntnis der Porphyrinbildung. I. Mitteilung. *Hoppe-Seyler's Zeitschrift für physiologische Chemie*, 82(1-2):96–108, 1912.
- [228] S. Rangan, S. Katalinic, R. Thorpe, R. A. Bartynski, J. Rochford, and E. Galoppini. Energy level alignment of a Zinc (II) tetraphenylporphyrin dye adsorbed onto TiO₂ (110) and ZnO (1120) surfaces. *The Journal of Physical Chemistry C*, 114(2):1139–1147, 2009.
- [229] G. Rojas, X. Chen, C. Bravo, J. Kim, J. Kim, J. Xiao, P. A. Dowben, Y. Gao, X. C. Zeng, W. Choe, et al. Self-assembly and properties of nonmetalated tetraphenyl-porphyrin on metal substrates. *The Journal of Physical Chemistry C*, 114(20):9408–9415, 2010.
- [230] P. L. Cook, W. Yang, X. Liu, J. M. García-Lastra, A. Rubio, and F. J. Himpsel. Unoccupied states in Cu and Zn octaethyl-porphyrin and phthalocyanine. *The Journal of Chemical Physics*, 134(20):204707, 2011.

- [231] S. Rangan, S. Coh, R. A. Bartynski, K. P. Chitre, E. Galoppini, C. Jaye, and D. Fischer. Energy alignment, molecular packing, and electronic pathways: Zinc (II) tetraphenylporphyrin derivatives adsorbed on TiO₂ (110) and ZnO (11–20) surfaces. *The Journal of Physical Chemistry C*, 116(45):23921–23930, 2012.
- [232] G. Bussetti, A. Calloni, R. Yivlialin, A. Picone, F. Bottegoni, and M. Finazzi. Filled and empty states of Zn-TPP films deposited on Fe(001)-p(1×1)O. *Beilstein Journal of Nanotechnology*, 7:1527, 2016.
- [233] C. Ruggieri, S. Rangan, R. A. Bartynski, and E. Galoppini. Zinc (II) tetraphenylporphyrin on Ag(100) and Ag(111): Multilayer desorption and dehydrogenation. *The Journal of Physical Chemistry C*, 120(14):7575–7585, 2016.
- [234] S. Rangan, C. Ruggieri, R. Bartynski, J. I. Martínez, F. Flores, and J. Ortega. Densely packed ZnTPPs monolayer on the rutile TiO₂ (110)-(1×1) surface: Adsorption behavior and energy level alignment. *The Journal of Physical Chemistry C*, 120(8):4430–4437, 2016.
- [235] L. Giovanelli, H.-L. Lee, C. Lacaze-Dufaure, M. Koudia, S. Clair, Y.-P. Lin, Y. Ksari, J.-M. Themlin, M. Abel, and A. A. Cafolla. Electronic structure of tetra(4-aminophenyl)porphyrin studied by photoemission, UV–Vis spectroscopy and density functional theory. *Journal of Electron Spectroscopy and Related Phenomena*, 218:40–45, 2017.
- [236] H. Ishii, S. Hasegawa, D. Yoshimura, K. Sugiyama, S. Narioka, M. Sei, Y. Ouchi, K. Seki, Y. Harima, and K. Yamashita. Electronic structures of porphyrins and their interfaces with metals studied by UV photoemission. *Molecular Crystals and Liquid Crystals Science and Technology. Section A. Molecular Crystals and Liquid Crystals*, 296(1):427–444, 1997.
- [237] S. Narioka, H. Ishii, D. Yoshimura, M. Sei, Y. Ouchi, K. Seki, S. Hasegawa, T. Miyazaki, Y. Harima, and K. Yamashita. The electronic structure and energy level alignment of porphyrin/metal interfaces studied by ultraviolet photoelectron spectroscopy. *Applied Physics Letters*, 67(13):1899–1901, 1995.
- [238] T. G. Gopakumar, H. Tang, J. Morillo, and R. Berndt. Transfer of Cl ligands between adsorbed iron tetraphenylporphyrin molecules. *Journal of the American Chemical Society*, 134(29):11844–11847, 2012.

Bibliography

- [239] A. Bendounan and S. Aït-Ouazzou. Role of the Shockley state in doping of organic molecule monolayer. *The Journal of Physical Chemistry C*, 120(21):11456–11464, 2016.
- [240] R. Einholz, T. Fang, R. Berger, P. Grüniger, Andreas Früh, T. Chasse, R. F. Fink, and H. F. Bettinger. Heptacene: Characterization in solution, in the solid state, and in films. *Journal of the American Chemical Society*, 139(12):4435–4442, 2017.
- [241] F. Ortmann, K. S. Radke, A. Günther, D. Kasemann, K. Leo, and G. Cuniberti. Materials meets concepts in molecule-based electronics. *Advanced Functional Materials*, 25(13):1933–1954, 2015.
- [242] C. Wang, H. Dong, W. Hu, Y. Liu, and D. Zhu. Semiconducting π -conjugated systems in field-effect transistors: a material odyssey of organic electronics. *Chemical Reviews*, 112(4):2208–2267, 2011.
- [243] G. Zhang, F. Rominger, U. Zschieschang, H. Klauk, and M. Mastalerz. Facile synthetic approach to a large variety of soluble diarenopenylenes. *Chemistry—A European Journal*, 22(42):14840–14845, 2016.
- [244] Z. Wang, P. Gu, G. Liu, H. Yao, Y. Wu, Y. Li, G. Rakesh, J. Zhu, H. Fu, and Q. Zhang. A large pyrene-fused N-heteroacene: fifteen aromatic six-membered rings annulated in one row. *Chemical Communications*, 53(55):7772–7775, 2017.
- [245] B. Kohl, F. Rominger, and M. Mastalerz. Ein Pyren-fusioniertes N-Heteroacene mit elf linear anellierten aromatischen Ringen. *Angewandte Chemie*, 127(20):6149–6154, 2015.
- [246] Q. Miao. Ten years of N-heteropentacenes as semiconductors for organic thin-film transistors. *Advanced Materials*, 26(31):5541–5549, 2014.
- [247] U. H. F. Bunz, J. U. Engelhart, B. D. Lindner, and M. Schaffroth. Große N-Heteroacene: ein alter Hut mit neuen Federn. *Angewandte Chemie*, 125(14):3898–3910, 2013.
- [248] U. H. F. Bunz. N-heteroacenes. *Chemistry—A European Journal*, 15(28):6780–6789, 2009.
- [249] U. H. F. Bunz. The larger linear N-heteroacenes. *Accounts of Chemical Research*, 48(6):1676–1686, 2015.
- [250] Z. Liang, Q. Tang, R. Mao, D. Liu, J. Xu, and Q. Miao. The position of nitrogen in N-heteropentacenes matters. *Advanced Materials*, 23(46):5514–5518, 2011.

- [251] Z. Liang, Q. Tang, J. Xu, and Q. Miao. Soluble and stable N-heteropentacenes with high field-effect mobility. *Advanced Materials*, 23(13):1535–1539, 2011.
- [252] M. Schulze, C. Bronner, and P. Tegeder. Adsorption energetics of azobenzenes on noble metal surfaces. *Journal of Physics: Condensed Matter*, 26(35):355004, 2014.
- [253] E. R. McNellis, C. Bronner, J. Meyer, M. Weinelt, P. Tegeder, and K. Reuter. Azobenzene versus 3,3',5,5'-tetra-tert-butyl-azobenzene (TBA) at Au(111): Characterizing the role of spacer groups. *Physical Chemistry Chemical Physics*, 12(24):6404–6412, 2010.
- [254] P. Tegeder, S. Hagen, F. Leyssner, M. V. Peters, S. Hecht, T. Klamroth, P. Saalfrank, and M. Wolf. Electronic structure of the molecular switch tetra-tert-butyl-azobenzene adsorbed on Ag(111). *Applied Physics A*, 88(3):465–472, 2007.
- [255] C. Bronner, B. Priewisch, K. Rück-Braun, and P. Tegeder. Photoisomerization of an azobenzene on the Bi(111) surface. *The Journal of Physical Chemistry C*, 117(51):27031–27038, 2013.
- [256] L. Óvári, Y. Luo, F. Leyssner, R. Haag, M. Wolf, and P. Tegeder. Adsorption and switching properties of a N-benzylideneaniline based molecular switch on a Au(111) surface. *The Journal of Chemical Physics*, 133(4):044707, 2010.
- [257] C. Bronner and P. Tegeder. Photo-induced and thermal reactions in thin films of an azobenzene derivative on Bi(111). *New Journal of Physics*, 16(5):053004, 2014.
- [258] N. Gonzalez-Lakunza, I. Fernandez-Torrente, K. J. Franke, N. Lorente, A. Arnau, and J. I. Pascual. Formation of dispersive hybrid bands at an organic-metal interface. *Physical Review Letters*, 100(15):156805, 2008.
- [259] C. H. Schwalb, S. Sachs, M. Marks, A. Schöll, F. Reinert, E. Umbach, and U. Höfer. Electron lifetime in a Shockley-type metal-organic interface state. *Physical Review Letters*, 101(14):146801, 2008.
- [260] R. Temirov, S. Soubatch, A. Luican, and F. S. Tautz. Free-electron-like dispersion in an organic monolayer film on a metal substrate. *Nature*, 444(7117):350, 2006.

Bibliography

- [261] M. S. Dyer and M. Persson. The nature of the observed free-electron-like state in a PTCDA monolayer on Ag(111). *New Journal of Physics*, 12(6):063014, 2010.
- [262] K. M. Andrews and T. P. Pearl. Modification of Ag(111) surface electronic structure via weak molecular adsorption of adenine measured with low temperature scanning tunneling microscopy and spectroscopy. *The Journal of Chemical Physics*, 132(21):214701, 2010.
- [263] B. W. Heinrich, L. Limot, M. V. Rastei, C. Iacovita, J. P. Bucher, D. M. Djimbi, C. Massobrio, and M. Boero. Dispersion and localization of electronic states at a ferrocene/Cu(111) interface. *Physical Review Letters*, 107(21):216801, 2011.
- [264] M. Marks, N. L. Zaitsev, B. Schmidt, C. H. Schwalb, A. Schöll, I. A. Nechaev, P. M. Echenique, E. V. Chulkov, and U. Höfer. Energy shift and wave function overlap of metal-organic interface states. *Physical Review B*, 84(8):081301, 2011.
- [265] M. C. E. Galbraith, M. Marks, R. Tonner, and U. Höfer. Formation of an organic/metal interface state from a Shockley resonance. *The Journal of Physical Chemistry Letters*, 5(1):50–55, 2013.
- [266] B. W. Caplins, D. E. Suich, A. J. Shearer, and C. B. Harris. Metal/phthalocyanine hybrid interface states on Ag(111). *The Journal of Physical Chemistry Letters*, 5(10):1679–1684, 2014.
- [267] F. Würthner and M. Stolte. Naphthalene and perylene diimides for organic transistors. *Chemical Communications*, 47(18):5109–5115, 2011.
- [268] U. H. F. Bunz, J. U. Engelhart, B. D. Lindner, and M. Schaffroth. Large N-heteroacenes: New tricks for very old dogs? *Angewandte Chemie International Edition*, 52(14):3810–3821, 2013.
- [269] M. Matena, M. Stöhr, T. Riehm, J. Björk, S. Martens, M. S. Dyer, M. Persson, J. Lobo-Checa, K. Müller, M. Enache, et al. Aggregation and contingent metal/surface reactivity of 1,3,8,10-tetraazaperopyrene (TAPP) on Cu(111). *Chemistry—A European Journal*, 16(7):2079–2091, 2010.
- [270] J. Björk, M. Matena, M. S. Dyer, M. Enache, J. Lobo-Checa, L. H. Gade, T. A. Jung, M. Stöhr, and M. Persson. STM fingerprint of molecule–adatom interactions in a self-assembled metal–organic surface coordination network on Cu(111). *Physical Chemistry Chemical Physics*, 12(31):8815–8821, 2010.

- [271] M. Matena, T. Riehm, M. Stöhr, T. A. Jung, and L. H. Gade. Transforming surface coordination polymers into covalent surface polymers: Linked polycondensed aromatics through oligomerization of N-heterocyclic carbene intermediates. *Angewandte Chemie International Edition*, 47(13):2414–2417, 2008.
- [272] S. Blankenburg, E. Rauls, and W. G. Schmidt. Catalytic action of a Cu(111) surface on tetraazaperopyrene polymerization. *The Journal of Physical Chemistry Letters*, 1(22):3266–3270, 2010.
- [273] F. Maass, A. Stein, B. Kohl, L. Hahn, L. H. Gade, M. Mastalerz, and P. Tegeder. Substrate-directed growth of N-heteropolycyclic molecules on a metal surface. *The Journal of Physical Chemistry C*, 120(5):2866–2873, 2016.
- [274] Alexander Broska. Elektronische Eigenschaften von Tetraazaperopyrenen auf Gold (111). Master’s thesis, Universität Heidelberg - Fachbereich Physik, 2014.
- [275] R. Courths, H. Zimmer, A. Goldmann, and H. Saalfeld. Electronic structure of gold: An angle-resolved photoemission study along the λ line. *Physical Review B*, 34(6):3577, 1986.

List of Publications, Conference Contributions and Supervised Theses

List of Publications

Publications Related to this Thesis

Triisopropylsilylethynyl-Pentacene on Au(111): Adsorption Properties, Electronic Structure, and Singlet Fission Dynamics

A. Stein, F. Maaß, and P. Tegeder

J. Phys. Chem. C 121, 18075 (2017)

Electronic Structure of an Iron-Porphyrin Derivative on Au(111)

A. Stein, D. Rolf, C. Lotze, C. Czekelius, K. J. Franke, and P. Tegeder

J. Phys. Condens. Matter 31(4), 044002 (2018)

Band Formation at Interfaces between N-Heteropolycycles and Gold Electrodes: Beneficial for Efficient Charge Injection

A. Stein, D. Rolf, C. Lotze, B. Günther, L. H. Gade, K. J. Franke, and P. Tegeder

in preparation

An “Arrowshaped” N-Heteropentacene on Au(111): Adsorption Properties and Electronic Structure

A. Stein, M. Ajardi, M. Müller, C. Placke, U. H. F. Bunz, and P. Tegeder

in preparation

Electronic Structure at Tetraazaperopyrene/Au(111) interfaces

A. Stein, D. Rolf, S. Feldmann, C. Lotze, D. Gerbert, A. Broska, B. Günther, L. Hahn, L. H. Gade, K. J. Franke, and P. Tegeder

in preparation

Publications Not Related to this Thesis

Dependence of the adsorption height of graphene-like adsorbates on their dimensionality

S. Weiß, D. Gerbert, A. Stein, A. K. Schenk, X. Yang, C. Brülke, R. Kremring, S. Feldmann, F. C. Bocquet, M. Gille, S. Hecht, M. Sokolowski, P. Tegeder, S. Soubatch, and F. S. Tautz

Phys. Rev. B 98, 075410 (2018)

2,6-Bis(5,6-diisopropyl-1,2,4-triazin-3-yl)pyridine: a highly selective N-donor ligand studied by TRLFS, liquid-liquid extraction and molecular dynamics

B. B. Beele, A. Skerencak-Frech, A. Stein, M. Trumm, A. Wilden, S. Lange, G. Modolo, U. Müllich, B. Schimmelpfennig, A. Geist and P. J. Panak

New J. Chem. 40, 10389 (2016)

Substrate-Directed Growth of N-Heteropolycyclic Molecules on a Metal Surface

F. Maaß, A. Stein, B. Kohl, L. Hahn, L. H. Gade, M. Mastalerz, and P. Tegeder
J. Phys. Chem. C 120, 2866 (2016)

List of Conference Contributions

Electronic Structure of TIPS-Pentacene on Au(111)

A. Stein and P. Tegeder

Presentation

DPG Spring Meeting, Regensburg, Germany, 2016

Excited state dynamics in TIPS-Pentacene on Au(111)

A. Stein and P. Tegeder

Presentation

DPG Spring Meeting, Dresden, Germany, 2017

TIPS-Pentacene on Au(111): Electronic structure and singlet fission dynamics

A. Stein, F. Maaß, and P. Tegeder

Poster

European Conference on Molecular Electronics, Dresden, Germany, 2017

Band formation at the Tetraazaperopyrene/Au(111) Interface

A. Stein, S. Feldmann, B. Günther, L. H. Gade, and P. Tegeder

Presentation

DPG Spring Meeting, Berlin, Germany, 2018

TIPS-Pentacene on Au(111): Electronic structure and singlet fission dynamics

A. Stein, F. Maaß, and P. Tegeder

Poster

The 2nd International Symposium on Singlet Fission and Photon Fusion, Gothenburg, 2018

Band Formation at the Tetraazaperopyrene/Au(111) Interface

A. Stein, S. Feldmann, D. Gerbert, A. Broska, B. Günther, L. Hahn, L. H. Gade, and P. Tegeder

Poster

Materials for organic Electronics, Heidelberg, 2018

List of Supervised Theses

Untersuchung von Stickstoff-substituierten TIPS-Pentacen Derivaten mittels Zwei-Photonen Photoemissionsspektroskopie

Patrik Weßling, Ruprecht-Karls-Universität Heidelberg, January 2017
Scientific Internship

Electronic Structure of the Tetraazaperopyrene/Au(111) Interface and Band Dispersion Probed by Two-Photon Photoemission Spectroscopy

Sascha Feldmann, Ruprecht-Karls-Universität Heidelberg, August 2017
Master Thesis

Untersuchung von Eisen-Tetrapyridylporphyrin auf Au(111) mittels Zwei-Photonen-Photoemissionsspektroskopie

Sonja Wieland, Ruprecht-Karls-Universität Heidelberg, April 2018
Scientific Internship

Untersuchung der elektronischen Struktur von Eisen-Tetrapyridylporphyrin auf Au(111) mittels Zwei-Photonen-Photoemissionsspektroskopie

Elena Michel, Ruprecht-Karls-Universität Heidelberg, Juli 2018
Scientific Internship

Untersuchung des TIPS-Pentacen Derivats TIPS-BAP auf Au(111) mittels Zwei-Photonen-Photoemissionsspektroskopie

Carsten Placke, Ruprecht-Karls-Universität Heidelberg, February 2019
Scientific Internship

Acknowledgements

An dieser Stelle möchte ich mich bei all jenen bedanken, die mich im Laufe meiner Promotion begleitet und unterstützt haben.

Im Besonderen danke ich:

Frau Prof. Dr. Tegeder für die Möglichkeit in ihrer Arbeitsgruppe zu promovieren und die hervorragende Unterstützung und Betreuung. Hervorzuheben seien an dieser Stelle die Möglichkeiten zur Teilnahme an diversen Tagungen und den Forschungsaufenthalten an der Columbia State University in New York City sowie an der Diamond Light Source in Oxfordshire.

Herrn Prof. Dr. Volpp für die freundliche Übernahme des Zweitgutachtens.

Meinen diversen Kooperationspartnern mit welchen ich im Rahmen dieser Arbeit zusammenarbeiten durfte und ohne jene die Arbeit in der vorliegenden Form nicht möglich gewesen wäre. Im Speziellen seien hier erwähnt: Dr. Daniela Rolf, Christian Lotze, und Prof. Dr. Katharina J. Franke für die Messung, Interpretation und Bereitstellung von STS und STM Daten, Benjamin Günther, Dr. Lena Hahn, Matthias Müller, Prof. Dr. Lutz H. Gade, Prof. Dr. Uwe Bunz, und Prof. Dr. Constantin Czekelius für die Synthese und Bereitstellung der untersuchten Moleküle, sowie die Mitarbeiter des MS-Labors unter der Leitung von Dr. Jürgen Gross für die Messung der verwendeten Massenspektren.

Meinen Kollegen Marc Hänsel, Friedrich Maaß, David Gerbert, Vipilan Sivanesan, Mohsen Ajdari, Tanja Schmitt, und Sascha Feldmann für die fruchtbare Zusammenarbeit, hohe Hilfsbereitschaft und angenehme Arbeitsatmosphäre. David Gerbert sei an dieser Stelle noch einmal zusätzlich für die Einweisung und langwährende Unterstützung an den experimentellen Aufbauten, sowie für die Bereitstellung der Messdaten an der TAPP-(C₃F₇)₂/Au(111) Grenzfläche gedankt.

Meinen Forschungspraktikanten Patrik Weßling, Sonja Wieland, Elena Michel und Carsten Placke für ihren Arbeitseinsatz und die anregenden Diskussionen.

Für die Unterstützung über diese Arbeit hinaus möchte ich mich ganz herzlich bei meinen Eltern und meiner gesamten Familie bedanken. Mein ganz besonderer Dank gilt abschließend Leonhard, Eike, Inga und Friederike,

List of Publications

welche mein Leben tagtäglich bereichern und für den nötigen Ausgleich sorgen.

Vielen Dank!



**Eidesstattliche Versicherung gemäß § 8 der Promotionsordnung für die
Naturwissenschaftlich-Mathematische Gesamtfakultät der Universität Heidelberg /
Sworn Affidavit according to § 8 of the doctoral degree regulations of the Combined
Faculty of Natural Sciences and Mathematics**

1. Bei der eingereichten Dissertation zu dem Thema / **The thesis I have submitted entitled**

.....
.....

handelt es sich um meine eigenständig erbrachte Leistung / **is my own work.**

2. Ich habe nur die angegebenen Quellen und Hilfsmittel benutzt und mich keiner unzulässigen Hilfe Dritter bedient. Insbesondere habe ich wörtlich oder sinngemäß aus anderen Werken übernommene Inhalte als solche kenntlich gemacht. / **I have only used the sources indicated and have not made unauthorised use of services of a third party. Where the work of others has been quoted or reproduced, the source is always given.**

3. Die Arbeit oder Teile davon habe ich wie folgt/bislang nicht¹⁾ an einer Hochschule des In- oder Auslands als Bestandteil einer Prüfungs- oder Qualifikationsleistung vorgelegt. / **I have not yet/have already¹⁾ presented this thesis or parts thereof to a university as part of an examination or degree.**

Titel der Arbeit / **Title of the thesis:**

Hochschule und Jahr / **University and year:**

Art der Prüfungs- oder Qualifikationsleistung / **Type of examination or degree:**

4. Die Richtigkeit der vorstehenden Erklärungen bestätige ich. / **I confirm that the declarations made above are correct.**

5. Die Bedeutung der eidesstattlichen Versicherung und die strafrechtlichen Folgen einer unrichtigen oder unvollständigen eidesstattlichen Versicherung sind mir bekannt. / **I am aware of the importance of a sworn affidavit and the criminal prosecution in case of a false or incomplete affidavit.**

Ich versichere an Eides statt, dass ich nach bestem Wissen die reine Wahrheit erklärt und nichts verschwiegen habe. / **I affirm that the above is the absolute truth to the best of my knowledge and that I have not concealed anything.**

.....
Ort und Datum / **Place and date**

.....
Unterschrift / **Signature**

¹⁾ Nicht Zutreffendes streichen. Bei Bejahung sind anzugeben: der Titel der andernorts vorgelegten Arbeit, die Hochschule, das Jahr der Vorlage und die Art der Prüfungs- oder Qualifikationsleistung. / **Please cross out what is not applicable. If applicable, please provide: the title of the thesis that was presented elsewhere, the name of the university, the year of presentation and the type of examination or degree.**